AS-TEXONO/98-07
Revised : December 7, 1998

A Pilot Experiment With Reactor Neutrino in Taiwan : A Technical Status Report[1]

The TEXONO Collaboration

Abstract

A Collaboration among scientists from Taiwan, mainland China and the U.S.A has been built up to initiate and pursue an experimental program in neutrino physics. A pilot experiment to be performed at the Nuclear Power Plant II in Taiwan is under intense preparation. The experiment will make use of a 500 kg CsI(Tl) crystal calorimeter to study various neutrino interactions. This report documents the experimental details of this effort.

[1]Available from http://hep1.phys.sinica.edu.tw/~exono/TEXT/TEXONO/texono9807.ps

The TEXONO[2] : Kuo-Sheng[3] Collaboration

C.P. Chen, M.L. Chu, G.C. Jon, G.C. Kiang, W.L. Lai, W.P. Lai, S.C. Lee,
P.K. Teng, C.W. Wang, S.C. Wang, T.F. Wang, H.T.K. Wong
Academia Sinica, Taipei, Taiwan

D.I. Lee, D.S. See, Y.T. Yang, T.R. Yeh
Institute of Nuclear Energy Research, Lungtan, Taiwan

Y.C. Tan
National Chiayi Teachers College, Chiayi, Taiwan

C.L. Kao, H.B. Li,
National Taiwan University, Taipei, Taiwan

J.H. Chao, K.P. Chen, C.Y. Liang, H.M. Liu
National Tsing Hua University, Hsinchu, Taiwan

R.F. Su
Nuclear Power Plant II, Kuosheng, Taiwan

L. He, H.Q. Tang, Z.Y. Zhou
Institute of Atomic Energy, Beijing

Y.F. Lai, J. Li, Y. Liu, J.G. Lu, Z.P. Mao, L. Meng, J.F. Qiu,
H.Y. Sheng, H.Y. Wang, P.L. Wang, X.M. Xia, D.X. Zhao,
J.W. Zhao, P.P. Zhao, S.Q. Zhao, B.A. Zhuang
Institute of High Energy Physics, Beijing

T.Y. Chen
Nanjing University, Nanjing

M. He, X.Y. Zhang
Shandong University, Jinan

X.Q. Yu
University of Science and Technology, Hefei

Z.Y. Zhang, Z.S. Zhao
Institute for Radiation Protection, Taiyuan

G.C.C. Chang, C.Y. Chang

[2]**T**aiwan **EX**periment **O**n Reactor **N**eutrin**O**.

[3]Kuo-Sheng, "National-Saint" in Chinese, is the site of Nuclear Power Station II where the Experiment will be performed.

University of Maryland, Maryland, U.S.A.

Regional Co-ordinators :

Taiwan - Henry T. Wong, Academia Sinica (htwong@sinica.edu.tw);

Mainland China - Jin Li, Institute of High Energy Physics, Beijing (lijin@bepc5.ihep.ac.cn);

U.S.A. - George C.C. Chang, University of Maryland (chang@enp.umd.edu).

Contents

List of Tables

List of Figures

1 Scope of this Report

In this report, we describe the experimental details of the "Pilot Experiment". The information presented is complementary to various other reports on the different aspects of our activities :

1. "The Starting Up of a Neutrino Project in Taiwan"(AS-TEXONO/97-03) [1], which documents our first year of strategies and activities, which focussed on a boron-loaded liquid scintillator for reactor neutrinos.
2. "A Feasibility Study of Boron-Loaded Liquid Scintillator for the Detector of Electron Anti-neutrinos"(AS-TEXONO/98-05) [2], which describes our R&D efforts in developing such a scintillator.
3. "A Pilot Experiment with Reactor Neutrinos in Taiwan"(AS-TEXONO/98-04) [3], which describes the motivations of our new approach of using CsI(Tl) crystal scintillators for the pilot experiment, the physics program and the conceptual design of the experiment.
4. "Outlook and Evolution of the TEXONO Collaboration" [4], which presents our view on how our activities can fit into the world arena of experimental neutrino physics, and expresses our interest of pursuing the studies of solar neutrinos as a long-term goal.

These articles are available upon request, and can be downloaded in postscript format from Web-site http://hep1.phys.sinica.edu.tw/~exono/TEXT/TEXONO/ .

2 A Crystal Calorimeter for Reactor Neutrinos

2.1 Motivations

Almost all previous reactor neutrino experiments [5] and future projects [6] are based on liquid scintillator techniques to study the ($\bar{\nu}_e$ p) interactions, but with different neutron-capture isotopes. A summary is given in Table 1. An experiment capable of high-quality gamma detection has never been attempted. However, gamma-ray spectroscopy has been a standard technique in nuclear sciences (that is, in the investigations of physics at the MeV range). Gamma-lines of characteristic energies give unambiguous information on the presence and transitions of whichever isotopes, allowing a unique interpretation of the physical processes.

The experimental difficulties of realizing a high-quality gamma detector for MeV neutrino physics have been the large target mass required. However, in the past few years, big electro-magnetic calorimeter system (with mass up to 40 tons of crystals, in the case for the forthcoming B-factories experiments [7]) have been built for high energy physics experiments, using CsI(Tl) crystals with photo-diodes readout.

The CsI-crystal production technology is by now well matured and the cost has been reduced enormously due to these large demands. It become realistic and affordable to build a CsI detector in the range of 1-ton in target mass for a reactor neutrino experiment.

Since a precision gamma-detection with a crystal calorimeter is a new approach to neutrino experiment, it does offer a wide spectrum of physics (and thesis!) opportunities with a rather modest investment of cost, manpower and time, well suited for a starting group. It is also technically much simpler to build and to operate than, for instance, gas chambers and liquid scintillators. The background processes for such novel applications are not thoroughly understood. It is a new research domain the experiment will explore and will require state-of-the-art techniques in its control, identification and suppression.

Furthermore, as indicated in Ref. [4], the crystal calorimetry techniques may have much potentials in the studies of dark matter and solar neutrinos. Indeed, NaI(Tl) crystals are now being deployed for dark matter searches, giving some of the best results so far [8]. Therefore, our efforts in realizing and operating the pilot experiment are coherent with, and indeed necessary for, our long-term goals. The pilot experiment will be a platform for building up a Collaboration, and a "launch-pad" for more ambitious projects beyond.

2.2 Physics Menu

In this section, we discuss the various physics items which can be potentially addressed by a 500 kg-CsI detector. A summary of the world-status on these measurements as well as the projected sensitivities the CsI detector can achieve will be discussed at Section 5.

Previous experiments with reactor neutrinos primarily focused on the ($\bar{\nu}_e$ p) interactions to look for neutrino oscillations. However, the use of low energy (MeV) neutrino as a probe to study particle and nuclear physics has not been well explored - although high energy (GeV) neutrino beams from accelerators have been very productive in investigating electroweak, QCD and structure function physics [9] and have blossomed into a matured field. There are rooms for interesting physics with reactor neutrino experiments along this direction.

2.2.1 Neutrino-Electron Scattering

The cross section for the process

$$\bar{\nu_e} + e^- \rightarrow \bar{\nu_e} + e^-$$

gives information on the electro-weak parameters (g_V, g_A, and $\sin^2\theta_W$), and are sensitive to small neutrino magnetic moments (μ_ν) and the mean square charge radius ($< r^2 >$) [10, 11]. Scatterings of the (ν_e e) and ($\bar{\nu_e}$ e) are two of the most realistic systems where the interference effects between Z and W exchanges can be studied [12], as shown by the Feynman diagrams in Figure 1. Many of the existing and proposed solar neutrino detectors (Kamiokande, Super-Kamiokande, Borexino, HELLAZ...) [13] make use of the ν_e-e interactions as their detection mechanisms. The W-Z interference is the physics-basis of Resonace Neutrino Oscillation in Matter (the "MSW" Effect) [14].

In an experiment, what can be measured is the recoil energy of the electron (T). The differential cross section can be expressed as :

$$\begin{aligned}\frac{d\sigma}{dT}(\nu\ e) &= \frac{G_F^2 m_e}{2\pi}[(g_V + x + g_A)^2 + (g_V + x - g_A)^2[1 - \frac{T}{E_\nu}]^2 + (g_A^2 - (g_V + x)^2)\frac{m_e T}{E_\nu^2}] \\ &+ \frac{\pi\alpha_{em}^2\mu_\nu^2}{m_e^2}[\frac{1 - T/E_\nu}{T}]\end{aligned}$$

where $g_V = 2\sin^2\theta_W - \frac{1}{2}$ and $g_A = -\frac{1}{2}$ for ν_μ e and ν_τ e scatterings where only neutral currents are involved, and

$$x = \frac{2M_W^2}{3} < r^2 > \sin^2\theta_W \quad \text{for} \quad \nu,$$

while replacing

$$\begin{array}{c} g_A \rightarrow -g_A \\ x \rightarrow -x \end{array} \quad \text{for} \quad \bar{\nu}\ .$$

For ν_e e scattering, both neutral and charged currents and their interference terms contribute, so that the cross sections can be evaluated by replacing $g_V \rightarrow g_V + 1$ and $g_A \rightarrow g_A + 1$.

The g_A^e Vs. g_V^e parameter space where ($\bar{\nu_e}$ e) scatterings are sensitive to is depicted in Figure 2. The complementarity with (ν_μ e, $\bar{\nu_\mu}$ e) can be readily seen. The expected recoil energy spectrum is displayed in Figure 3, showing standard model expectations and the case with an anomalous neutrino magnetic moment at the present limit. The μ_ν term have a $\frac{1}{\mathrm{T}}$ dependence. Accordingly, experimental searches for the neutrino magnetic moment should focus on the reduction of the threshold (usually background-limited) for the recoil electron energy.

Therefore, investigations of ($\bar{\nu_e}$ e) cross-sections with reactor neutrinos allow one to study electro-weak physics (measurement of $\sin^2\theta_{\mathrm{W}}$) at the MeV range, to test electron-muon universality (that is, whether ($\bar{\nu_e}$ e) can be described by the same $g_{V/A}$ as (ν_μ e) and ($\bar{\nu_\mu}$ e)), and to look for an anomalous neutrino magnetic moment if one can reduce background at low (less than 1 MeV) energy.

A 500 kg CsI crystal calorimeter will have more target electrons than previous experiments [15, 16, 17], and current projects [18] and thus can potentially improve the sensitivities of these studies. The signature for ($\bar{\nu_e}$ e) will be a single hit out of the several hundred channels in the active target configuration.

2.2.2 Neutrino Charged and Neutral Currents on Deuteron

The interactions

$$\mathrm{CC} \ : \ \bar{\nu_e} \ + \ \mathrm{d} \ \rightarrow \ \mathrm{e}^+ \ + \ \mathrm{n} \ + \ \mathrm{n} \quad (\text{Threshold} = 4.02 \text{ MeV})$$

and

$$\mathrm{NC} \ : \ \bar{\nu_e} \ + \ \mathrm{d} \ \rightarrow \ \bar{\nu_e} \ + \ \mathrm{p} \ + \ \mathrm{n} \quad (\text{Threshold} = 2.23 \text{ MeV})$$

have been observed [19, 20], and there are already theoretical work studying them [21, 22, 23, 25]. Improved measurements will be of interest, especially since the NC reaction is the detection channel adopted by the forthcoming SNO experiment [24] for solar neutrino detection. Measurement of the CC/NC ratio provides a complementary method to search for neutrino oscillations, which is independent of the detailed knowledge of the neutrino source. The unique and most attractive feature of the SNO experiment is its potential capabilities to perform this CC/NC ratio measurements for solar neutrino. It would be desirable and worthwhile to have a laboratory experiment demonstrating the validity of the technique, and to understand the systematics involved.

In a realistic experiment, the CsI crystal slabs will be put into a tank with 500 kg of heavy water (D_2O) with good neutron capture isotopes (like gadolinium or cadmium) either as dissolved salts or as inserted sheets. The CC signatures will be rather spectacular:

back-to-back 511 keV γs followed by two separate bursts of high energy γs produced in neutron capture by Gd or Cd. The NC detection will rely on a single γ-burst.

This is a complementary - and improved - technique to the previous experiments which used ^{3}He proportional counters which were sensitive only to neutrons. Therefore, the CsI detector, with its γ-detection capabilities, can differentiate the signals from the other neutron-producing background channels :

$$\begin{array}{rcl} \text{“Reines”} : \bar{\nu}_e + p & \rightarrow & e^+ + n \text{ (Threshold = 1.80 MeV) and} \\ \gamma \text{ Dissociation} : \gamma + d & \rightarrow & p + n \text{ (Threshold = 2.23 MeV) ,} \end{array}$$

and can prevent the CC events with one undetected neutron from contaminating the NC sample.

2.2.3 Neutral Current Excitation on ^{10}B and ^{11}B

If a compact boron-rich object like B_4C (natural boron consists of 20% ^{10}B and 80% ^{11}B) is used as the passive target, characteristic γ-lines (3.59, 5.16 MeV for ^{10}B, and 2.11, 4.45, 5.02 MeV for ^{11}B) will be emitted by the excited daughter nuclei following the NC interactions :

$$\bar{\nu}_e + {}^{10}\text{B} \rightarrow \bar{\nu}_e + {}^{10}\text{B}^*$$

and

$$\bar{\nu}_e + {}^{11}\text{B} \rightarrow \bar{\nu}_e + {}^{11}\text{B}^* .$$

There are theoretical works [22, 25, 26] suggesting that these cross sections [27, 28] are sensitive to the axial isoscalar component of NC interactions and the strange quark content of the nucleon. Therefore, νN NC scattering may provide a complementary approach to the investigations of nucleon structure physics comparing to the eN scattering systems. The ν_e NC interaction on ^{11}B has been considered as the detection mechanism in the BOREX solar neutrino proprosal [27].

A realistic experiment will consist of about 500 kg of B_4C, either in plate or powder form, inserted into a chamber with CsI crystals at optimized positions. The experimental signature will be gamma-lines of the characteristic energies which show up during reactor ON period.

If a CsI calorimeter proves itself to be optimal for studying NC excitations on nuclei [22, 25], where the experimental signatures are the characteristic γ-lines, one can insert other passive materials to measure their cross sections, and turns the experiment into a longer-term program.

2.2.4 Neutrino Charged and Neutral Currents on Nuclei

Neutrino interactions on nuclei have not been studied experimentally beyond a few light ones (^{1}H, ^{2}H, ^{12}C). If a CsI calorimeter proves itself to be optimal for low background MeV neutrino experiments where the experimental signatures are the characteristic γ-lines, one can insert other passive materials to measure the $\bar{\nu}_e$N CC or NC cross sections, and turns the detector into a longer-term experimental program.

Besides nuclear and nucleon structure physics issues, investigations of these interactions may provide important input to the considerations of future neutrino detectors, including the merits of an even larger scale CsI-calorimeter. The isotope ^{127}I has been proposed as a target material to study solar neutrinos [29]. The interaction rates of low-energy neutrinos on various nuclei have been considered [30] to study terrestial neutrinos coming from the radioactivity at the Earth's core.

There are two modes for the charged-current (CC) interactions: (I) Inverse beta decay

$$\bar{\nu_{\rm e}} ~+~ ({\rm A,Z}) ~\rightarrow~ {\rm e}^+ ~+~ ({\rm A,Z-1})^*$$

have signatures of 2 back-to-back 511 keV γs from the positron annihilation, plus the characteristic γ-lines from the daughter nuclei; (II) Resonant orbital electron capture

$$\bar{\nu_{\rm e}} ~+~ {\rm e}^- ~+~ ({\rm A,Z}) ~\rightarrow~~ ({\rm A,Z-1})^*$$

takes place only at a narrow range of neutrino energy equal to the Q-value of the transition. The signatures are the characteristic gamma lines for the excited daughter nuclei. The neutral current (NC) interactions

$$\bar{\nu_{\rm e}} ~+~ ({\rm A,Z}) ~\rightarrow~ \bar{\nu_{\rm e}} ~+~ ({\rm A,Z})^*$$

will have the characteristic γ-lines as signatures. The physics analysis of $\bar{\nu_e}$ on ^{133}Cs and ^{127}I will be performed. It is essentially a free by-product from the active target data taking where the main focus will be on $\bar{\nu_{\rm e}}$ e scatterings.

The evaluations of the NC cross sections of various nuclei have been performed [22, 25, 26], while estimations for the charge-current modes exist only for two extreme cases ^{3}He and ^{209}Bi [30]. Conventional expectations, however, would suggest that the CC is suppressed for stable high Z nuclei since they are usually neutron-rich, so that the CC interactions to produce (A,Z-1) daughter nuclei will involve conversion of proton to neutron and hence will be "Pauli-blocked".

Theoretical efforts in evaluating these cross-sections are not very matured and there are much room for further work. Research efforts can be organized to complement the experimental program to "cover the field".

3 Experimental Details

In this section, we describe the experimental details of the CsI calorimeter in the "Active Target" mode for $\bar{\nu_e}$-e scattering shown in Figure 4. This will be our first set-up and is where the focus is at for the moment. The "Passive Target" experiments for $\bar{\nu_e}$-N scattering, also shown in Figure 4, will share many common features on detector modules, electronics, data acquisition, shielding modules, simulation and analysis software tools. The primary difference will be the mechanical design of the inner detector region and the trigger schemes.

3.1 Locations

A list of power reactors in Taiwan is given in Table 2. The pilot experiment will be performed at the reactor building of Nuclear Power Plant II (NP2) near Kuo-Sheng at the northern coast of Taiwan. A schematic map of the location of NP2 is shown in Figure 5. The Taiwan Power Company (TPC) has officially approved our use of the sites.

The Plant consists of two Boiling Water Reactor cores each with 2.9 GW rated thermal power output. Two laboratory space are allocated for the experiment, and their locations are shown in the floor plans, both top and views, in Figure 6 and Figure 7, respectively. The sites are about 28 m from one reactor core and 102 m from the other. Each core has a reactor cycle of about 16 months, between which a shut-down period of typically 50 days. The sites have easy access for heavy equipment. Laboratory huts provided with electricity, telephone lines and air conditioning will be built.

Both sites are at "Level 1" or the lowest floor of the seven-storey reactor buildings. The bottom-most level is chosen because the floor can provide the best support to the heavy shieldings, while the over-burden materials which suppress cosmic rays flux are also maximized. The concrete for the buildings as well as the water for the reactor core cooling systems, amounts to an average of about 20-30 m of water equivalence (that is, about 30 nuclear interaction length) over-burden. The will suppress the cosmic muon flux by a factor of two and the primary hadron component to a negligible amount. The measured cosmic fluxes are 126, 74 and 34 $m^{-2}s^{-1}$ at AS 4F, AS basement and on-site, respectively.

Ambient radioactivity at the site have been surveyed with Thermoluminescent Dosimeters (TLDs) and NaI calorimeters. The background spectra are shown in Figure 8. The on-site γ background is about factor of 20 above the typical laboratory background level at energy below 1.4 MeV, attributed to excess of ^{60}Co in the steel inside the reinforced concrete. Background are similar between 1.5-3 MeV, while the on-site background is less by a factor of 6 above 3 MeV, indicating that the cosmic fluxes are less due to increased overburden, and that there are no excess of neutrons

Excess of neutron flux over environmental level is not measure-able with normal survey equipment, as expected from the reactor design (more than 5 meters of concrete should suppress the neutrons from the core to almost zero level) and as noted in previous experiments (Gösgen, Bugey [5]). Therefore, reactor associated background can be safely assumed to be negligible.

Ambient background at the site will be monitored continuously during the experiment by an additional CsI(Tl) detector coupled to photo-multiplier tube readout.

3.2 Reactor Neutrino Source

Nuclear reactors are prolific source of electron anti-neutrinos. During each fission, a mean of $\sim$ 204 MeV of thermal energy is released together with an average of about 6 neutrinos. Therefore, the total neutrino production rate $\mathrm{R}(\bar{\nu_e})$ at the core of thermal power $\mathrm{P_{th}}$ is given by :

$$\mathrm{R}(\bar{\nu_e}) \;=\; \frac{6 \times \mathrm{P_{th}}}{204\ \mathrm{MeV}}\ \mathrm{s^{-1}} \;=\; 1.8 \times 10^{20}\ \ (\mathrm{P_{th}/GW})\ \mathrm{s^{-1}}\ .$$

The production is isotropic so that the flux $\phi(\bar{\nu_e})$ at our location (28 m from the core of 2.9 GW thermal power) is

$$\phi(\bar{\nu_e}) \;=\; 5.2 \times 10^{12}\ \mathrm{cm^{-2}s^{-1}}\ ,$$

while the flux due to the far core at 102 m will be $0.4 \times 10^{12}\ \mathrm{cm^{-2}s^{-1}}$. The neutrino spectrum is a smooth distribution which peaks at 0.5-1 MeV and extends up to 8-10 MeV.

Extensive efforts have been done on modelling both the flux and the shape of reactor neutrinos [32]. The accuracy has been demonstrated in the Bugey experiment [31] with a "Pressurized Water Reactor" for neutrinos in the energy range of 3 MeV to 7 MeV to the 2% uncertainty level based on 1.2×10^5 measured ($\bar{\nu_e}$ p) events.

The rector neutrino spectrum can be evaluated using some by now standard algorithms which require as inputs the reactor thermal power output and the compositions of the main fissile isotopes (^{235}U, ^{238}U, ^{239}Pu, and ^{241}Pu), their variations during a reactor cycle as well as their spatial distribution inside the core. These data are continuously monitored during the reactor operation, and availability to the experiment has been officially approved by TPC and NP2.

3.3 CsI(Tl) Detector and Photo-diode Readout

Calorimetry using CsI(Tl) crystal with photo-diode (PD) readout is by now a matured technology in high energy physics experiments, where individual crystal weighs several kilogram in mass and an entire calorimeter systems of 40 tons are deployed [7].

The properties of CsI(Tl) crystals [33], together with those of a few common scintillators, are listed in Table 3. The CsI(Tl) crystal offers certain advantages over the other possibilities. It has relatively high light yield and high photon absorption (or short radiation length). It is mechanically stable and easy to machine, and is only weakly hygroscopic.

Meanwhile, silicon PIN photodiodes [34] have several advantages over photo-multiplier tubes : they are operational at much lower voltages, stable, and unaffected by magnetic field. They are compact devices leading to less passive mass and volume, and for low background applications, less intrinsic radioactive contaminants. The typical emission spectrum of CsI(Tl) and the PD spectral sensitivities are shown in Figure 9. The emission spectrum peaks at about 550 nm making the crystal optimal for photo-diode readout. Therefore, the CsI(Tl) plus PD readout combination offers great potentials as gamma-ray detector.

Compared to high energy physics calorimetry, our application in low energy neutrino experiments involves less massive modules (about one kilogram per module instead) but requires better energy resolution at low (sub-MeV) energy and a lower energy threshold of 100 keV, Also very critical is the intrinsic radiopurity (common naturally occuring radioactive contaminations include ^{238}U, ^{232}Th, and ^{40}K) of the crystal itself which must be kept very low.

The CsI(Tl) crystals used in this experiment are developed and produced in close partnership with the manufacturer[4]. Crystals are grown by the "decreasing crucible"

[4] Manufacturer: Unique Crystals, Beijing

(Bridgeman-Stockbager) method using 99.999% pure CsI and TlI powder[5] as raw materials. It takes typically 25 days with one oven to grow a crystal 10 cm in diameter and 30 cm in height which weighs about 6.6 kg. The Tl concentration in the CsI(Tl) crystal is of the range of 0.03-0.12%. All the subsequent processing - cutting, grinding and polishing - are done by the manufacturer.

Each detector unit consists of CsI(Tl) crystal with end surfaces hexagonal in shape with 2-cm sides giving an area of 10.4 cm^2. The length is 20 cm and the mass per crystal is 0.94 kg. Two such crystals are glued together at the end to form a *module*, as depicted schmatically in Figure 10. The crystal surfaces are polished to the "diffused-scattering" grade, and are wrapped by 300 μm thick white teflon reflector to provide diffused reflection for optimal light collection. Two photo-diodes (PD) and pre-amplifiers (PA) are mounted at the two open ends of the module. Output signals from the PA are fed through 5 m cables to back-end electronics.

The characteristic parameters of the photo-diode[6] is listed in Table 4. The active area is 2 cmX1 cm, thus covering 20% of the end surfaces. Initially, the PDs available have the silicon sensors grown on a ceramic substrate which is a known to be a bad material from the radiopurity point of view. After joint efforts with the manufacturer, custom-designed low-background PDs will be used in this experiment. Such PD will be grown on aluminium substrate and will have the signals brought out via a flexible printed circuit made of copper strips, as depicted in Figure 11.

The PD can also work as a solid state detector for low energy photons. Using a commercial pre-amplifier[7], the bare PD gives a FWHM resolution[8] of 8.3% with a 60 keV ^{241}Am X-ray source. This procedure can be used to establish an absolute "number of photo-electrons (pe) per ADC channel" calibration for the system (knowing that the energy to generate an electron-hole pair is 3.62 eV). The pre-amplifier rms noise is 460 pe, while rms noise of the combined PD+pre-amplifier system is 580 pe.

The energy resolution achieved for the ^{137}Cs 667 keV line are 19.6% for one photo-diode at room temperature and 15.3% for two photo-diodes at 5^{o}C. The spectra for ^{137}Cs and ^{60}Co as shown in Figures 12 and 13. The resolution as a function of photon energy

[5]Supplier: Chemtall GMBH, Germany

[6]Supplier: Model S2744-08 SPL2, Hamamatsu Photonics, Japan.

[7]Canberra 2006

[8]All resolution quoted in this article are FWHM

at room temperature is shown in Figure 14 and can be expressed as :

$$\frac{\Delta \mathrm{E}}{\mathrm{E}_\gamma} = 14.7\% \times \mathrm{E}_\gamma(\mathrm{MeV})^{-0.97}$$

The closer approximation to E_γ^{-1} than to $\mathrm{E}_\gamma^{-0.5}$ indicates that the resolution is limited by electronic noise rather than photon-statistics. The variation of light collection (that is, photopeak position) within the crystal active volume is uniform to within 5%. The energy threshold (3σ level above noise) achieved is 70 keV.

The electronic noise (σ_Q) of the PD+PA system can be, to a first approximation, modelled as

$$\sigma_\mathrm{Q}^2 = \mathrm{a}_1 \mathrm{I}_\mathrm{D} \tau + \mathrm{a}_2 \mathrm{C}_\mathrm{in}^2 \tau^{-1} ,$$

where I_D is the PD dark current, $\mathrm{C}_\mathrm{in} = \mathrm{C}_\mathrm{PD} + \mathrm{C}_\mathrm{PA}$ is the total input capacitance, τ is the shaping time, and a_1, a_2 are parameters less likely to be modified. The reverse bias voltage reduces C_PD but increases I_D and hence has an optimal setting. Figure 15 depicts the variation of (a) the light output of CsI+PD+PA, and (a) the energy resolution of the PD+PA system, as a function of time as the system is warmed up from -10°C to room temperature. It can be seen that temperature should be kept possible to minimize dark currents, and this will more than compensate the slight reduction of light output within our range. Practically, we plan to operate the experiment at a 5-10°C ambient temperature, and with good humidity control.

With two standard crystals optically coupled together at the end, the light output as measured by PMTs from the left Q_1 and right Q_2, together with $\mathrm{Q}_\mathrm{total} = \mathrm{Q}_1 + \mathrm{Q}_2$ and $\mathrm{Q}_1 - \mathrm{Q}_2$, as a function of position along the crystal, are displayed in Figures 16 and 17. The achieved resolution (from $\mathrm{Q}_\mathrm{total}$) is 16% at 660 keV, and the longitudinal resolution (from $\mathrm{Q}_\mathrm{L} - \mathrm{Q}_\mathrm{R}$) is 1.3 cm.

Another interesting possibility with CsI(Tl) crystals is its particle identification capabilities with the pulse shape discrimination (PSD) techniques [36], as demonstrated in Figure 18 for our crystal. The time evolution of the scintillation pulse can be approximated as :

$$\mathrm{L(t)} = \mathrm{L}_\mathrm{f} \exp(-\mathrm{t}/\tau_\mathrm{f}) + \mathrm{L}_\mathrm{s} \exp(-\mathrm{t}/\tau_\mathrm{s}) ,$$

where L_f and L_s are the initial amplitudes, while τ_f ($\sim 0.4 - 0.7\ \mu s$) and τ_s ($\sim 7\ \mu s$) are the decay time constants, of the slow and fast components, respectively. The ratio $\mathrm{L}_\mathrm{f}/\mathrm{L}_\mathrm{f}$ increases while the fast component decay constant τ_f decreases with larger dE/dx. That is, alpha particles will have faster and larger fast components than electrons (this is opposite to the effects in liquid scintillator). The PSD technique can help to differentiate alpha pulses and direct photo-diode events (which have very fast pulses) from gamma and electron signatures originating from inside the crystal.

Our applications of the CsI(Tl) calorimetry in low background experiments involves very stringent requirements on the intrinsic radiopurity of the crystal. The ^{238}U and ^{232}Th cascade series, as summarized in Table 5 and 6, respectively, emit alpha-particles of definite energy, besides beta- and gamma-rays. Trace contaminations of these isotopes in the crystal can thus be measured by studying the "alpha-lines" (which have 100% acceptance and detection efficiency), most of them above 3 MeV where the natural radioactivity background is both continuous and low. In the first study on the CsI(Tl) crystal intrinsic radiopurity [35], extremely high sensitivities were achieved, to the level of 10^{-18} and 10^{-22} g/g ^{228}Th contaminations with measurements in an unshielded environment at sea-level and at underground, respectively. Similar measurements have been repeated in a ordinary surface laboratory site on a 30 cmX5 cmX5 cm CsI(Tl) crystal (mass 5 kg) for our candidate manufacturer. The crystal is shielded by 10 cm of lead with cosmic vetos, and read out by with photo-tubes. The measured spectrum is displayed in Figure 19. Structures below 2.5 MeV are mostly from ambient radioactivity (radon, lead, concrete, PMTs ...). The absence of α-lines above 3 MeV implies limits on the ^{238}U and ^{232}Th chains to the level of 10^{-12} g/g. This corresponds to a background rate of less than one disintegration per day per kg of crystal.

This method of evaluating the uranium and thorium content in a material is unique for crystal scintillators - that the α's are only slightly quenched so that one looks for peaks in the much cleaner >3 MeV range (as compared to a 5 MeV α only giving 500 keV electron-equivalence of light). Adding in the pulse shape discrimination properties can potentially boost the sensitivities by another factor of 100 to the 10^{-14} g/g level - just in a surface location! (As compared to solar neutrino projects like SNO and Borexino which has invested tremendous efforts and big underground facilities [37] to get sensitivities down to the 10^{-16} g/g level). This is a very attractive feature for the use of crystal scintillator in future low-background experiments.

3.4 Detector Geometry

The detector unit with two crystals glued together will be the building blocks of various configurations,

In the *active target* mode for $\bar{\nu}_e$-e scattering, the target calorimeter consist of a matrix of 2(Width)X17(Depth)X15(Height)=510 crystals, giving a total mass of 480 kg and occupying a space of roughly 40 cm(W)X60 cm(D)X46 cm(H). The cross-section is depicted in Figure 10. The relevant detector parameters are listed in Table 7. Photo-diodes are mounted at the two open ends.

We have the flexibility of choosing our fiducial volume, outside of which will be used as an ant-Compton veto. As an illustration, the interaction mean free path for 2 MeV photon is about 5.4 cm for CsI and 28.4 cm for liquid scintillator, so that an active veto of 6 cm of CsI is equivalent to 31.6 cm of liquid scintillator.

A full GEANT simulation has been performed to evaluate the suppression factors for photons hitting the detector from outside and producing single hits, as functions of active veto thickness and photon energy, The results are shown in Figure 20. As an illustration, if a 2 MeV photon is emitted isotropically at the surface, there will be 5% probability that it get into the inner target after 2 layer of active veto, and out of those, only 35% will manifest as single hits, giving an overall suppression factor of 2%.

The detection of single electrons in the inner target region has also been studied and the results are displayed in Figure 21. The efficiency is the probability of single electron orginating inside a particular crystal producing only a single hit out of the many crystals. This is close to unity at low energies but drops to about 50% at 5 MeV. The reason of the decrease for high energy electrons is due to radiation loss by bremsstrahlung effects. Both Cs and I are high-Z nuclei and therefore bremsstrahlung cross-section is enhanced by $\sigma(\text{brem.}) \propto Z^2$. A 5 MeV electron on average loses 0.7 keV of energy by radiation (or a "Bremsstrahlung Yield" of 14%) before being stopped in the CsI crystal. When the bremsstrahlung photon leaves the mother crystal and gets absorbed by another cell, it will manifest itself as a multiple-hit event and hence becomes an inefficiency factor in the neutrino-electron scatttering measurements.

3.5 Electronics and Trigger Systems

The electronics readout scheme is depicted schematically in Figure 22. Essentially all the electric boards are designed and built by ourselves.

The photo-diode signals will pass through a pre-amplifier (PA) board mounted at the crystal right behind the PD. The differential output is then transferred over $\sim$5 m of twisted-pair cable to the main amplifier plus shaper circuitries, shown schematically in Figure 23 located outside the shieldings. The entire pulse shape of the amplified output will then be recorded out by a Flash ADC(FADC), whose block diagram is depicted in Figure 24. The system is equipped with two computer controlled threshold voltage adjustors for setting the discriminator levels (one for trigger above an energy threshold, the other above electronics noise level), and signal generator to be fed to the PA for monitor and calibration, the block diagrams of both are illustrated in Figure 25. The logic control module co-ordinating the various modules is displayed in Figure 26.

The timing schematics of the FADC readout is depicted in Figure 24. The amplified analog signals are continuously digitized by the FADC and put into a circular buffer. A trigger signal will create an "Interrupt" which stops the digitization after a certain pre-selected time (around 10 μs), and the valid data can then be read out at the range before the Interrupt. The CLOCK module, depicted schmatically in Figure 26, is provided with frequencies of 5, 10 and 20 MHz, and can be controlled with software via the VME-bus or by an external signal or by a manual push-button.

The schematics of the trigger system is displayed in Figure 27. Cosmic ray muons, which set off an ~MeV threshold from the veto scintillators, will disable the system for a software-selectable time (typically 100 μs), a period necessary to removed delayed effects due to spallation or muon-capture neutrons produced when the muon goes through the system. A simple "online trigger" in the Active Target mode will be adopted. The trigger conditions will include :

- No cosmic Veto, and
- Energy disposition exceeding 500 keV in at least one channel.

After the FADC digitization period, one has the option of holding the system for another software-defined time (typically 1 ms) before reading the data out, to study possible time-correlated delay activities, as discussed in Section 4.3. The computer time when reading out an event (resolution 1 μs), as well as the time between a recorded event and the previous cosmic veto, are also recorded for diagnostic purposes.

For every event, the "hit-map" patterns of the veto scintillators subjected to a low (~100 keV) threshold will be recorded for later diagnostics. The active veto thickness will be determined offline based on actual background, and may depends on energy. Besides the main "physics trigger", various other software-selectable diagnostic tools (such as triggers for cosmic rays, radioactive source calibration, calibration-pulser monitoring, etc.) will be provided. The trigger type will be encoded in a "trigger bit" within the event header. The timing between various prompt and delayed events will be recorded by commercial TDCs[9].

[9] LeCroy TDC1176

3.6 Data Acquisition, Calibration and Monitoring Systems

The VME data acquisition system is selected for this experiment. The FADC, threshold adjustor, calibration pulser, hit pattern unit, gate generator, and trigger interrupt generator all follow the VME protocols, while the non-readout modules (main amplifiers, discriminators, fan-out units) will adopt the NIM conventions. The readout time (or daq dead-time) for an event will be about 1 ms.

The schematics of the DAQ system is shown in Figure 28. The VME modules are read out by by a target processor[10] which runs on the VxWorks[11] operating system with a maximum capacity of 20 Mbytes/s and adopts the C programming language. The VME target-CPU is supported by a UNIX host machine[12] as a boot-server. Data are directly transferred via the Ethernet to the hard disk of a Pentium II/266 PC with LINUX operating system and a maximum throughput rate of 1 Mbytes/s. The VME target processor provides the CPU for zero suppression while that of the the PC will perform event display, online analysis and monitoring, as well as further data compression via the gzip protocol. The data will be duplicated and stored in two local 6.4 Gbytes hard disks. One of the disks will be brought back to our home-base and backed up in 8 mm Exabyte tapes (5 Gbyte storage capacity) for storage and/or via CD-RW writer to CDs (650 Mbytes storage capacity).

The schematic of the data format recorded on disk is shown in Table 8. The "Event Header" provides information on run and event numbers, date and time (resolution to 1 μs), as well as trigger categories, followed by data from the hit-pattern units, TDCs, scalers, input settings (thresholds, gate widths ...), as well as several blank spaces reserved for future expansions. The bulk of the data comes from the FADC.

Taking 50 FADC time bins and an average of 10 channels per event, each event will be 500 bytes in size, so that the hard disk will be able to save 1.3×10^7 events, which can be copied to two Exabyte tapes or 10 CDs. The actual event rate will depend on the background and how loose or stringent the online trigger and veto conditions we set. Practically, one would like to attend the experiment only once a week to swap hard disks during steady state operation. Allowing only half the disk to fill up, This corresponds to a maximum data taking capacity of 70 Hz.

[10] MVME 167, Motorola

[11] Wind River Systems Inc.

[12] Silicon Graphics

The on-line graphic display software, based on the PAW[13] packages, provides tools for event display, monitoring and slow control system. The front panel of the display system, from which different functions can be selected by mouse-botton via X/MOTIF protocols, is shown in Figure 29.

The event-display will show the spatial distribution of hits and the pulse shape of individual channels. Time-integrated parameters (such as number of hits, background energy spectrum, response to cosmic rays etc.) will be monitored on-line in a channel-by-channel basis, and their stability with time will be checked.

All crystals with the complete readout system will be calibrated by common radioactive gamma-sources (like ^{137}Cs, ^{22}Na, ^{60}Co and ^{228}Th), before installation and at regular intervals (one week to one month) during data taking. This will cover the gamma-response range from 500 keV to 2.6 MeV. Temperature effects will be studied. A data base for these performance parameters will be constructed.

Depending on the actual background, peaks from un-removable background sources may also show up as data are accumulated. These may provide the most direct online energy calibration as well as stability monitor. The 511 keV annihilation photons are especially interesting for this purpose. Pair production contribution becomes significant for high energy (more than 3 MeV) photons, and such events have rather distinct topological features : a central hit from the e^-e^+ pair plus two back-to-back hits each having the characteristic 511 keV energy.

A precision software-control calibration-pulser will be used to supply calibration pulses to the pre-amplifier, so that performance and stability of the entire electronics chain can be monitored continuously.

The "slow control" for various operational parameters is done by another PC running either Windows-95 and equipped with the LabView[14] graphic package. Data are recorded on to disks under different files as the data. The ambient conditions, like temperature, humidity, flow rate of circulating gas, etc. affect the performance of both crystals and electronics. Their values will be measured by sensors at a few strategically placed locations. These quantities, together with the low voltages from the various power supplies, will be read out by ADCs on the PC-bus and continuously monitored. The high voltage system[15], which supply the PMTs, is controlled and the operation continuously monitored

[13]Physics Analysis Workstation, CERN, Switzerland

[14]LabView, National Instruments

[15]LeCroy HV Mainframe 1458

via a PC interface with the LabView packages.

During steady state operation, the running conditions will be remotely monitored at the home-base, through the telephone line with MODEM at a transfer rate of 56 Kpbs. Key information will be studied to ensure stable and steady operation. An electronic logbook system, which enables on-site "logbook-type" information to be accessible by every institutes, will be developed at a later stage.

3.7 Shieldings Design

The relatively compact inner target detector (of only 40 cmX60 cmX46 cm in dimension for crystal along) enables an efficient shielding to be built. The schematic layout of the shielding is depicted in Figure 30. while the technical layout on our experimental site is shown in Figure 31. A modular and expandable approach has been adopted in the shielding design. The adopted dimension of various layers are based on the experience of previous reactor neutrino experiments which operated under similar ambient conditions.

The most exterior layer is the plastic scintillator for cosmic ray veto. Each scintillator module has dimension 3 mX0.75 mX3 cm, and are read out by 5-inch PMTs at both ends[16]. The efficiency for detecting traversing muons is more than 98%. Three of these will form a panel to match a side of the shielding structure. Three of the six sides (the top one and two opposite side ones) will be covered by these panels. The geometrical coverage for cosmic muons from these three sides is about 87%. The two remaining sides will be covered with other scintillator panels of smaller size. The bottom side will not have cosmic veto.

The shieldings and inner target will be inside a plastic bag flushed with dry nitrogen to prevent the radioactive radon gas from diffusing into the target regions. Inside the plastic bag is 15 cm of lead, and 25 cm of boron-loaded polyethylene (as $\sim$10% of B_2O_3 by weight). The lead layer attenuate external gamma fluxes whereas the protons in PE serve to slow down the high energy neutrons while the large capture cross sections of ^{10}B enable efficient absorption leaving only 480 keV photons.

Internal to the polyethylene shields and just exterior to the CsI inner target will be 5 cm of oxygen-free-high-conductivity (OFHC) copper. This is one of the best radioactive-wise pure materials and provides shielding to residual background from the lead and PE themselves.

[16]On loan from the CYRNUS Experiment, Los Alamos National Laboratory, U.S.A.

The entire shielding assembly makes up of three parts : (1) a fixed shielding house, (2) a movable trolley on which the target sits, and (3) the front door which can be moved by wheels. The technical drawing for the front door and the trolley is depicted in Figure 32. Access to the target will therefore involve opening the front door and then pulling the movable trolley out. Cables from pre-amplifiers are brought out through cable trays through the corner of the front door. There are two calibration holes at the front door through which radioactive sources can be inserted, while another two gas pipes at the back wall for gas circulation. All the access pipes and trays are bent or come with angles so that there are no direct line-of-sight between the inner target and the external background.

The inner target region will be cooled to 5-10^{o}C by an external cooling system shown schematically in Figure 33, which circulates cooled dry nitrogen gas through plastic pipes. A 4 cm thick thermal insulator will be inserted interior to the copper plates to enclose the CsI target. The PE plates will also serve as additional thermal insulator. An inner space of 90 cm(W)X70 cm(D)X60 cm(H) is available for the crystal target and its associated mechanics and electronics, offering sufficient space for future maneuver and growth, like putting in more target or shielding materials.

Full simulations have been performed to study the attenuation effects for photons and neutrons due to this (and other) shielding configurations, based on GEANT and MCNP [38]/GEANT+GCALOR packages, respectively. Figure 34 shows the attenuation factor for γ's coming from exterior to the shielding assembly towards the target center, while Table 9 summarizes the capture probabilities for neutrons originating at various locations.

In a measurement with similar shielding configurations and comparable overburden [39], it was found that 20 cm of wax is sufficient to attenuate the neutron flux to a saturated level, as illustrated in Figure 35. In addition, a prototype shielding was set up at the AS basement laboratory, with a 5 kg NaI crystal shielded by B_2O_3 powder, 4 cm of paraffin wax and 5 cm of lead, and the principal measurements are illustrated in Figure 36. The effects from a Am/Be neutron-source can be readily seen - neutrons give rise to background mostly in the 3-8 MeV range, and with a distinct end-point at about 8 MeV. The (n,γ) Q-values from the various isotopes can also be identified. The background spectrum at this energy range is smooth and does not show any of the characteristic features for neutrons, indicating that the background is dominated by the various cosmic-ray induced channels, rather than by neutrons.

3.8 Offline Software

Standard software packages and practices in high energy experimentation will be adopted for the experiment. A sketch of the software organization is depicted in Figure 37.

The organization follows the typical sequence of a offline data flow-chart : data taking, refinement, storage, distribution, analysis and eventually publication of results, as elaborated further below :

- **Data I/O:** The offline software will serve as a event reconstruction and detector response simulation machine, which has an input interface with either 4-vector data from physics event generators or raw data from experiments. The results of Monte Carlo will be written as Monte Carlo N-Tuples, while the reconstructed events from raw data will be further refined and stored in the format of DST (Data Summary Tape) or N-Tuples.
- **Data refinement:** This procedure turns pulse shape information from the FADCs in (channel number, energy) arrays, and executes very loose cuts. It will be centrally done in our software base institute.
- **Data base and distribution:** The central data base will be easily accessible and distributed within the collaboration, and protected from intruders. All sites of databases will be brought up to date automatically, or labeled by a clear version tag. Multiple back-ups on optical disks, tapes will be performed, such as on 100-Mbyte floppy disks or ZIP-Drive.
- **Physics analysis:** The DST and N-tuples refined data will be analysed at collaborating institutes. A comparison between data with Monte-Carlo will be crucial for all physics analysis. The mutual tune-up will be according to either experimental systematics or Monte Carlo imperfections.
- **Documentation :** A news bulletin is regularly circulated to every members of the Collaboration via the Internet. Written articles in the form of poposals, status reports and different levels of techincal/physics notes are also made available and accessible. A Web-site[17] allows access gateway to all these information.
- **Publication:** The contents of conference talks or papers to be published will be circulated within the Collaboration, and results will be approved in advance by the Collaboration before being made public.

[17] http://hep1.phys.sinica.edu.tw/EXONO/index.html/

Physics and detector simulations will be based on GEANT (Version 3.21), complemented with the support of neutron transport code by MCNP [38], a standard package in nuclear engineering. Code management is performed by PATCHY (Version 5.03/14), while event and other graphics display will be based on HIGZ (X11 Version). Fortran coding conventions will be adopted, supported by the standard CERN software library packages such as HBOOK, HPLOT and CERNLIB. Data analysis will be performed in the PAW (Version 2.07/02) platforms, with the KUMAC macros and Fortran-callable subroutines. The data storage format will be either in DST or in N-tuples.

4 Background Discussions

Experimental neutrino physics is primarily the art of building massive detectors while keeping the cost and background low. The understanding and control of background is crucial to all neutrino experiments. Since the expected cross-sections of the process we are going to investigate in this experiment are very small (range of $10^{-45}\mathrm{cm}^2$), the background control will require state-of-the-art solutions.

In this section, the various background processes expected for this experiment will be discussed, and measures to suppress or identify them will be described.

4.1 Cosmics Rays

The experimental site is at the lowest floor of the NP2 reactor building, and an overburden of about 10 m of concrete, giving 20-30 mwe of overburden. This will be sufficient to effectively attenuate the hadronic component from cosmic rays.

Cosmic muon flux, however, are reduced by a small factor to the level of 34 $\mathrm{m}^{-2}\mathrm{s}^{-1}$. Besides directly hitting the CsI target, they can also produce bremsstrahlung photons (which is in coincidence with the muons) or neutrons (which will give rise to a delayed pulse when they are captured) from the surrounding materials. The cosmic bremsstrahlung spectra originate dominantly by δ-electrons from the muons, and are peaked at low energies [40].

The CsI target and the shielding walls will be covered on five sides by plastic scintillator as cosmic ray veto. The veto scintillators have more than 98% efficiency of tagging a traversing muon. The veto signal will disable the data acquisition system for 100 μs to cover the range of delayed background due to associated neutrons.

4.2 Ambient Radioactivity

Natural radioactive background consists mostly of ^{40}K, as well as the ^{238}U and ^{232}Th chains, the decay sequence of which are shown in Table 5 and 6, respectively. The radioactivity level of the selected sites at NP2 has been measured with TLDs and NaI detector, and the background spectra are shown in Figure 8. The on-site γ background is about factor of 20 above the typical laboratory background level at energy below 1.4 MeV, while a factor of 6 less for energy above 3 MeV, as explained in Section 3.1. The measured rates for the 5 kg NaI detector are 5170 Hz for 0.5-3 MeV and 0.36 Hz for 3-8 MeV.

To suppress the ambient background, the inner target will be surrounded by shielding materials: 15 cm of lead and 25 cm of polyethylene and 5 cm of copper, attenuating 2 and 5 MeV gamma fluxes by factors of 2×10^{-5} and 10^{-4}, respectively, as depicted in Figure 34. Coupling the measured spectra and the attenuation factors, the estimated background rate from ambient radioactivity is given in Table 11, indicating that the suppression of this background to below the signal level should be possible.

The environment usually contains traces amount of radon gas (^{220}Rn and ^{222}Rn are intermediate isotopes in the ^{232}Th and ^{238}U cascade chains shown respectively in Table 5 and 6) which typically gives rise to 40 Bqm^{-3} of activity. To prevent the radon gas from diffusing into the target region, the entire shielding will be covered by a plastic bag flushed with dry nitrogen from the gas circulation and cooling system. The purity level of air less than the 10^{-3} level is required.

4.3 Radioactivity from Internal Components

Detector compontents which will be located inside the lead shieldings have to be free from, or at least minimized in, radioactive contaminants. "Rule-of-thumb" experience from previous experiments [41] has been adopted in the first selection of materials. Extensive measurements have been carried out on the candidate materials with low background germanium detectors (which are normally used for environmental radiopurity measurements). A summary of the results is shown in Table 12.

As an illustrations, a typical spectra measured with the germanium detector is given in Figure 38, in the case of an early sample of CsI(Tl) crystal. The various lines are from natural background due to ^{40}K (1461 keV), ^{238}U (1764 keV and others) and ^{232}Th (2614 keV and others) series. In this particular measurement, an intriguing excess was observed at 660 keV, which can be interpreted as ^{137}Cs contamination at a level of 5×10^{-17} g/g. This excess was not repeated again in subsequent samples. The suspicion is that the first sample had been contaminated by inappropiate handling when exposed to a ^{137}Cs source during previous measurements.

Some of our radiopurity measurements which affect the experimental design features include:

- The common "fiber glass" circuit boards have consistently revealed the contaminations by ^{238}U and ^{232}Th cascade isotopes in different samples. Accordingly, the "bread board" ciruit boards, which gave negative results to these isotopes, will be adopted in the construction of the pre-amplifier circuits.
- Boron carbide B_4C is commonly used in loading polyethylene as neutron absorber. It is found to have small activity, and therefore, boron oxide B_2O_3 has been selected as the loading materials.
- The commercially available photo-diode[18] is found to be radioactive, due to the use of ceramics as backing materials. Based on joint efforts with the manufacturer, including the measurements of epoxy resin and flexible printed circuit (FPC) which give negative results, a custom-designed photo-diode using aluminium as backing and FPC as readout, will be used in the experiment.

Residual radiopurity from the lead, polyethylene and B_2O_3 are attenuated by the 5-cm OFHC copper plates, a known radioactive-clean materials used extensively in inner shieldings for low background measurements. The inner target "fiducial" region is further shielded by the outer CsI modules serving as active veto, the thickness of which can depend on energy, will be determined *a posteriori* based on actual background.

The fiducial target region consists only of two materials: CsI(Tl) crystals and teflon wrapping sheets. Radioactivity from the PD and PA are further attenuated by the active veto. The attenuation factors, as function of photon energies and veto thickness, are shown in Figure 39. It can be seen that, with 5 cm of veto thickness, only about 1% of the photons from the PD+PA region will produce a single hit, and this is an attenuation factor of 10 compared to the case when there is no active veto-buffer. Known radioactive-wise pure materials, like OFHC copper and acrylic, will be used as far as possible in the target region mechanics.

[18] Hamamatsu S2744-08

The radiopurity of the CsI(Tl) crystal itself is therefore particularly crucial. The CsI(Tl) is an active element and therefore has 4π solid angle for absorption and is subjected to both internal β and α background (which have higher energies compared to the γs as well as 100% acceptance and detection efficiencies). Alpha particles can be identified easily through their pulse shape discrimination properties, whereas single beta-decay without associated γ-rays, will be a potential background. A list of these "lone" β-decays from the ^{238}U and ^{232}Th series is tabulated in Table 10. Some of these decays can be tagged through their characteristic timing sequence.

As described in Section 3.3, background measurements have been performed with crystal produced by the candidate supplier, and the results are shown in Figure 19. The absence of alpha lines above 3 MeV implies limits on the ^{238}U and ^{232}Th chains to be below the level of 10^{-12} g/g, which corresponds to less than one decay per kg of crystal per day, an acceptable level.

In addition, the CsI(Tl) crystal has been subjected to a "neutron activation analysis" (NAA) which is sensitive also to stable trace contaminants. It was found to consist of about 40 ppm of ^{23}Na. This is stable but can undergo neutron capture (n, γ) ($\sigma \sim 0.4$ b) to give ^{24}Na, which is beta-emitter with $\tau_{\frac{1}{2}} = 15$ h and a high Q-value of 5.5 MeV. From the composition and cross-section ratios, the effects are expected to be at only a sub-ppm level compared to those due to neutron captures by ^{134}Cs and ^{127}I, as discussed in Section 4.4. The ^{40}K contamination from NAA is also less than the ppb level.

Gamma-rays, be they from ambient or internal background sources, are emitted in fixed energies and the lines from the usual radioactive contaminants (^{40}K, ^{238}U and ^{232}Th series) are known. Since the CsI detector has good energy resolution to gammas and is efficient in fully absorbing the photons, the background gamma background may show up as discrete lines. These will help both in real time energy calibration and in the understanding and subtraction of background (for instance, one can veto events with an energy deposition of 1.4 MeV - the gamma line from ^{40}K).

4.4 Neutrons

Neutrons at a shallow depth can be produced in the surrounding structures or in the shielding and target themselves, via various cosmic-induced interactions.

Ambient neutrons are produced not only by cosmic-induced interactions, but also from ^{238}U fissions and (α,n) processes in the rock or concrete wall. The measured flux at a 17 mwe site is 8×10^{-5} cm^{-2}s^{-1} [39]. As indicated in Table 9, ambient neutrons exterior to the shieldings have practically no chance of hitting the inner target. Part of them, however, can be captured in the lead or polyethylene producing gamma-rays which will be attenuated by the shielding materials or the active veto walls. In particular, (n,γ) reactions from ^{207}Pb (22% isotopic abundance, $\sigma \sim$0.4 b) will produce high energy mono-energetic gamma-rays: 6.73 MeV (BR 5%) and 7.37 MeV (BR 94%). The suppression factors of γ's produced uniformly and isotropically in the lead shieldings to hit the inner target are depicted in Figure 40, showing a 10^{-3} attenuation for the 7 MeV photons.

Neutrons produced in the shielding and target materials require special attention. There are two cosmic-induced mechanisms where neutrons are produced :

1. **Spallation**, which is the deep inelastic scatterings of muons on nuclei

$$\mu^{\pm} \ + \ \mathrm{N} \ \rightarrow \ \mu^{\pm} \ + \ \mathrm{X} \quad ,$$

   where the neutrons are part of the components from the hadronic shower X. The interaction rate depends on the number of nucleons and hence approximately proportional to the mass of the target.

2. **Muon capture** [42], which takes place when muons are stopped and subsequently captured by the nuclei via :

$$\begin{aligned} \mu^{-} \ + \ (\mathrm{A,Z}) \quad & \rightarrow \quad (\mathrm{A,Z-1})^{*} \ + \ \nu_{\mu} \quad , \\ (\mathrm{A,Z-1})^{*} \quad & \rightarrow \quad (\mathrm{A-Y,Z-1}) \ + \ \gamma\,'\mathrm{s} \ + \ \mathrm{Y \ neutrons} \quad , \end{aligned}$$

   where Y can be 0,1,2,..... with $< \mathrm{Y} > \sim 1.2$. The energy of the neutrons emitted is at the 0.1-10 MeV range (determined from the energy sharing between the neutrons and the ν_{μ} for the 105 MeV muon rest mass), peaking at 0.5-1 MeV. The fraction of muon capture to muon decay is a function of Z and is depicted in Figure 41.

The measured production rates at a 17 mwe site are 240 and 11 kg^{-1}day^{-1} for lead and wax, respectively [39].

The neutrons emitted will then slow down in the materials and eventually be captured by the nuclei mostly via the (n,γ) processes. The gamma-ray produced during spallation, neutron emission or neutron capture are time-correlated with the initial cosmic-muons, and hence can be tagged by the cosmic-veto with a delayed time. The typical time delay distributions for neutron captures in the lead, PE and CsI target are shown in Figure 42. The time profiles indicate different features. The (n,γ) capture cross-sections are large for CsI, while the thermalization of neutrons is inefficient, so that neutrons are mostly captured at high energies within 1 μs before being thermalized. In the polyethylene, neutrons are thermalized quickly and then captured by the ^{10}B in the 10 μs range. Lead has poor cross-sections for both thermalization and captures, and hence both high-energy and thermalized captures contribute. A extended cosmic veto of 100 μs will eliminate most of these background.

The more problematic background are due to the long-lived (longer than ms) unstable isotopes created by the neutron capture mainly via the (n, γ) for thermal neutons, but can also be with the (n,p), (n,α), (n,2n) .... etc. processes for fast (10 MeV range) neutrons. Among the various materials, (n,γ) capture by the target isotopes [43]:

$$\begin{aligned} n \; + \; ^{133}\mathrm{Cs} \quad &\rightarrow \quad ^{134}\mathrm{Cs} \quad (\sigma = 30 \text{ b} \; ; \mathrm{Q} = 6.89 \text{ MeV}) \; ; \\ n \; + \; ^{127}\mathrm{I} \quad &\rightarrow \quad ^{128}\mathrm{I} \quad (\sigma = 6 \text{ b} \; ; \mathrm{Q} = 6.83 \text{ MeV}) \end{aligned}$$

have relatively large cross-sections and will create the unstable

$$\begin{aligned} ^{134}\mathrm{Cs} \quad &: \quad \tau_{\frac{1}{2}} = 2.05 \text{ yr} \; ; \; \mathrm{Q}_{\beta^-} = 2.06 \text{ MeV} \quad \text{and} \\ ^{128}\mathrm{I} \quad &: \quad \tau_{\frac{1}{2}} = 25 \text{ min} \; ; \; \mathrm{Q}_{\beta^-} = 2.14 \text{ MeV} \end{aligned}$$

whose decay schemes are displayed in Figure 46. In particular, ^{128}I has a 79% branching ratio of having a lone beta-decay (without associated gammas) with end-point energy of 2.14 MeV. This will be an irreducible background for the ($\bar{\nu_e}$ e) scattering at low energies. As indicated in Table 9, neutrons from outside the shieldings or originated from the lead have little probability of being captured by the CsI crystal target. About 25% of the neutrons (1 MeV range) generated at the target will be captured by the target itself. It is crucial that the experiment can provide an independent measurement of the neutron capture rate by the target to subtract off this background channel, as discussed in Section 4.6

Another potential background of concern is the long-lived isotope ^{16}N produced by the muon capture of ^{16}O in B_2O_3 for the polyethylene loading:

$$\mu^- \; + \; ^{16}\mathrm{O} \; \rightarrow \; ^{16}\mathrm{N} \; + \; \nu_\mu \quad ,$$

followed by the beta-decay of ^{16}N (Q=10.4 MeV ; $\tau_{\frac{1}{2}} = 7.2$ s) :

$$^{16}\mathrm{N} \; \rightarrow \; ^{16}\mathrm{O} \; + \; \mathrm{e}^- \; + \; \bar{\nu_\mathrm{e}} \; + \; \gamma \;\; (\mathrm{E}_\gamma = 6.13 \text{ MeV} \; ; \; \mathrm{BR} = 68\%) \; ,$$

as depicted in Figure 47. This background channel will probably exclude the option of using B_2O_3 as passive target materials in later experiments. It is, however, acceptable as the loading material for polyethylene, since the amount is small and there are further suppression factors due to solid angle and attenuations from the copper plate and active veto.

4.5 Reactor-ON Correlated Background

Previous experiments with reactor neutrinos [5] indicated that gamma and neutron background associated with "reactor-ON" are essentially zero outside the reactor core and within reasonable shieldings.

Neutrino-induced background, however, requires further attention. The dominant channel

$$\bar{\nu}_e + p \rightarrow e^+ + n$$

has a cross section about 100 times higher than that from ($\bar{\nu}_e$-e) and therefore these events have to be minimized and identified. The target region is essentially proton-free : it consists only of the CsI(Tl) crystals and teflon wrapping sheets, while the materials in proximity include silicon photodiode, fluoro-carbon coated cables. circuit boards and other pre-amplifier components with a total mass much much less than the 500 kg CsI from the target. The e^+-delayed neutron capture signatures can be efficiently identified, though the subsequent decays of the unstable ^{134}Cs and ^{128}I may contribute to background.

Several tons of polyethylene will be used as the inner shielding for neutrons. They will provide an abundant source of protons for the ($\bar{\nu}_e$ p) interactions. The prompt e^+ will only give rise at most to a 511 keV gamma, efficiently vetoed by the wall, while the neutron (energy range 1-10 keV) will be mostly captured by the ^{10}B in the polyethylene or at the innermost B_4C plates, producing only 480 keV gammas, but no long-lived unstable isotopes.

4.6 Absolute Background Measurements

Previous reactor neutrino experiments almost exclusively use the "Reactor ON − Reactor OFF" technique to extract their signals. This method may encounter its limitations with the future "long-baseline" reactor neutrino oscillation experiments [6] whose source may be due to many reactor cores and it is impossible to switch them off at the same time. In a similar spirits, proving the capability of observing neutrinos from the Sun in future real-time solar neutrino experiments [13] can be subtle and non-trivial, since one cannot switch off the Sun.

The CsI(Tl) detector will have more analysing power for background studies because of the better gamma response and its granularity. In particular, one will make an attempt to evaluate the absolute intrinsic radiopurity, as well as external gamma and neutron flux *at* the inner target. Such background subtraction techniques through consistent measurements and modeling have been routinely used in high energy experiments. Whether they can be applied in low energy neutrino experiments in our case remains to be demonstrated. (Double beta decay experiments with ^{76}Ge do employ such techniques [44], having the capabilities of measuring accurately the background γ-lines.) It can be considered as one of the experimental challenges of the pilot experiment and its success may have implications in future projects.

4.6.1 Intrinsic Radiopurity

The crystal scintillator is well suited to accurately measure the intrinsic radiopurity level for the ^{238}U and ^{232}Th chains, assuming that they are in secular equilibrium. The signatures to α's are distinct and unique (high energy due to little quenching, and with pulse shape discrimination), and being a solid, the various isotopes in a cascade will remain at the same location, unlike gaseous or liquid detectors.

The ^{238}U cascade can be tagged by the β-α space- and time-correlated events through the ^{214}Bi$-$^{214}Po decays:

$$^{214}\mathrm{Bi} \rightarrow {}^{214}\mathrm{Po} + \bar{\nu}_e + e^- + \gamma's \; (\mathrm{Q} = 3.28 \ \mathrm{MeV} \; ; \; \tau_{\frac{1}{2}} = 19.7 \ \mathrm{min}) \; ,$$

$$^{214}\mathrm{Po} \rightarrow {}^{210}\mathrm{Pb} + \alpha \; (\mathrm{Q} = 7.8 \ \mathrm{MeV} \; ; \; \tau_{\frac{1}{2}} = 164 \ \mu\mathrm{s}) \; ,$$

as depicted in Figure 43. Similarly, the ^{232}Th series can be identified by the α-α tag from the ^{220}Rn$-$^{216}Po decays:

$$^{220}\mathrm{Rn} \rightarrow {}^{216}\mathrm{Po} + \alpha \; (\mathrm{Q} = 6.4 \ \mathrm{MeV} \; ; \; \tau_{\frac{1}{2}} = 55 \ \mathrm{s}) \; ,$$

$$^{216}\mathrm{Po} \rightarrow {}^{212}\mathrm{Pb} + \alpha \; (\mathrm{Q} = 6.9 \ \mathrm{MeV} \; ; \; \tau_{\frac{1}{2}} = 0.15 \ \mathrm{s}) \; ,$$

and the β-α tag from the ^{212}Bi$-$^{212}Po decays:

$$^{212}\mathrm{Bi} \rightarrow {}^{212}\mathrm{Po} + \bar{\nu}_e + e^- + \gamma's \; (\mathrm{Q} = 2.24 \ \mathrm{MeV} \; ; \; \tau_{\frac{1}{2}} = 60.6 \ \mathrm{min} \; ; \; \mathrm{BR} = 64\%) \; ,$$

$$^{212}\mathrm{Po} \rightarrow {}^{208}\mathrm{Pb} + \alpha \; (\mathrm{Q} = 8.9 \ \mathrm{MeV} \; ; \; \tau_{\frac{1}{2}} = 304 \ \mathrm{ns}) \; ,$$

shown in Figure 44. The second decay-series is a direct measurement of the 2.614 MeV γ-ray (the highest energy photon in natural radioactivity) intensity, which originates from the alternative (BR=36%) decay of ^{212}Bi to ^{208}Tl:

$$^{212}\mathrm{Bi} \rightarrow {}^{208}\mathrm{Tl} + \alpha \; (\mathrm{Q} = 6.2 \ \mathrm{MeV} \; ; \; \tau_{\frac{1}{2}} = 60.6 \ \mathrm{min} \; ; \; \mathrm{BR} = 36\%) \; ,$$

$$^{208}\mathrm{Bi} \rightarrow {}^{208}\mathrm{Pb} + \bar{\nu}_e + e^- + \gamma's \; (\mathrm{Q} = 5.0 \ \mathrm{MeV} \; ; \; \tau_{\frac{1}{2}} = 3.1 \ \mathrm{min}) \; ,$$

where the BR for the the 2.614 MeV γ-ray emission is 100%, as displayed in Figure 45.

Knowing the contamination level of both series, the contribution to the background spectra can then be modeled and subtracted off.

4.6.2 Gamma Flux

Gamma-rays with energies more than 3 MeV have a substantial pair-production cross section. Some of the events will exhibit the unique "single escape (SE) " (central cell having energy of $E(e^+e-)$+511 keV while a neighbouring cell having an energy of 511 keV) or "double escape (DE) " (central cell having energy of $E(e^+e-)$ while two back-to-back cells each having a 511 keV gamma) signatures. The absolute gamma-flux at a particular cell location can then be evaluated by :

$$\phi(E_\gamma = E_{e^+e^-} + 2m_e) = \frac{N_{obs}(SE \text{ or } DE)}{\sigma(\gamma \to e^+e^-)\ \epsilon(SE \text{ or } DE)}$$

where N_{obs} is the observed number of events, $\sigma(\gamma \to e^+e^-)$ is the theoretically known pair-production cross section at E_γ, and ϵ(SE or DE) is the E_γ-independent efficiencies based on simulations for SE (about 17%) or DE (about 7%) , respectively. Knowing the gamma flux at energy E_γ as a function of cells, their contributions to the background via photo-electric effects, Compton scatterings, and pair production with both 511 keV photons re-captured in the same cell, can be evaluated accordingly.

In addition, a 500 kg CsI target can be considered as a total absorber of photons (apart from the smaller edge effects which can be modeled). Accordingly, the total energy spectrum is, to a good approximation, *the* absolute γ-flux hitting the detector. Having the measured absolute flux, the expected background spectra under various fiducial and geometrical definitions can be evaluated by simulations.

4.6.3 Neutron Flux

Similarly, the absolute neutron flux at the target region can be measured through the unique signatures due to the decays of ^{134}Cs and ^{128}I :

$$^{134}Cs \rightarrow \ ^{134}Ba + e^-(Q = 0.66 \text{ MeV}) + \gamma(0.76 \text{ MeV}) + \gamma(0.60 \text{ MeV})$$

which has $\tau_{\frac{1}{2}}$=2.05 yr and branching ratio 71%, giving rise to a triple coincidence with two characteristic gamma energies, and

$$^{128}I \rightarrow \ ^{128}Xe + e^-(Q = 1.70 \text{ MeV}) + \gamma(0.44 \text{ MeV})$$

with $\tau_{\frac{1}{2}}$=25 min and branching ratio 13%, leading to a double coincidence. Their decay schemes are depicted in Figure 46. The difference in lifetimes may make the interpretation of data more subtle : for instance, the amount of ^{134}Cs decays is sensitive to neutron flux at the crystal over the last few years rather than the immediate present.

A complementary method to evaluate the neutron capture rates on the CsI target is to measure the prompt-gamma flux (with or without coincidence with cosmic muons) of energy at the 6.8 MeV region, the Q-value for (n,γ) on ^{133}Cs and ^{127}I [43]. Again, knowing the absolute neutron capture rate at the target, the background spectra under different conditions can be studied.

4.7 Overall Considerations

The control *and* understanding of the background are the most crucial ingredient of *any* neutrino experiments. The success of the pilot experiment (that is, achieving the physics potentials as noted in Section 5) requires state-of-the-art solutions in this arena. On the hand, the experience of tackling this problem will place the Collaboration in a favorable position in future projects along the directions of low-background experimentations (such as dark matter and solar neutrino experiments).

Summarizing this section, several key conditions should be met in performing the pilot experiment:

1. The CsI(Tl) production should be done with care so as to maintain the 10^{-12} g/g of ^{238}U and ^{232}Th purity level.
2. Teflon is a known clean materials. Precautions should be exercised so as not to have dust and dirt attached to the surface during crystal-wrapping.
3. Cosmic-ray veto should be maintained at the >98% level, both in terms of geometrical coverage and scintillator efficiency.
4. Acrylic and OFHC copper should be used as inner target mechanics construction materials. High radiopurity materials should be selected and tested for the other components (photo-diodes, pre-amplifiers, cables). Inner target region should be flushed with dry nitrogen to purge out the radioactive radon.
5. Independent measurements on the various background sources - intrinsic radiopurity, external γ-flux, and neutron capture on target - should be devised. Particular critical is the single beta-decay from ^{128}I produced by (n,γ) on ^{127}I.

5 World-Status and Projected Sensitivities

The sensitivities of the experiment will depend critically on the background level one can actually achieve. Since the CsI calorimeter is a new technique for low-background physics, there is no previous guidance for the background estimation. In estimating the sensitivities in this section, we adopt the assumption that our background level would be that of "the last best experiment" scaled with the surface area.

5.1 Neutrino-Electron Scattering

Neutrino-electron scatterings have been well studied at the accelerator with GeV range neutrinos, mostly ν_μ and $\bar{\nu_\mu}$ [45]. An accuracy of 3% for the measurements of $\sin^2\theta_{\rm W}$ and $g_{\rm A}$ have been achieved, and the results are shown in Figure 2.

Electron antineutrino-electron ($\bar{\nu_e}$ e) scatterings, however, have been observed with reactor neutrinos [15, 16, 17] but not well measured. Some new experiments are now under construction [18]. A summary of previous and present generation of experiments, together with the relative merits in comparison with the CsI experiment, is listed in Table 13. The typical range of accuracy is only 30-50% for the cross-section (and hence the $\sin^2\theta_{\rm W}$) measurement, and a limit of 10^{-9}-10^{-10} Bohr magneton ($\mu_{\rm B} = \frac{\rm e}{2\rm m_e}$) for the neutrino magnetic moments. Electron neutrino-electron ($\nu_{\rm e}$ e) scatterings have also been observed with accelerator neutrinos with similar accuracy [46].

In particular, the W-Z interference in ($\nu_{\rm e}$ e) at $\sim$30 MeV has been demonstrated to be destructive (negative) at a 5σ level by an accelerator experiment at LAMPF [46]. Reactor experiments, probing ($\bar{\nu_e}$ e) at $\sim$MeV scale, do not give very solid conclusion yet, as summarized in Table 14, where various theoretical scenarios are compared with the results from the Savannah River experiment [15] which quoted best uncertainties. Accordingly, Ref. [12] stated that "Thus, it can be concluded that reactor experiments to date provide some evidence for destructive interference; however, they do not strongly exclude the possibility of constructive interference, nor do they prove that there is any coherent interference in the first place. Experiments with greater precision are needed to settle these issues."

As shown in Table 14, the Savannah River experiment [15], although quoting the best accuracy (30% in the cross-section measurement), measured a high central value of $\sin^2\theta_{\rm W} = 0.29 \pm 0.05$. Subsequently, a re-analysis of the results [11], based on an improved reactor neutrino spectrum and the Standard Model $\sin^2\theta_{\rm W}$ value, suggested that the measured ($\bar{\nu_e}$ e) cross-sections at 1.5-3.0 MeV and 3.0-4.5 MeV are 1.35±0.4 and 2.0±0.5 times larger than expected, respectively. Therefore, there are motivations and interests to improve on this difficult measurement further.

In the simple extensions of the Standard Model, massive Dirac neutrinos can acquire through radiative corrections an anomalous magnetic moment [47]

$$\mu_\nu = \frac{3 G_F e m_\mu}{8\sqrt{2}\pi^2} = 3.2 \times 10^{-19} m_\nu(\mathrm{eV})$$

which, though non-zero, is too small to be observable experimentally or through their effects on astrophysical phenomena. However, models incorporating new particles or right-handed currents or transition moments for Majorana neutrinos can produce μ_ν as high as 10^{-10} μ_B [48].

The best neutrino magnetic moment limit on $\bar{\nu_e}$ from reactor was by the Rovno experiment [17] which obtained $\mu_\nu < 1.5 \times 10^{-10}$ μ_B at 68% C.L. from a detector threshold of 600 keV. The anomalous measured cross-section of the Savannah River experiment [15], to be taken literally and liberally, can be interpreted to be consistent with a μ_ν at the range of (2-4)X10^{-10} μ_B [11].

Neutrinos with magnetic moments as large as 10^{-10} μ_B will have an important role to play in stella physics. Inversely, astrophysical observations can help settling limits on μ_ν but only via highly model-dependent parameters-specific calculations. The time duration of the supernova SN1987A burst implies $\mu_\nu < 1 - 20 \times 10^{-13}$ μ_B [49]; stella cooling leads to $\mu_\nu < 0.3 - 1 \times 10^{-11}$ μ_B [50] ; while Big Bang Nucleosynthesis allows at most one neutrino with $\mu_\nu > 5 \times 10^{-11}$ μ_B [51].

Indeed, in the late 1980's, there were intense interest of an anomalous neutrino magnetic moments of range $\mu_\nu \sim 10^{-10}$ μ_B as a solution to the Solar Neutrino Puzzle. Solar neutrinos (ν_e), which are produced at the center of the Sun, may flip their spin on their way out while crossing the solar magnetic field at the Sun's surface and become the right-handed sterile state [52]. This speculation predicts the solar neutrino flux observed on Earth is modulated by the 11 yr solar cycle. Some statistical analysis suggested there exists such a correlation [53] with the ^{37}Cl solar neutrino experiment [54] while this conclusion was contradicted by other work [55]. The Kamiokande solar neutrino data [56], however, does not show any time variation.

As shown in Table 13, the planned TEXONO experiment with CsI(Tl) crystals will improve over previous experiments by having a higher target electron number, and by being more compact in size so that shielding from external gammas and neutrons can be made more efficient. The CsI experiment does not have as good modularity as Rovno [17] or NUMU [18], and hence may not be able to achieve the low thresholds as these experiments may do.

In reactor neutrino experiments, the statistical accuracies are usually limited by the relatively short duration of the "Reactor-OFF" period. Assuming all experiments have similar length of this OFF period, then the ratio of statistical uncertainties (R_δ) among experiments can be given by

$$R_\delta \sim \frac{\sqrt{R_B}}{R_S}$$

where R_B and R_S are the ratios of background and signal among the experiments, respectively.

Displayed in Figure 48 is the projected statistical uncertainties relative to the Savannah River experiment [15] (i.e $R_S = 3.6$ from Table 13), with different cases where the background would be constant or scaled by the surface area, volume or mass ratios between the two detectors. It can be seen that in the reasonable case where the background would scale by detector surface area (giving $R_B = 3.3$), the CsI experiment can improve the uncertainties to 45% of the Savannah River experiment, so that a 14% measurement of the $\bar{\nu}_e$e cross-section is possible. This will be able to give a clear-cut distinction among the different W-Z interference scenario. With a 14% measurement accuracy and a threshold of 1 MeV, the magnetic moments the experiment can probe to will be down to the range of 8×10^{-11} μ_B.

5.2 Neutrino Interactions on Deuteron

The summary and relative merits between previous experiments [19, 20] and the proposed CsI detector on the measurements of reactor neutrino-deutron cross sections are tabulated in Table 15. The CsI detector will be sensitive to neutrons (whose signatures are high energy gamma bursts after neutron capture by gadolinium) and γ-rays, and hence will represent a major improvement over previous techniques with ^{3}He proportional counters which are sensitive only to neutrons. Accordingly, the experiment can differentiate efficiently the signals :

$$\begin{aligned} \mathrm{CC} : \bar{\nu}_e + d &\rightarrow e^+ + n + n \text{ , and} \\ \mathrm{NC} : \bar{\nu}_e + d &\rightarrow \bar{\nu}_e + p + n \end{aligned}$$

from the background

$$\bar{\nu}_e + p \rightarrow e^+ + n \text{ , and}$$

$$\gamma + d \rightarrow p + n$$

which would otherwise be indistinguishable in a γ-insensitive detector. In addition, the $\bar{\nu}_e$d-CC events will not contaminate the $\bar{\nu}_e$d-NC sample if one of the neutrons is undetected since there will be two back-to-back 511 keV γs preceeding them.

Relative to the Savannah River experiment [19] and including the ratios in neutrino flux, target mass and detector efficiencies, one gets R_S of 2.9 and 1.4 for CC and NC, respectively. The improvement is mainly due to an estimated neutron detection efficiency of 90%. The goals and realistic assumptions are that one can reduce the background to a relative ratios of 0.1 and 0.3 for the CC and NC, respectively. This will lead to an improvement of the statistical uncertainties to 10% (NC) and 40% (CC) of the Savannah River results. Since systematic uncertainties including the neutrino spectra are at the few % level, an overall accuracies of 5% for $\bar{\nu}_e$d-CC and 10% for $\bar{\nu}_e$d-NC can be achieved.

Comparison between the measured and expected CC/NC ratio is a sensitive way to search for neutrino oscillations, being insensitive to the detailed knowledge of the neutrino source. This will be the important measurement the SNO solar neutrino experiment [24] will pursue. The Savannah River experiment made an attempt to measure this ratio and compare with theoretical calculations [21]. They got

$$\mathrm{R} = \frac{(\mathrm{CC/NC})_{\mathrm{expt}}}{(\mathrm{CC/NC})_{\mathrm{theo}}} = 0.40 \pm 0.22$$

leading to claims that there are oscillations [57]. The claim, while creating heated discussions and attention, was shown to be inconsistent with the null-results from a host of other reactor oscillation experiments [5]. The Savannah River group never published new results on this measurement, except there is a brief paragraph in a conference proceedings review [58] stating that the double ratio is modified to $\mathrm{R} = 0.74 \pm 0.23$ due to event selection errors. The Deiton experiment [20] did not give an explicit value on this double ratio, but inference from their results will give $\mathrm{R} = 0.88 \pm 0.33$. Given the importance and implications of this measurement, an experiment with improved accuracy adopting a complementary technique will be highly worthwhile.

5.3 Neutrino Interactions on Nuclei

Low energy neutrino interactions on nuclei have not been experimentally studied except for the case of a few light nuclei (^{1}H, ^{2}H and ^{12}C). We will be venturing into a previously unexplored domain when we perform the measurements of reactor neutrinos on ^{10}B, ^{11}B and other nuclei. Since the experimental signatures are the γ-lines with the characteristic energies, the CsI(Tl) calorimeter will be well-suited to investigate these processes. There is a distinct potential for the CsI experiment to "open up a new field".

There are no calculations so far on the $\bar{\nu}_e$N-CC processes with reactor neutrinos, although the extreme cases of ^{3}He and ^{209}Bi have been considered for neutrinos from the Earth's core [30]. The $\bar{\nu}_e$N-NC cross-sections have been surveyed for many nuclei by H.C. Lee in the late 70's [22]. Some of the predictions are listed in Table 16. Recently, with the new input of strange quark content in the nucleon [26] and the axial isoscalar neutral-currents [25], as well as the interest on the BOREX solar neutrino proposal, the cross-sections of ^{11}B [27] and ^{10}B [28] have been re-calculated. The results, using the reactor neutrino spectra with a flux of 2×10^{13} cm^{-2}s^{-1}, are also shown in Table 16.

Scaled to our flux on site, the estimated event rates for the 3 excited states of ^{11}B (2.11, 4.44, and 5.02 MeV) are 7.1, 0.77 and 0.51 (100 kg boron)$^{-1}$day^{-1}, respectively [25, 27]. The difficulties of studying such a low rate process is somewhat compensated by the very distinct signatures (a peak from a flat and low background at 4-5 MeV). The EMC experiment [59] observed a surprisingly large axial isoscalar versus isovector couplings (~ 0.15). This would enhance the $\bar{\nu}_e$-^{11}B NC cross-sections by 30-40%. Accordingly, a measurement better than this uncertain will give independent and complementary information on the axial isoscalar couplings and therefore the strange quark content of the nucleon through the contribution of the $\bar{\psi}_{\rm s}\gamma_\mu\gamma_5\psi_{\rm s}$ term.

6 Collaboration Organization

One of the important motivations of performing the CsI experiment is to acquire the experience of conceiving, formulating, and then constructing and executing a complex modern high-energy-physics style experiment in its totality. The successful design, construction and operation of the CsI experiment requires the efficient coordination and the coherent involvement of expertise from many diversified fields: particle physics, nuclear physics, nuclear engineering, low background techniques, mechanical engineering design, modern electronics design, data acquisition systems, modern software packages and large-scale computation in simulations and analysis. In addition, efficient communications and working experience with certain key industrial manufacturers have to be established.

Protocols for the operation of international collaborations are adopted for our Collaboration. Collaboration meetings are held once every three months, the venues alternating between Taiwan and mainland China, to review the progress status, to identify areas of focus and to define the next immediate goals. Regional co-ordination are under the responsibilities of Academia Sinica (for Taiwan groups), Institute of High Energy Physics, Beijing (for mainland Chinese groups), and University of Maryland (for U.S. participation). Administrative and financial issues are discussed among the "Collaboration Board" made up of one representative per institute. Topical working group meeting are arranged ad hoc accordingly to demand. In addition, phone and video meetings via the Internet[19] take place between Taiwan, Beijing and the U.S. regularly.

The regional co-ordinators follow closely the progress and ensure efficient task distributions among the groups. A internal newsletter is prepared regularly review the status and is broadcast to all members via the Internet. Web-sites are set up both in Taiwan[20] and in the Mainland to centralize and store all relevant information on the experiment, and to ensure their easy access by all members of the Collaboration.

The Taiwan groups are funded by the Taiwan National Science Foundation and by the Academia Sinica operational grant. The Mainland groups are funded by the Mainland National Science Foundation, while University of Maryland are funded by an U.S. National Science Foundation (International Program).

The principal task-sharing among the groups are summarized in Table 17. Up to now, the financial resources come mainly from Taiwan, while most groups contribute significantly in the prototype and design studies, formulation of the physics program and the construction of the experiment.

The estimated budget required for the CsI experiment is rather modest in the typical high energy physics scale. The summary of the major items are listed in Table 18. The estimate does not include travels, personnel and labour expenses (except for the shielding installation) and operational cost. Assuming that a loan arrangement for the heavy water will be realized, we hope to be able perform the experiment with a 1 MUSD budget ceiling.

7 Status and Outlook

By the end of 1998, the conception and formulation of the project is well completed. There are intense efforts throughout the Collaboration in the crystal production and quality control monitor, as well as the design, prototyping and construction of the hard-

[19]based on the VRVS packages

[20]http://hep1.phys.sinica.edu.tw/EXONO/index.html/

ware, electronics and software systems. Our immediate goal is to have the first 100 kg detector equipped with full electronics and data acquisition system and other online control software operational and fully debugged at the AS by Spring 1999, before moving it to the NP2 reactor site. The 40-ton shielding house will first be built in the contractor's base before moving to NP2. By the time the experiment reaches a state of matured data-taking on NP2 site, resources within the Collaboration will be shared between adding more crystals plus electronics channels to the pilot experiment, and launching the bigger longer-term project beyond.

Residual technical details on the experiment to be finalized and optimized include :

- Design of the pre-amplifier.
- Study of longitudinal position resolution in a 40 cm long unit with two crystals glued together and read out by photo-diodes.
- Design of the inner target mechanics, which depends on the previous two items.
- Developing techniques to push the sensitivities of the crystal intrisic purity measurements to better than the current 10^{-12} g/g level, based on pulse shape discrimination.

This technical report will be regularly updated when these and other fronts get to completion.

In the mean time, the Collaboration is also investigating our long-term direction beyond the "pilot" experiment. Opportunities along the directions of long-baseline reactor neutrino oscillations, dark matter searches and solar neutrino studies have been investigated. Our current thoughts and evaluations on the world status and how we can fit in are documented in Ref. [4]. The pilot experiment presented in this report is an important, coherent and indispensible first step towards the realization of these future visions.

In addition to being a pioneering effort on the development of large-scale basic research in Taiwan, the pilot experiment also represents one of the first big collaborative efforts among scientists on both sides of the Taiwan Strait. The importance of the outcomes of such an "experiment" and experience will lie beside, if not beyond, neutrino physics.

References

[1] C.Y. Chang, S.C. Lee and H.T. Wong, in *Procs. of XVI Int. Workshop on Weak Interactions and Neutrinos 1997*, Nucl. Phys. (Procs. Suppl.) **B 66**, 419 (1998).

[2] S.C. Wang et al., preprint AS-TEXONO/98-04, submitted to Nucl. Instrum. Methods (1998).

[3] H.T Wong and J. Li, LANL e-print hep-ex/9805024, to be published in *Procs. of the Workshop on the Japan Hadron Facilities Science* (1998), also in *Procs. of the XVIII Int. Conf. in Neutrino Physics and Astrophysics* (1998).

[4] H.T. Wong (for TEXONO Collaboration), in preparation.

[5] G. Zacek et al. (Gösgen), Phys. Rev. **D 34**, 2621 (1986) ;
A.I. Afonin et al. (Rovno), Sov. Phys. JETP **67** (2), 213 (1988);
G.S. Vidyakin et al. (Krasnoyarsk), JETP Lett. **59**, 364 (1994);
B. Achkar et al. (Bugey), Nucl. Phys. **B 434**, 503 (1995);
Z.D. Greenwood et al. (Savannah River), Phys. Rev. **D 53**, 6054 (1996);
M. Apollonio et al., (Chooz) Phys. Lett. **B 420**, 397 (1998);
F. Boehm et al. (Palo Verde), Palo Verde Proposal (1993).

[6] F. Suekane (KamLAND), in *Procs. of VI Conf. on Intersection of Particle and Nuclear Phys., Big Sky, Montana (1997)* ; also as preprint Tohoku-NSS-97-01 (1997);
S. Schoenert and L. Oberauer (Borexino), Nucl. Phys. (Proc. Suppl.) **B 70**, 195 (1998).

[7] Letter of Intent, Belle Coll., KEK (1993);
Letter of Intent, BaBar Coll., SLAC-443 (1994).

[8] M.L. Sarsa et al., Nucl. Phys. **B 35**, 154 (1994);
N.J.C. Spooner et al., Phys. Lett. **B 321**, 156 (1994);
R. Bernabei et al., Phys. Lett. **B 389**, 757 (1996).

[9] For a recent review, see, for example, "Precision Measurements with High-Energy Neutrino Beams", J.M. Conrad, M.H. Shaevitz and Tim Bolton, LANL e-print hep-ex/9707015, submitted to Rev. Mod. Phys. (1997).

[10] A.V. Kyuldjiev, Nucl. Phys. **B 243**, 387 (1984).

[11] P.Vogel and J.Engel, Phys. Rev. **D 39**, 3378 (1989).

[12] B. Kayser et al., Phys. Rev. **D 20**, 87 (1979).

[13] See, for example, J.N. Bahcall et al. Physics Today July 1996, 30, and references therein (1996).

[14] L. Wolfenstein, Phys. Rev. **D 17**, 2369 (1978);
S.P. Mikheyev and A. Yu. Smirnov, Sov. J. Nucl. Phys. **42**, 1441 (1985).

[15] Savannah River : F. Reines, H.S. Gurr and H.W. Sobel, Phys. Rev. Lett. **37**, 315 (1976).

[16] Kurtchatov : G.S. Vidyakin et al, JETP Lett. **55**, 206 (1992).

[17] Rovno : A.I. Derbin et al., JETP Lett. **57**, 769 (1993).

[18] NUMU : C. Broggini et al., Nucl. Instrum. Methods **A311**, 319 (1992);
ITEP : A.G. Beda et al., LANL e-print hep-ex/9706004v2 (1997).

[19] Savannah River : T.L. Jenkins, F.E. Kinard, and F. Reines, Phys. Rev. **185**, 1599 (1969); E. Pasierb et al., Phys. Rev. Lett. **43**, 96 (1979) .

[20] Deiton : G.S. Vidyakin et al., JETP Lett. **49**, 151 (1988); G.S. Vidyakin et al., JETP Lett. **51**, 279 (1990).

[21] B.R. Davis et al., Phys. Rev. **C 19**, 2259 (1979).

[22] H.C. Lee, Nucl. Phys. **A 294**, 473 (1978) ;
T.W. Donnelly and R.D. Reccei, Phys. Rep. **50**, 1 (1979).

[23] J.N. Bahcall, K. Kubodera, and S. Nozawa, Phys. Rev. **D 38**, 1030 (1988);
S. Ying, W.C. Haxton, and E.M. Henley, Phys. Rev. **D 40**, 3211 (1989).

[24] G.T. Ewan et al. SNO Proposal (1987).

[25] J. Bernabéu et al., Nucl. Phys. **B 378**, 131 (1992);
K. Kubodera and S. Nozawa, Int. J. Mod. Phys. **E 3**, 101 (1994).

[26] D.B. Kaplan and A. Manohar, Nucl. Phys. **B 310**,527 (1988);
G. Garvey et al., Phys. Rev. **C 48**, 1919 (1993).

[27] R.S. Raghavan and S. Pakvasa, Phys. Rev. **D 37**, 849 (1988).

[28] T. Suzuki, Y. Kohyama, and K. Yazaki, Phys. Lett. **B 252**, 323 (1990).

[29] W. Haxton, Phys. Rev. Lett. **60**, 768 (1988);
J. Engel, S. Pittel and P. Vogel, Phys. Rev. Lett. **67**, 426 (1991);
C.C. Chang, C.Y. Chang, and G. Collins, Nucl. Phys. (Proc. Suppl.) **B 35**, 464 (1994).

[30] L.M. Krauss, S.L. Glashow and D.N. Schramm, Nature **310**, 191 (1984).

[31] B. Achkar et al., Bugey Collaboration, Phys. Lett. **B 374**, 243 (1996).

[32] P. Vogel et.al., Phys. Rev. **C 24**, 1543 (1981);
H.V. Klapdor and J. Metzinger, Phys. Rev. Lett. **48**, 127 (1982); Phys. Lett. **B 112**, 22 (1982);
P. Vogel, Phys. Rev. **D 29**, 1918 (1984).

[33] H. Grassman, E. Lorentz, and H.G. Moser, Nucl. Instrum. Methods **228**, 323 (1985);
P. Schotanus, R. Kamermans, and P. Dorenbos, IEEE Trans. Nucl. Sci. **37**, 177 (1990).

[34] D.E. Groom, Nucl. Instrum. Methods **219**, 141 (1984);
S. Gunji et al., Nucl. Instrum. Methods **A 295**, 400 (1990);
M. Suffert, Nucl. Instrum. Methods **A 322**, 523 (1992).

[35] U. Kilgus, R. Kotthaus, and E. Lange, Nucl. Instrum. Methods **A 297**, 425, (1990);
R. Kotthaus, Nucl. Instrum. Methods **A 329**, 433 (1993).

[36] J. Alarja et al., Nucl. Instrum. Methods **A 242**, 352 (1986);
P. Kreutz et al., Nucl. Instrum. Methods **A 260**, 120 (1987).

[37] G. Alimonti et al., Nucl. Instrum. Methods **A 406**, 411 (1998).

[38] "MCNP - A General Monte Carlo N-particle Transport Code, Version 4A", J. F. Briesmeister ed., LA-12625-M (1993).

[39] A. Da Silva et al., Nucl. Instrum. Methods **A 354**, 553 (1995).

[40] P. Vojtyla, Nucl. Instrum. Methods **B 100**, 87 (1995).

[41] G. Heusser, Nucl. Instrum. Methods **B 58**, 79 (1991);
P. Jagam and J.J. Simpson, Nucl. Instrum. Methods **A 324**, 389 (1993).

[42] S. Charalambus, Nucl. Phys. **A 166**, 145 (1971);
T. Suzuki, D.F. Measday, and J.P. Roalsvig, Phys. Rev. **C 35**, 2212 (1987);
T. Kozlowski et al., Nucl. Phys. **A 436**, 717 (1985).

[43] V.L. Alexeev et al., Nucl. Phys. **A248**, 249 (1975);
L.A. Schaller, J. Kern and B. Michaud, Nucl. Phys. **A 165**, 415 (1971).

[44] A. Balysh et al., Phys. Lett. **B 322**, 176 (1994).

[45] F. Bergsma et al., CHARM Coll., Phys. Lett. **B 147**, 481 (1984);
P. Vilain et al., CHARM-II Coll., Phys. Lett. **B 335**, 246 (1994).

[46] R.C. Allen et al., Phys. Rev. Lett. **55**, 2401 (1985);
R.C. Allen et al., Phys. Rev. **D 47**, 11 (1993).

[47] B.W. Lee and R.E. Shrock, Phys. Rev. **D 16**, 1444 (1977);
W. Marciano and A.I. Sanda, Phys. Lett. **B 67**, 303 (1977).

[48] M.A.B. Beg, W.J. Marciano and M. Ruderman, Phys. Rev. **D 17**, 1395 (1977);
M. Fukugita and T. Yanagita, Phys. Rev. Lett. **58**, 1807 (1987);
K.S. Babu and R.N. Mohapatra, Phys. Rev. Lett. **63**, 228 (1989);
M. Leurer et al., Phys. Lett. **B 231**, 81 (1990);
R. Barbieri et al., Phys. Lett. **B 252**, 251 (1990);
A.M. Barr, E.M. Friere and A. Zee, Phys. Rev. Lett. **65**, 2626 (1990);
B.K. Pal, Phys. Rev. **D 44**, 2261 (1991).

[49] J.M. Lattimer and J. Cooperstein, Phys. Rev. Lett. **61**, 23 (1988);
R. Barbieri and R.N. Mohapatra, Phys. Rev. Lett. **61** 27 (1988);
D. Notzold, Phys. Rev. **D 38**, 1658 (1988).

[50] J. Bernstein et al., Phys. Rev. **132**, 1277 (1963);
P. Sutherland et al., Phys. Rev. **D 12**, 2700 (1976);
G. Raffelt, Phys. Rev. Lett. **64**, 2856 (1990).

[51] J. Morgan, Phys. Lett. **B 102**, 247 (1981);
M. Fukugita and S. Yazaki, Phys. Rev. **D 37**, 3817 (1987).

[52] M.B. Voloshin, M.I. Vysotskii and L.B. Okun, Sov. Phys. JETP **64**, 446 (1986).

[53] B.W. Filippone and P. Vogel, Phys. Lett. **B 246**, 546 (1990);
J.W. Bieber et al., Nature **348**, 407 (1990);
L. Krauss, Nature **348**, 403 (1990);
J.N. Bahcall and W.H. Press, Astrophys. J. **370**, 730 (1991).

[54] R. Davis Jr., Nucl. Phys. (Procs. Suppl.) **B 48**, 284 (1996).

[55] G. Walther, Preprint astro-ph/9710031 (1997).

[56] Y. Suzuki, in *Procs. of Neutrino '96 Conference*, 73, World Scientific (1997).

[57] F. Reines, H.W. Sobel, and E. Pasierb, Phys. Rev. Lett. **45**, 1307 (1980).

[58] F. Reines, Nucl. Phys. **A396**, 469c (1983).

[59] J. Ashman et al., EMC Coll., Phys. Lett. **B 206**, 364 (1988);
J. Ashman et al., EMC Coll., Nucl. Phys. **B 328**, 1 (1989).

Experiment	Neutron Capture Isotopes	Target Mass	Distance from Core (max.)	Δm^2 (90% CL) (min.)	Status
Gösgen	^{3}He	320 kg	65 m	0.019	completed 1986
Rovno	Gd	190 kg	25 m	0.05	completed 1988
Krasnoyarsk†	^{3}He	458 kg	231 m	0.008	completed 1994
Bugey	^{6}Li	555 kg	95 m	0.01	completed 1995
Savannah River	Gd	250 kg	24 m	0.1	completed 1996
Chooz	Gd	5 ton	1 km	0.9×10^{-3}	completed 1998
Palo Verde	Gd	12 ton	750 m	$10^{-3\ddagger}$	data taking
Borexino	proton	300 ton	1000 km	$2 \times 10^{-6\ddagger}$	start 2001
KamLAND	proton	1000 ton	160 km	$10^{-5\ddagger}$	start 2001

† All experiments except the Krasnoyarsk detector adopted liquid scintillator as a proton-rich active target. The Krasnoyarsk experiment used polyethylene as passive target.
‡ Goals

Table 1: A summary of previous and current reactor neutrino oscillation experiments as well as future projects.

Plant	Type	No. Cores	Power/core (GW)	Location	Status
I	Boiling Water	2	1.78	Northern Shore	Operational
II	Boiling Water	2	2.90	Northern Shore	Operational
III	Pressurized Water	2	2.78	Southern Shore	Operational
IV	Advanced Boiling Water	2	4.1	Northern Shore	Compl. 2004

Table 2: Power Reactor Plants in Taiwan and their Parameters. The Pilot Experiment will be performed at a distance of 30 m from the core in Nuclear Power Plant II.

Properties	CsI(Tl)	NaI(Tl)	BGO	Liquid	Plastic	Glass
Density	4.51	3.67	7.13	0.9	1.0	2.5
Relative Light Yield	0.45	1.00	0.15	0.4	0.35	0.15
Radiation Length (cm)	1.85	2.59	1.12	$\sim$45	$\sim$45	4
Emission Peak (nm)	565	410	480	425	425	395
Decay Time (ns)	1000	230	300	2	2	100
Refractive index	1.80	1.85	2.15	1.5	1.6	1.55
Hygroscopic	slightly	yes	no	no	no	no

Table 3: Characteristic properties of the common crystal scintillators and their comparison with typical liquid, plastic and glass scintillators.

Parameters	Values
Active Area	10 mm $\times$ 20 mm
Thickness	300 μm
Spectral Range	320 nm to 1100 nm
Quantum Efficiency at 550 nm (CsI(Tl) peak)	85%
Reverse Voltage Max. Reverse Voltage Typical (V_R)	100 V 70 V
Dark Current at (V_R)	3 nA
Terminal Capacitance at (V_R)	85 pF
Operating Temperature	-20°C to 60°C
Dark Current at 25°C Dark Current at 0°C	0.8 nA 0.1 nA

Table 4: Characteristics of the candidate photo-diode.

Parent	Daughter	Half-life	Decay Mode	Q Value (MeV)
^{238}U	^{234}Th	4.47×10^9 y	α	4.270
^{234}Th	^{234}Pa*	24.10 d	β^-	0.183
^{234}Pa*	^{234}Pa	1.18 min	IT (0.13%)	0.08
^{234}Pa*	^{234}U	1.18 min	β^- (99.87%)	2.207
^{234}Pa	^{234}U	6.70 h	β^-	2.287
^{234}U	^{230}Th	2.45×10^5 y	α	4.856
^{230}Th	^{226}Ra	8.0×10^4 y	α	4.771
^{226}Ra	^{222}Rn	1600 y	α	4.871
^{222}Rn	^{218}Po	3.83 d	α	5.591
^{218}Po	^{214}Pb	3.05 min	α	6.115
^{214}Pb	^{214}Bi	26.8 min	β^-	1.024
^{214}Bi	^{214}Po	19.7 min	β^-	3.270
^{214}Po	^{210}Pb	163.7 μs	α	7.834
^{210}Pb	^{210}Bi	22.26 y	β^-	0.063
^{210}Bi	^{210}Po	5.01 d	β^-	1.161
^{210}Po	^{206}Pb	138.38 d	α	5.408

Table 5: The ^{238}U decay chain, with the low part of the table showing decays from the daughters of ^{222}Rn.

Parent	Daughter	Half-life	Decay Mode	Q Value (MeV)
^{232}Th	^{228}Ra	1.41×10^{10} y	α	4.081
^{228}Ra	^{228}Ac	5.76 y	β^-	0.046
^{228}Ac	^{228}Th	6.13 hr	β^-	2.137
^{228}Th	^{224}Ra	1.91 y	α	5.520
^{224}Ra	^{220}Rn	3.66 d	α	5.789
^{220}Rn	^{216}Po	55.6 s	α	6.405
^{216}Po	^{212}Pb	0.15 s	α	6.907
^{212}Pb	^{212}Bi	10.64 h	β^-	0.573
^{212}Bi	^{212}Po	60.60 min	β^- (64.0%)	2.246
^{212}Bi	^{208}Tl	60.60 min	α (36.0%)	6.207
^{212}Po	^{208}Pb	0.30 μs	α	8.954
^{208}Tl	^{208}Pb	3.05 min	β^-	2.377

Table 6: The ^{232}Th decay chain, with the low part of the table showing decays from the daughters of ^{220}Rn.

Parameters	**Values**
Individual Crystal Module :	
Dimension	hexagonal-shaped with 2 cm side and 10 cm length
Mass	0.94 kg
Unit :	
Configuration	2 crystals coupled together
Active Target Configuration :	
Crystal Matrix	2(Width)$\times$17(Depth)$\times$15(Height)
Dimesion	40 cm(W)$\times$60 cm(D)$\times$46 cm (H)
Total No. of Crystal Modules	510
Total Mass	480 kg
Active Target Mass :	
Veto : NO	480 kg
Veto : 1 layer + 3 cm end	312 kg
Veto : 2 layer + 3 cm end	229 kg
Veto : 1 layer + 6 cm end	257 kg
Veto : 2 layer + 6 cm end	200 kg

Table 7: Geometrical parameters of the CsI(Tl) modules and complete detector in the active target configuration.

Data	Size (byte)
Event Header	
Date and Time (year to second)	6
Time in μs (+ overflow)	4 (+2)
Trigger Type	1
Input Parameters	8
No. of Channels with hits	2
Misc. Data	
TDCs	8
Scalers	8
Hit-Pattern	8
Blank and Spare	32
FADC Data	
Channel Number	2
FADC Data	1 $\times$ time-bin (50)
($\times$ N hits)	

Table 8: The format and size of data to be saved on disk.

Standard Shielding Configuration :

Initial Energy	**Capture Probability**					
	External	Veto	Lead	PE+B	Cu	CsI
Exterior Shooting In:						
0.1 MeV	0.54	0.07	0.063	0.33	0.	0.
1 MeV	0.44	0.027	0.033	0.50	0.	0.
10 MeV	0.41	0.027	0.027	0.52	0.0057	0.0066
Middle of Lead and Isotropic:						
0.1 MeV	0.40	0.053	0.058	0.49	0.	0.
1 MeV	0.45	0.027	0.034	0.49	0.	0.
10 MeV	0.47	0.025	0.023	0.48	0.0016	0.0019
Uniform within Crystal and Isotropic:						
0.1 MeV	0.	0.	0.	0.38	0.12	0.50
1 MeV	0.	0.	0.	0.65	0.11	0.24
10 MeV	0.0062	0.0008	0.0007	0.69	0.12	0.19

Table 9: Results of neutron transport simulations with the standard shielding configurations, indicating the neutron capture probabilities among the various materials.

Isotopes	$\tau_{\frac{1}{2}}$	$\mathbf{Q}_\beta$ (MeV)	$\mathbf{BR}_1^\dagger$	$\mathbf{BR}_2^\ddagger$	Time Tags
^{238}U **Series (Table 5) :**					
^{234}Pa	1.17 min	2.29	0.98	0.99	None
^{214}Pb	26.8 min	1.04	0.06	0.98	None
^{214}Bi	19.9 min	3.28	0.19	0.19	$\beta - \alpha$ ($\tau_{\frac{1}{2}} = 164$ μs)
^{210}Bi	5 day	1.16	1.00	1.00	None
^{232}Th **Series (Table 6) :**					
^{228}Ac	6.13 h	2.15	0.0	0.24	None
^{212}Bi	60 min	2.24	0.64×0.54	0.64×0.54	$\beta - \alpha$ ($\tau_{\frac{1}{2}} = 0.3$ μs)

† Branching Ratio to the ground state of the daughter isotopes.

‡ Branching Ratio to the ground state of the daughter isotopes *and* their excited states of less than 500 keV.

Table 10: A list of β-decays with $Q_\beta > 1$ MeV and without associated γ-rays in the ^{238}U and ^{232}Th chains.

Energy Range	1-1.5 MeV	1.5-3 MeV	3-6 MeV
NaI Measurement (Hz)	2500	50	0.12
Per Day		$\times$ 86400	
Scaling by Surface Area[†]		$\times$ 20	
Shielding Attenuation (total)	10^{-6}	4×10^{-5}	1.5×10^{-4}
Threshold > 1 MeV	0.1	0.3	0.6
Active Veto (2 layers)	0.06	0.1	0.1
Single Hit	0.4	0.3	0.15
Estimated Rate per Day	10	31	0.3

[†] For 500 kg of CsI(Tl) target.

Table 11: Estimations of event rates due to ambient radioactivity based on measured background on-site and the standard shielding configuration.

Samples (weight)	**Range of Activity in Bq/kg (in μg/g)**		
	K†	^{232}Th	^{238}U
CsI (127 g)	<0.08 (2.8)	<0.08 (0.024)	<0.08 (0.0064)
B_4C Powder			
NTHU (100 g)	<0.1 (3.5)	<0.1 (0.03)	<0.1 (0.008)
Beijing (74 g)	<0.14 (5)	3.±0.7 (0.9)	<0.14 (0.01)
INER (137 g)	<0.07 (2.5)	<0.07 (0.022)	0.43±0.3
Supplier (78 g)	<0.13 (4.5)	<0.13 (0.04)	1.2±0.4
B_2O_3 powder			
AS sample (96 g)	<0.1 (3.5)	<0.1 (0.03)	<0.1 (0.008)
Photo-diode			
Ham. S2744-08 (20 g)	<0.5 (17.5)	7.1 (2.13)	32.4 (2.6)
Ham. S2744-08 SPL			
Epoxy Resin (33 g)	<0.3 (10.5)	<0.3 (0.09)	<0.3 (0.024)
Copper strips (23 g)	<0.43 (15)	<0.43 (0.13)	<0.43 (0.034)
LEDs (10 g)	<1 (35)	<1 (0.3)	<1 (0.08)
PMT (1)	424 (15000)	2.3(0.6)	2.5 (0.2)
Fiber Glass Circuit Board			
I (100 g)	<0.1 (3.5)	20 (6)	12 (1)
II (100 g)	<0.1 (3.5)	6 (2)	7.3 (0.58)
III (67 g)	<0.15 (5.2)	49±4.7	26.5±7.6
"Bread Board" (144 g)	<0.07 (2.4)	<0.07 (0.02)	<0.07 (0.006)
Flat Cable (208 g)	<0.05 (1.7)	1.2±0.2 (0.32)	0.6±0.2 (0.04)
LEMO Cable (133 g)	<0.07 (2.5)	<0.07 (0.022)	<0.07 (0.006)
Teflon Coated Cable			
Single Wire (143 g)	<0.07 (2.5)	<0.07 (0.02)	<0.07 (0.006)
Coaxial (173 g)	<0.05 (2.0)	<0.05 (0.017)	0.3±0.2
Capacitor (40 g)	<0.25	10±1.3	23±1.0
IC Chips (65 g)	<0.15 (5.3)	<0.15 (0.046)	<0.15 (0.012)
Teflon wrapping sheet			
I (71 g)	<0.14 (4.9)	<0.14 (0.04)	<0.2 (0.008)
II (103 g)	<0.1 (3.5)	<0.1 (0.03)	0.8±0.4 (0.024)
Al. foil (18 g)	<0.56 (19)	<0.56 (0.16)	<0.56 (0.04)
Al. mylar (15 g)	<0.67 (23)	<0.67 (0.2)	<0.67 (0.05)
Al. wrapping sheet (74 g)	<0.14 (5)	3.8 (1.14)	2.6±0.5 (0.2)
Lead raw sample (360 g)	<0.036 (1.3)	<0.036 (0.01)	<0.036 (0.003)

† K is total potassium, multiply by 0.0117% for ^{40}K.

Table 12: A summary of results on the radioactive contaminants in various candidate components based on measurements with low background germanium detectors.

Experiment	Savannah[15]	Kurtchatov[16]	Rovno[17]	NUMU[18]	TEXONO
Target	plastic scin.	fluorocarbon scin.	Si(Li)	CF_4 gas 5 bar	CsI(Tl) crystals
Active Veto	20 cm NaI	none	none	50 cm liq. scin.	3.5 cm CsI(Tl)
Fid. mass	15.9 kg	103 kg	37.5 kg	21 kg	312 kg*
Electron/Mass Ratio	1.0	0.85	0.88	0.84	0.73
Target Electron Ratio	1.0	5.5	2.0	1.1	14.3
$\phi(\bar{\nu}_{\rm e})/10^{12}$ cm^{-2}s^{-1}	22	2.7	20	10	5.6
Rel. Stat. Merits	1.0	0.7	1.8	0.5	3.6
Modularity	per kg	per 15 kg	per 60 g	few mm	per 0.94 kg
Threshold (MeV)	1.5	3.1	0.6	0.5 (goal)	1.0 (goal)
Signal Events / Day	7.1	not quoted	41	10 (expect)	37 (expect)
Signal : Background	0.18	0.1	0.008	2 (goal)	0.45 †
Accuracy of $\sigma(\bar{\nu}_{\rm e}{\rm e})$	29%	53%	49%	not quoted	15% (goal)
μ_ν (10^{-10} $\mu_{\rm B}$)	2-4 ‡	$<$ 2.4	$<$ 1.9	0.3 (goal)	0.8 (goal)

* Based on a 500 kg target with 1 veto layer and 3 cm buffer, as shown in Table 7.

† Background is estimated by scaling with surface area from the Savannah River background level.

‡ Reanalysis of Savannah River experiment [11] indicates excess of events which can be interpreted as finite μ_ν.

Table 13: Characteristics of the previous and current $\bar{\nu}_e$-e scattering experiments.

Electron Energy	$1.5 - 3$ MeV	$3 - 4.5$ MeV
Theory $\sigma(\bar{\nu}_{\rm e}{\rm e})/\sigma_{\rm V-A}$ **[12] :**		
Destructive	0.83	1.20
Constructive	2.2	2.8
No Interference	1.5	2.0
Experiment :		
Savannah River $\sigma(\bar{\nu}_{\rm e}{\rm e})/\sigma_{\rm V-A}$ [15]	0.87 ± 0.25	1.7 ± 0.44
Re-Analysis $\sigma(\bar{\nu}_{\rm e}{\rm e})/\sigma_{\rm SM}$ [11]	1.35 ± 0.4	2.0 ± 0.5
Rovno $\sigma(\bar{\nu}_{\rm e}{\rm e})/\sigma_{\rm SM}$ [17]	1.28 ± 0.63 (0.6-2 MeV)	

Table 14: Theoretical expectations for reactor neutrino $\bar{\nu}_e$-e cross sections from various W-Z interference pattern, normalized to $\sigma_{\rm V-A}$, the cross section for pure charged-current interaction. Experimental measurements are also shown for comparison, together with a re-analysis normalized to $\sigma_{\rm SM}$, the Standard Model value.

Experiment	Savannah[19]	Deiton[20]	TEXONO
Target	268 kg D_2O	406 kg D_2O	500 kg D_2O with Gd
$\phi(\bar{\nu}_e)/10^{12}$ cm^{-2}s^{-1}	25	5	6.4
Rel. Stat. Merits	1.0	0.3	0.48
Detector	^{3}He counter	^{3}He counter	CsI(Tl) scin.
Active Veto	30 cm Liq.Scin.	None	CsI(Tl) scin.
Charged Current Cross-Section :			
Signatures	2 neutrons	2 neutrons	2 511 keV γs and 2 n
Efficiencies	10%	60%	60% (est.)
Signal Events / Day	5±2.8	8.1±2.4	15 (expect)
Signal : Background	0.1	0.16	1 (goal)
$\sigma(\bar{\nu}_e d)_{CC}$ (10^{-45} cm$^2/\bar{\nu}_e$)	1.5±0.4	1.7±0.3	-
Accuracy	27%	18%	5% (goal)
Neutral Current Cross-Section :			
Signatures	1 neutron	1 neutron	1 neutron
Efficiencies	32%	76%	90% (est.)
Signal Events / Day	38±9	22.7±8.0	51 (expect)
Signal : Background	0.1	0.05	0.3 (est.)
$\sigma(\bar{\nu}_e d)_{NC}$ (10^{-45} cm$^2/\bar{\nu}_e$)	3.8±0.9	4.8±1.6	-
Accuracy	24%	33%	10% (goal)

Table 15: Characteristics of the previous $\bar{\nu}_e$-d experiments, and their relative merits compared to the CsI experiment.

Target Nucleus	Excitation Energy (keV)	σ_ν (10^{-45} cm^2)	Events / day †
Ref. [22]:			
^{2}H (D)	2223	7.1	820
^{6}Li	3563	3.4	300
^{7}Li	478	26	2000
^{9}Be	2429	1.2	260
	2780	0.36	77
^{11}B	2110	3.0	660
^{13}C	3684	0.44	77
^{19}F	1554	0.29	32
^{23}Na	439	3.7	160
	2982	0.19	8
^{29}Si	1273	0.36	30
	2426	0.70	59
Ref. [25, 27]:			
^{11}B	2110	3.0	640
	4445	0.32	69
	5021	0.20	46
Ref. [28]:			
^{10}B	3590	0.01	2
	5160	1.3	286

† Events per day at a reactor neutrino flux of 2×10^{13} cm^{-1}s^{-1} with a 1 m^3 target.

Table 16: Predictions on the neutral current excitation cross section and event rates for a selected sample of nuclei.

Institutes	**Tasks and Responsibilities**
AS	Overall coordination, physics, shielding design, electronics design and construction, data acquistion and on-line control systems, simulations, offline software coordination, future projects.
INER	Shielding design and construction, mechanics and workshop facilities, radiopurity measurements (neutron activation), provisions of raw materials (heavy water).
NCTC	Student participation, simulations.
NTU	Student participation, data acquisition.
NTHU	Nuclear engineering, neutron transport calculation, radiopurity measurements (germanium detectors).
NP2	Site provision and logistic support.
CIAE	Physics, background studies, radiopurity measurements (accelerated mass spectroscopy).
IHEP	Physics, CsI production and quality monitor, tests and measurements of prototypes, inner detector engineering design, electronics design and construction, simulations, future projects.
Nanjing	Analysis and simulations.
Shandong	Analysis and simulations.
Hefei	Electronics design and production.
UMD	Provision of plastic scintillators and PMTs, pre-amplifiers, simulations, future projects.

Table 17: Major items in the task sharing among the collaborating institutes. Many groups will participate in the physics and data analysis.

Items	**Amount**	**Unit Price/USD**	**Cost/kUSD**
CsI(Tl) Crystal	500X200 cc	2.5	250
Photo-Diodes	550 pieces	120	66
Electronics Components	600 channels	150	90
DAQ+Computers			70
Power Supplies			30
Cables and Connectors			10
Polyethylene	3 tons		10
OFHC copper	2 ton		15
Lead Shielding	35 tons		40
Shielding Installation			60
Plastic Scintillator			On Loan
Heavy Water			Loan Expected
Total			641
Contingency 20%			128
Seed Funds for R&D			50
Grand Total			819

Table 18: An estimate of the budget for the CsI(Tl) equipment experiment. The figures do not include positions, travels, and labour cost , except the major item on shieldings installation.

$\bar{\nu}_e \; e^- \;\; : \quad$ NC + CC + Interference.

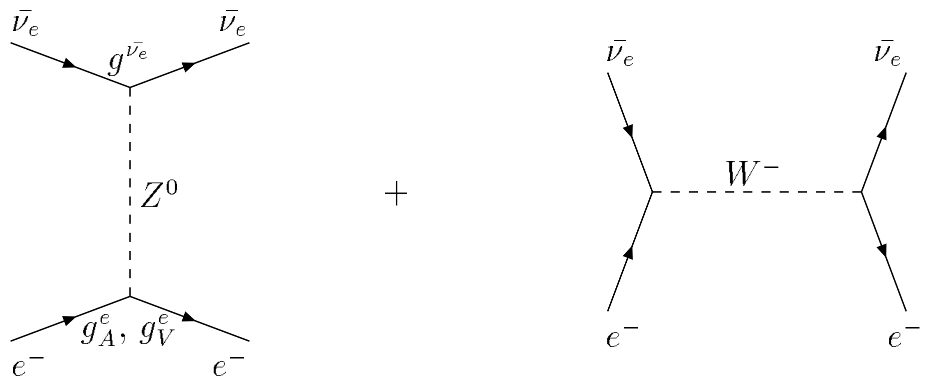

$$g_A^{eff} = g^{\bar{\nu}_e} \cdot g_A^e$$
$$g_V^{eff} = g^{\bar{\nu}_e} \cdot g_V^e$$

Figure 1: Feynman diagrams for ($\bar{\nu}_e$ e) interaction, showing there exists charged and neutral current components, as well as their interference term.

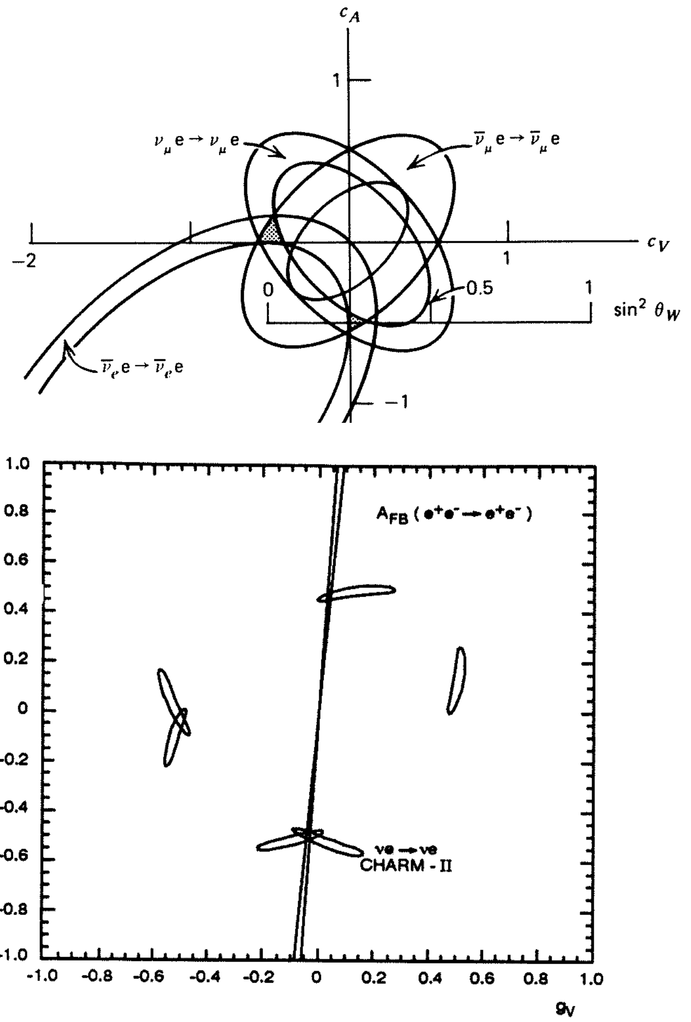

Figure 2: **Top** : Sensitivities of (ν_μ e), ($\bar{\nu_\mu}$ e) and ($\bar{\nu_e}$ e) cross-sections to different regions in the g_A-g_V parameter space (axes labelled c_A and c_V), showing their complementarity. **Bottom** : Allowed region of the g_A-g_V plane from the accelerator (ν e) scattering and the e^+e^- forward-backward symmetry data.

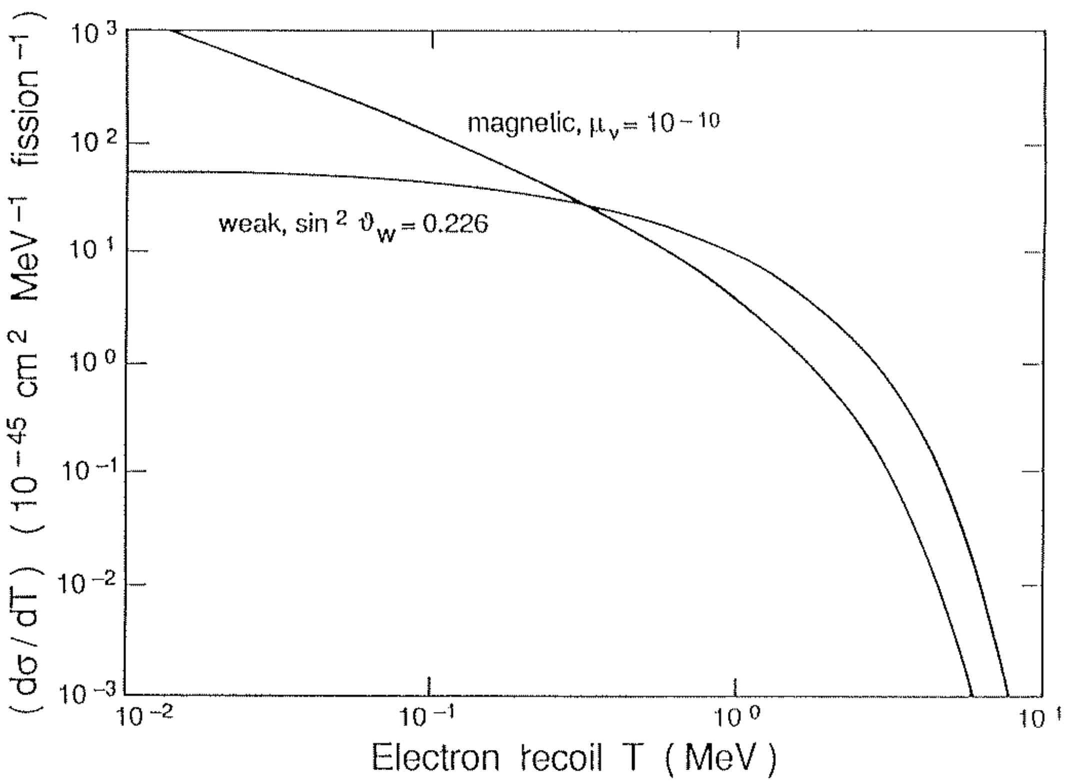

Figure 3: Differential cross section showing the electron recoil energy spectrum in $\bar{\nu}_e$-e scatterings, for of Standard Model processes and for the case with a neutrino magnetic moment of 10^{-10} Bohr magneton, the present experimental limit.

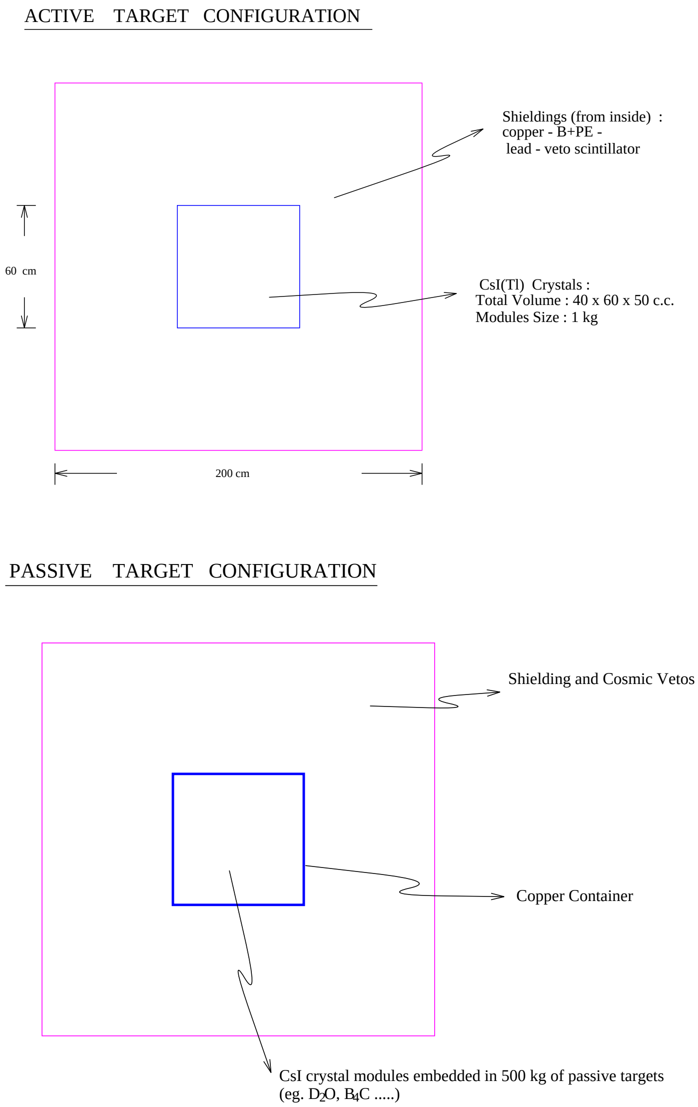

Figure 4: Schematic layout of the experiment using CsI crystals as **Top :** active target, and **Bottom :** where passive target materials like D_2O or B_4C are inserted in between.

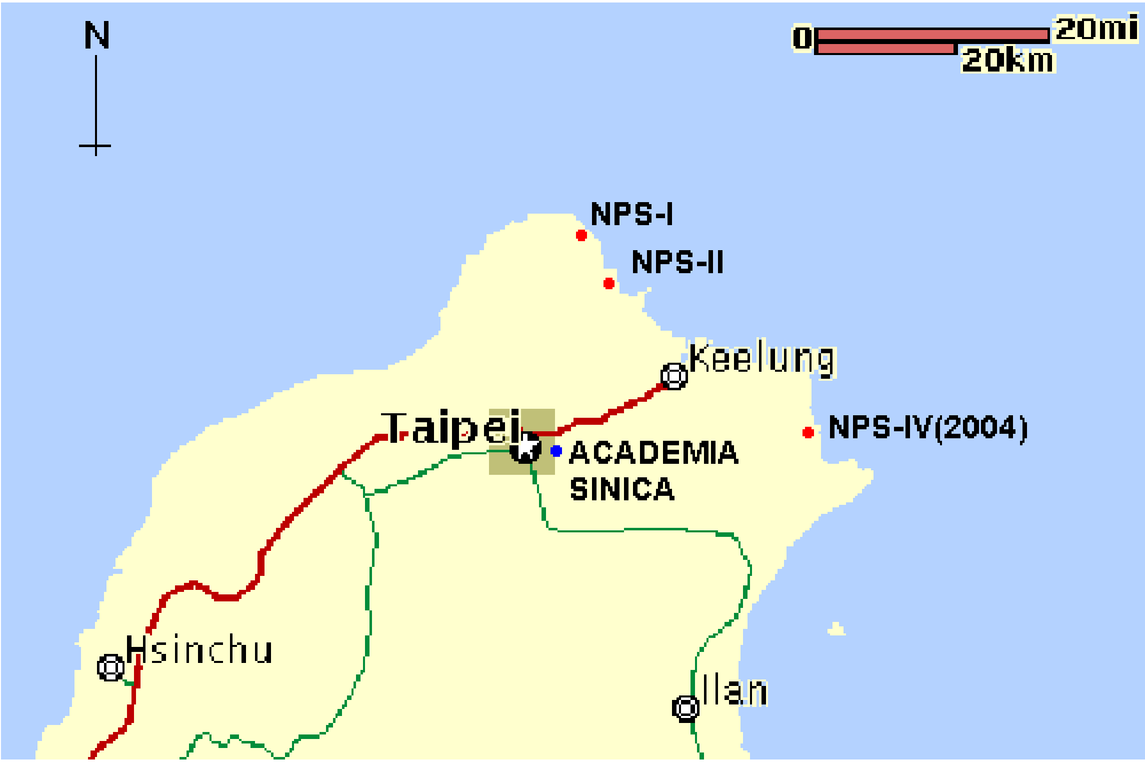

Figure 5: Sketch map of the northern shore of Taiwan, showing the three nuclear power stations and their relative position with Taipei city.

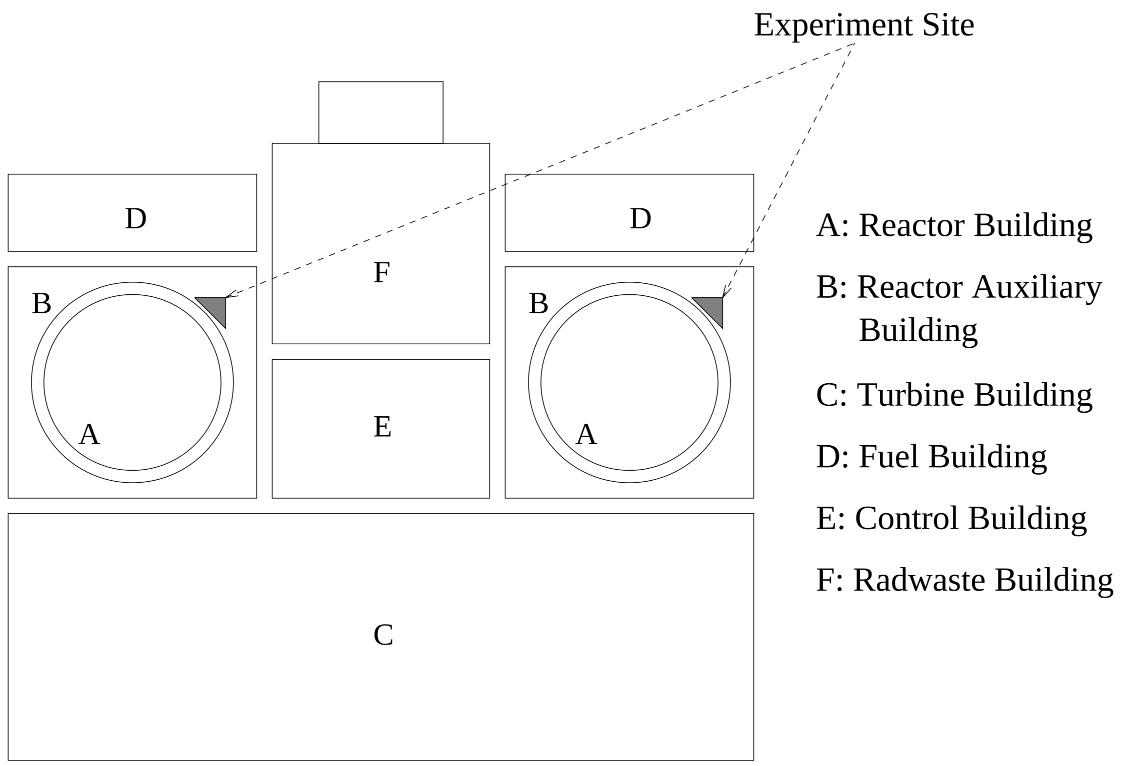

Figure 6: Schematic top view, not drawn to scale, of the NP2 Reactor Complex, indicating the experimental sites.

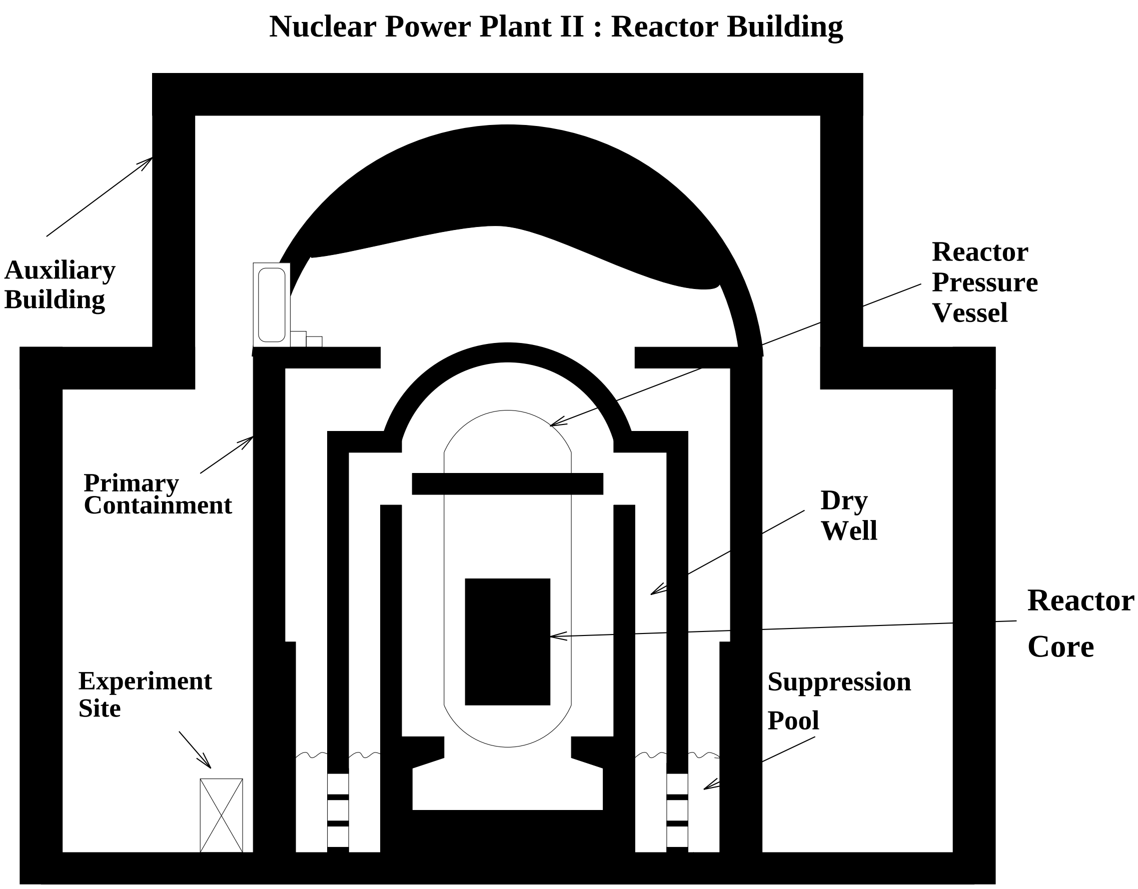

Figure 7: Schematic side view, not drawn to scale, of the NP2 Reactor Building, indicating the experimental site. The reactor core-detector distance is about 30 m.

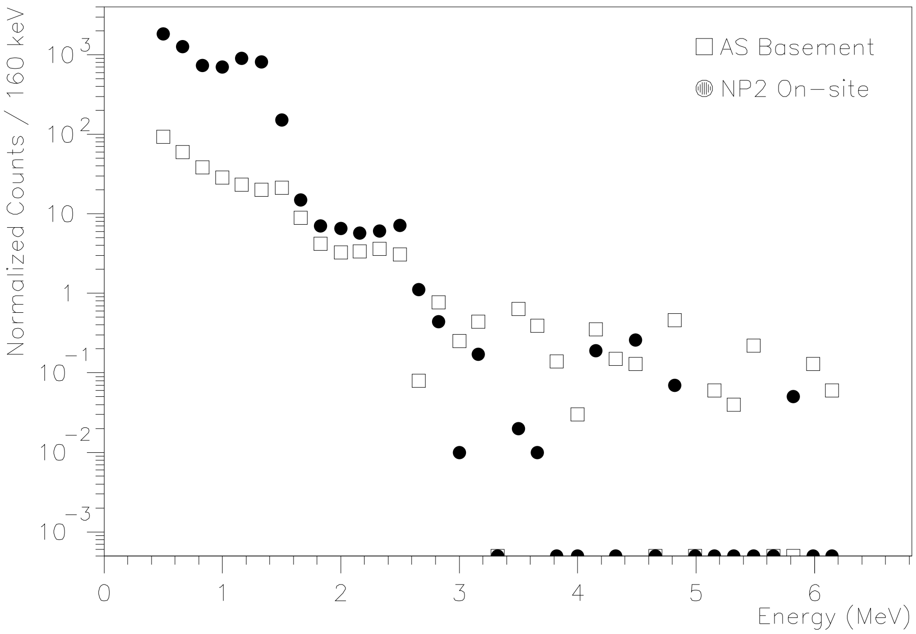

Figure 8: Measured energy spectra on-site at NP2 with a 5-kg NaI(Tl) detector, and in comparison with measurements at AS basement.

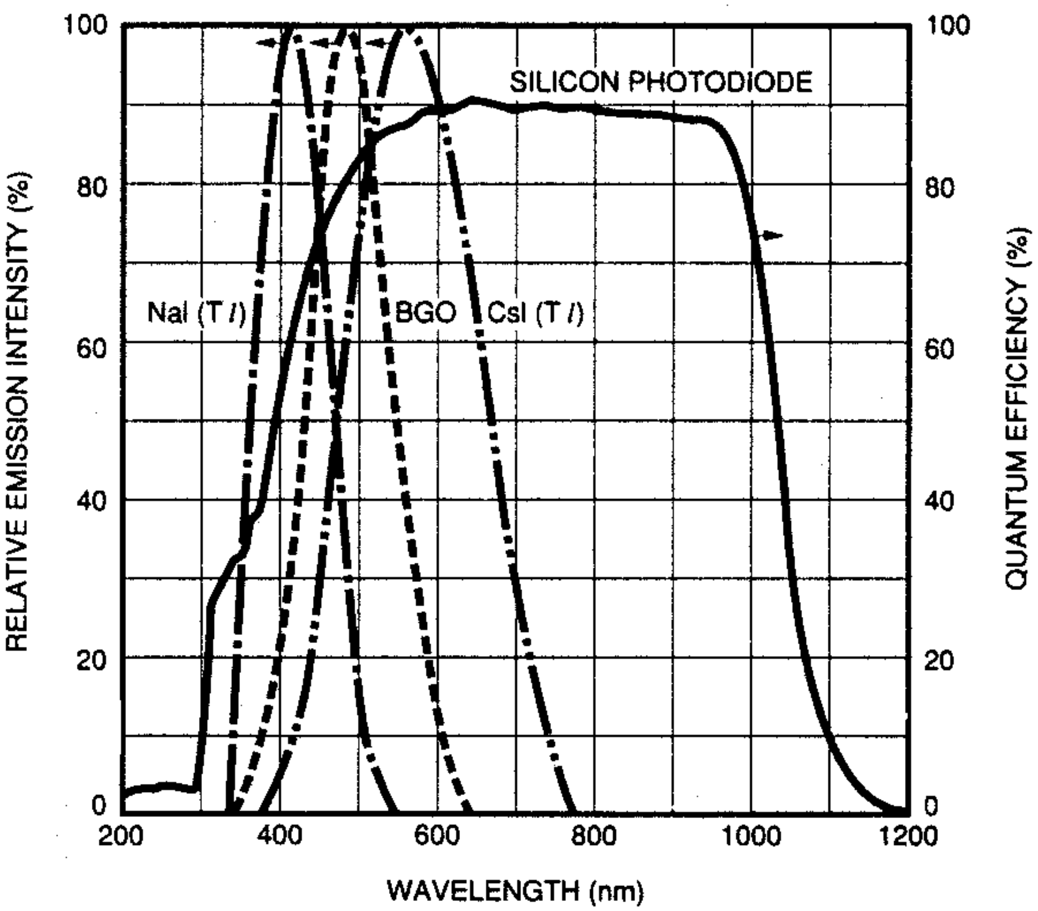

Figure 9: The sensitivities as a function of wavelength for typical silicon photo-diode, and the emission spectra of several common crystal scintillators, showing that CsI(Tl) matches best among them.

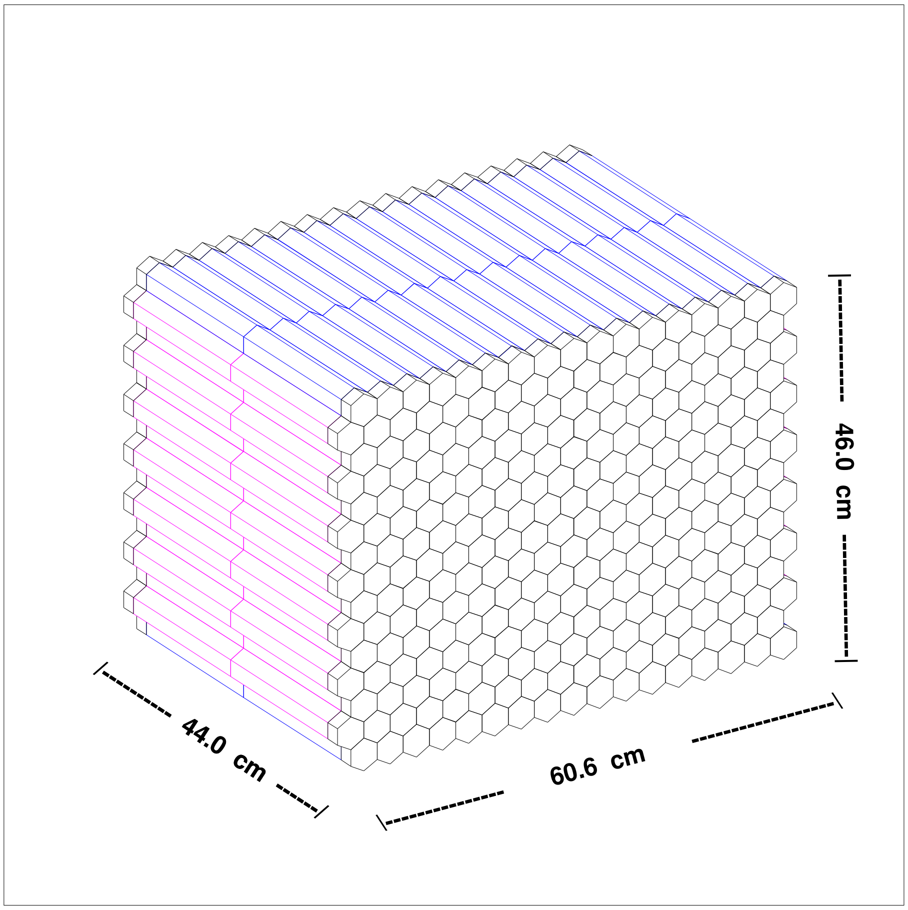

Figure 10: Schematic drawings of the CsI(Tl) target configuration, showing a 2(Width)X 17(Depth)X15(Height) matrix. Individual crystal module is 20 cm long wiht a hexagonal cross-section of 2 cm edge. Readout is performed by photo-diodes and pre-amplifiers at both ends.

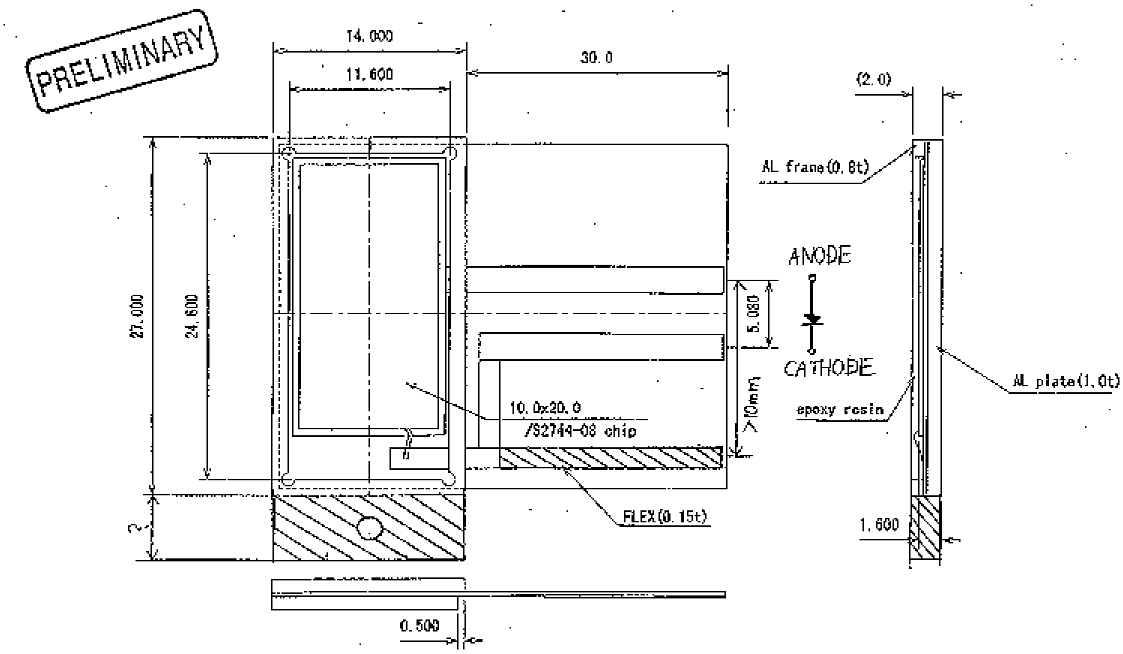

Figure 11: Schematic drawing of the low-background photo-diode custom-designed for this experiment.

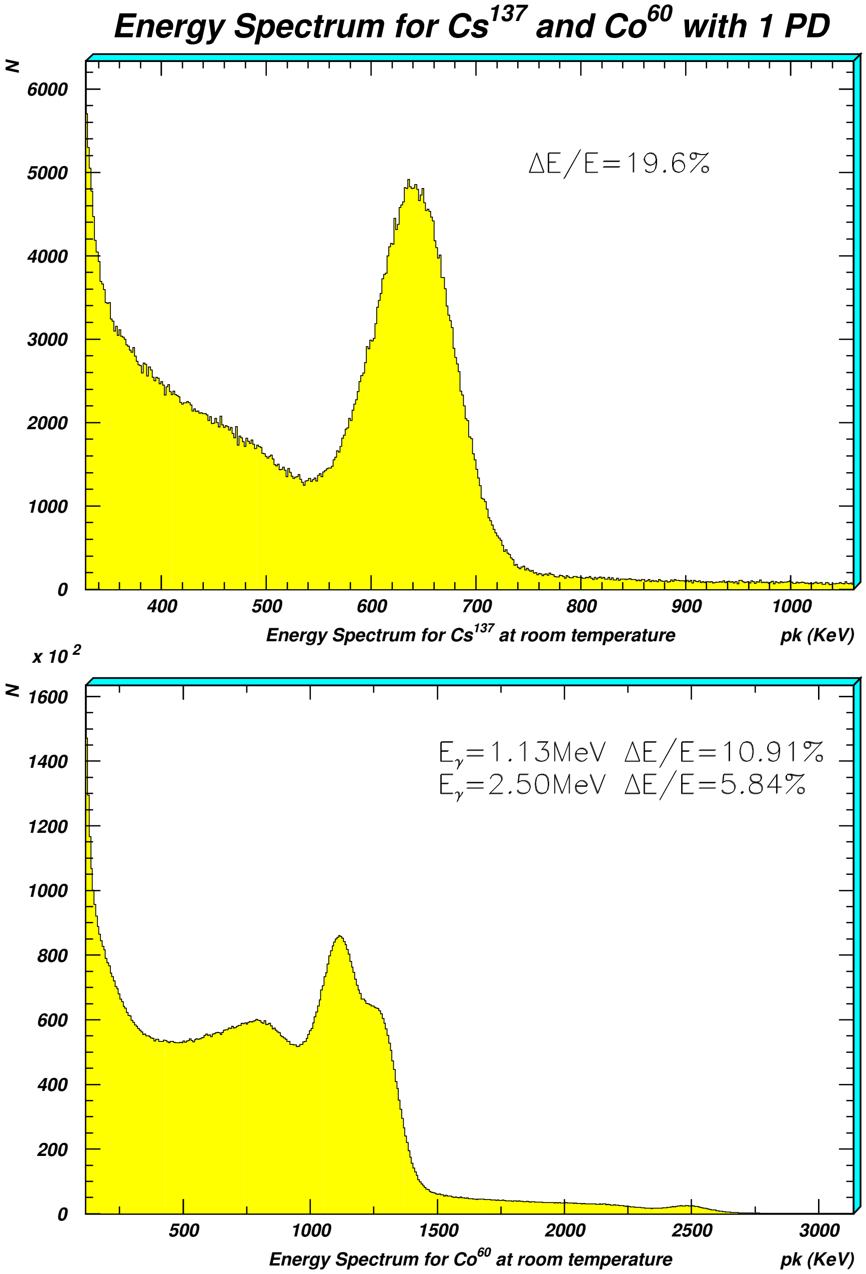

Figure 12: Measured energy resolution from a CsI(Tl) prototype with one photo-diode at room temperature with ^{137}Cs and ^{60}Co sources.

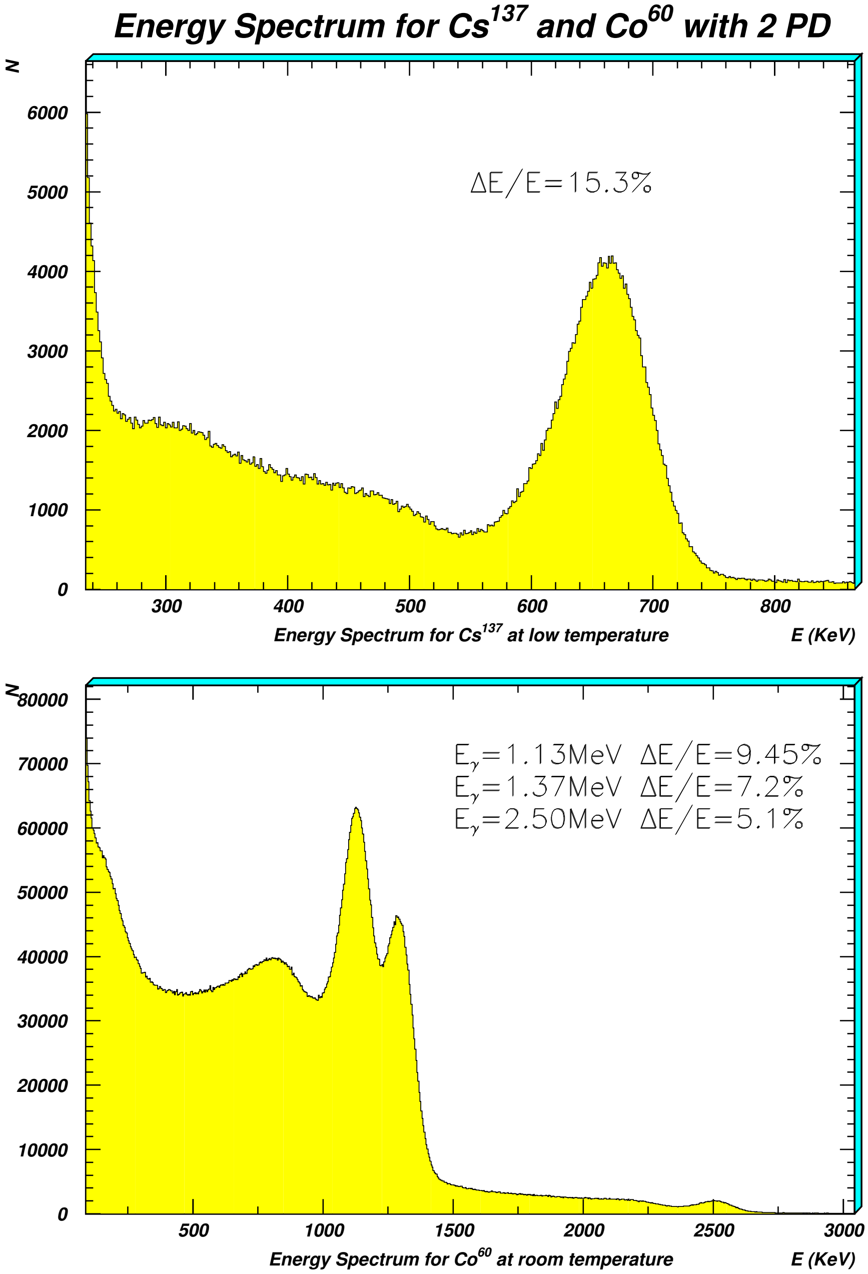

Figure 13: Measured energy resolution from a CsI(Tl) prototype with two photo-diodes with **Top:** ^{137}Cs at 5^o, and **Bottom:** ^{60}Co at room temperature.

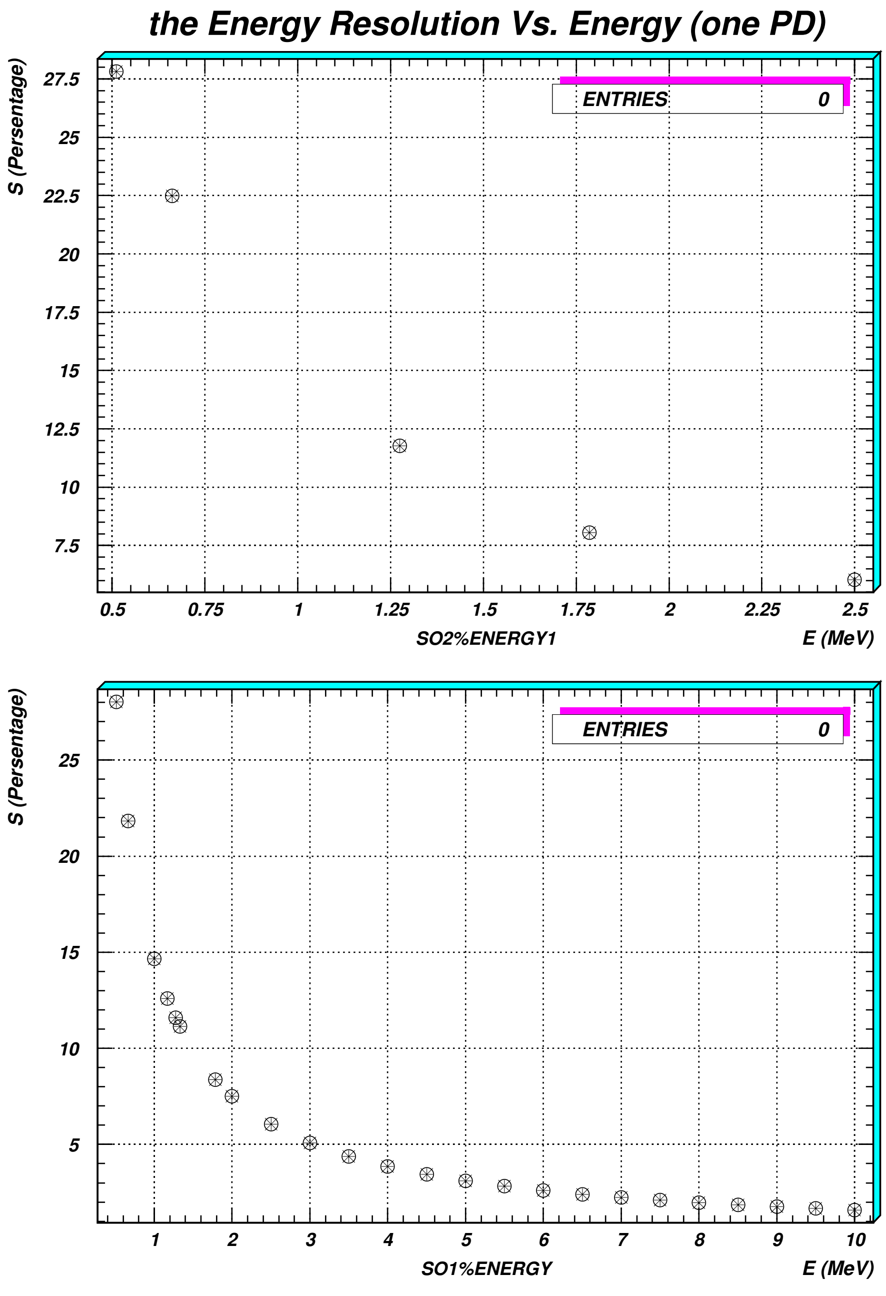

Figure 14: The variation of energy resolution with energy. The appromiate E^{-1} suggests that the resolution is dominated by electronic noise. **Top:** Measurements, and **Bottom:** Extrapolations based on fits.

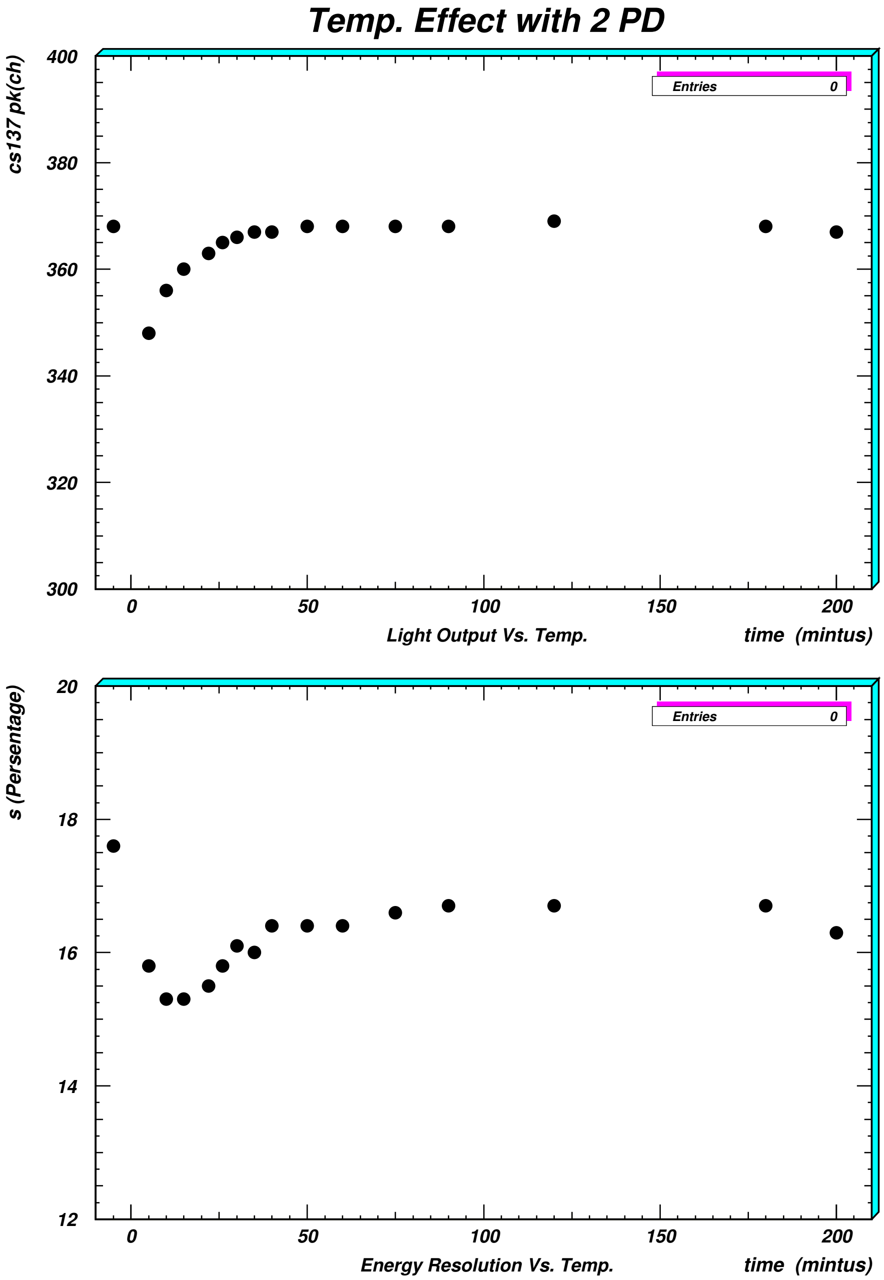

Figure 15: Measured variation of light output and energy resolution with time when the system at -10 °C is warmed to room temperature.

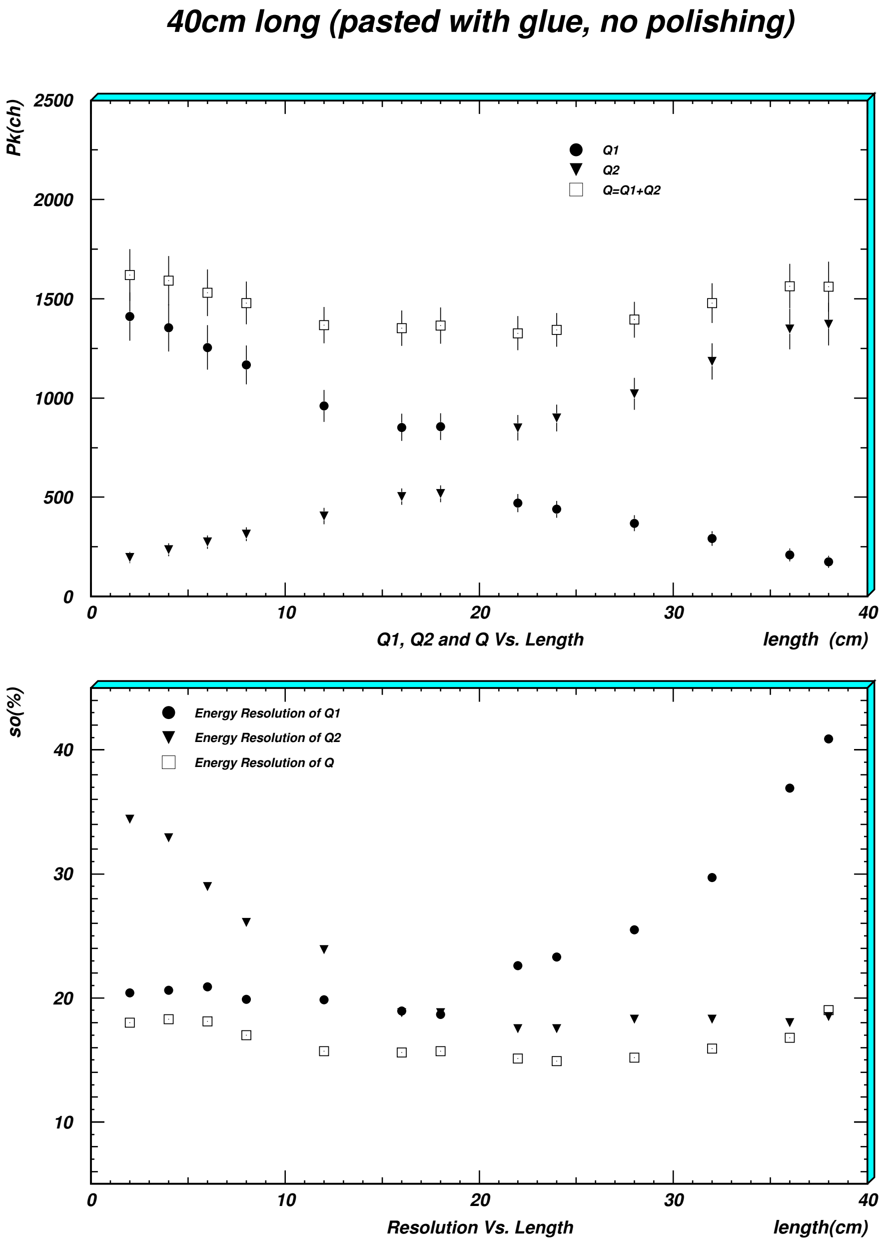

Figure 16: **Top:** The variation of Q_1, Q_2, $Q_1 + Q_2$ (energy), and **Bottom:** the energy measurement accuracy as a function of longitudinal position.

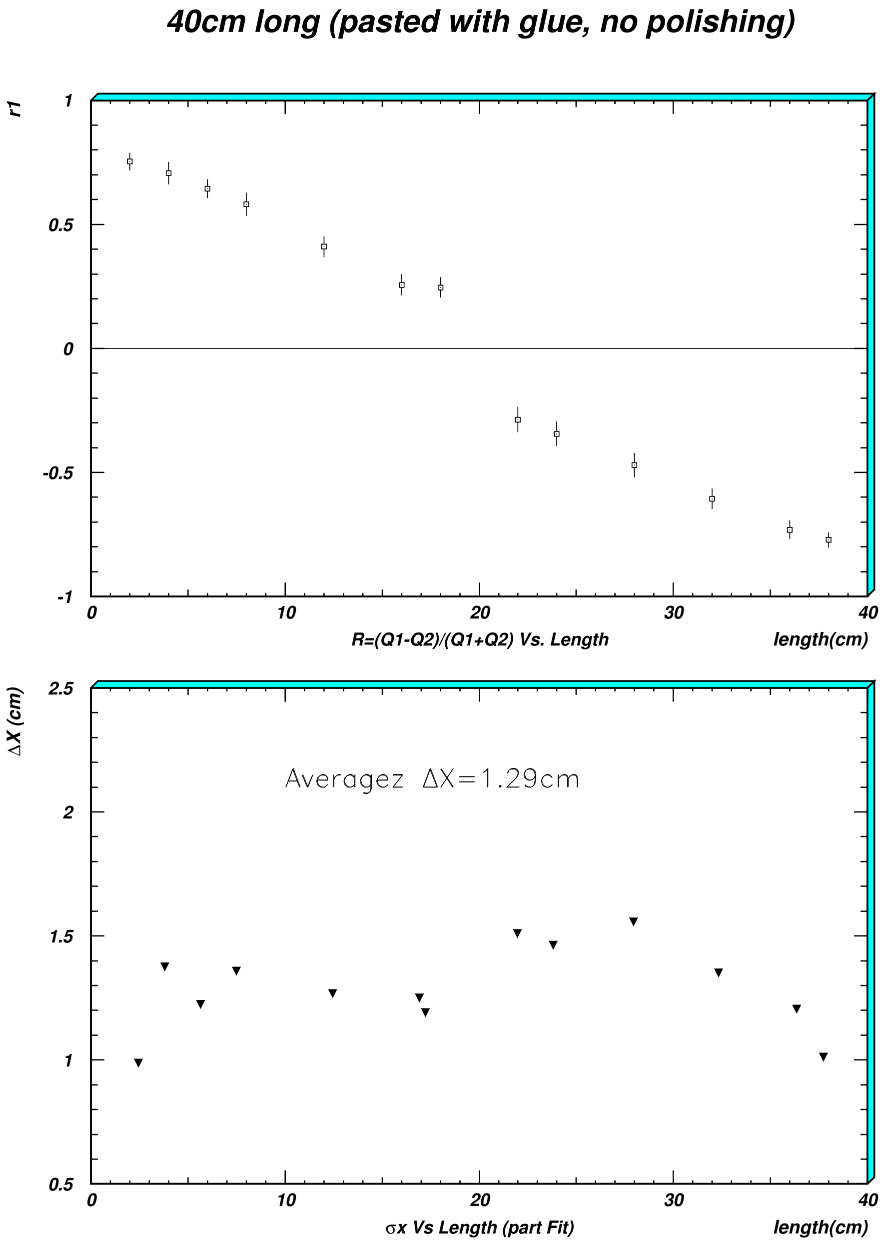

Figure 17: **Top:** The variation of $Q_1 - Q_2$, and **Bottom:** the longitudinal position measurement accuracy, as a function of position.

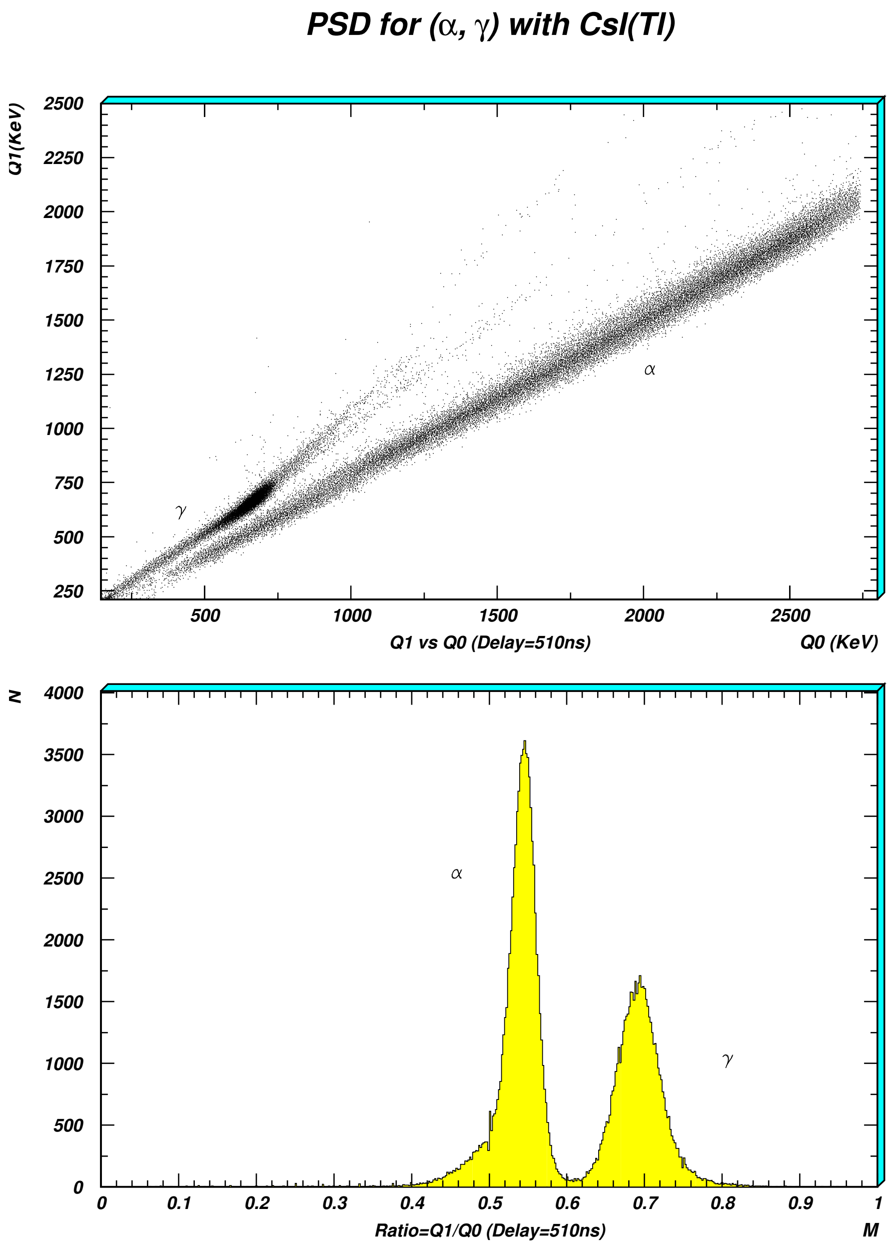

Figure 18: The pulse shape discrimination spectra for α and γ, the separation of which indicates the capabilities of event identification.

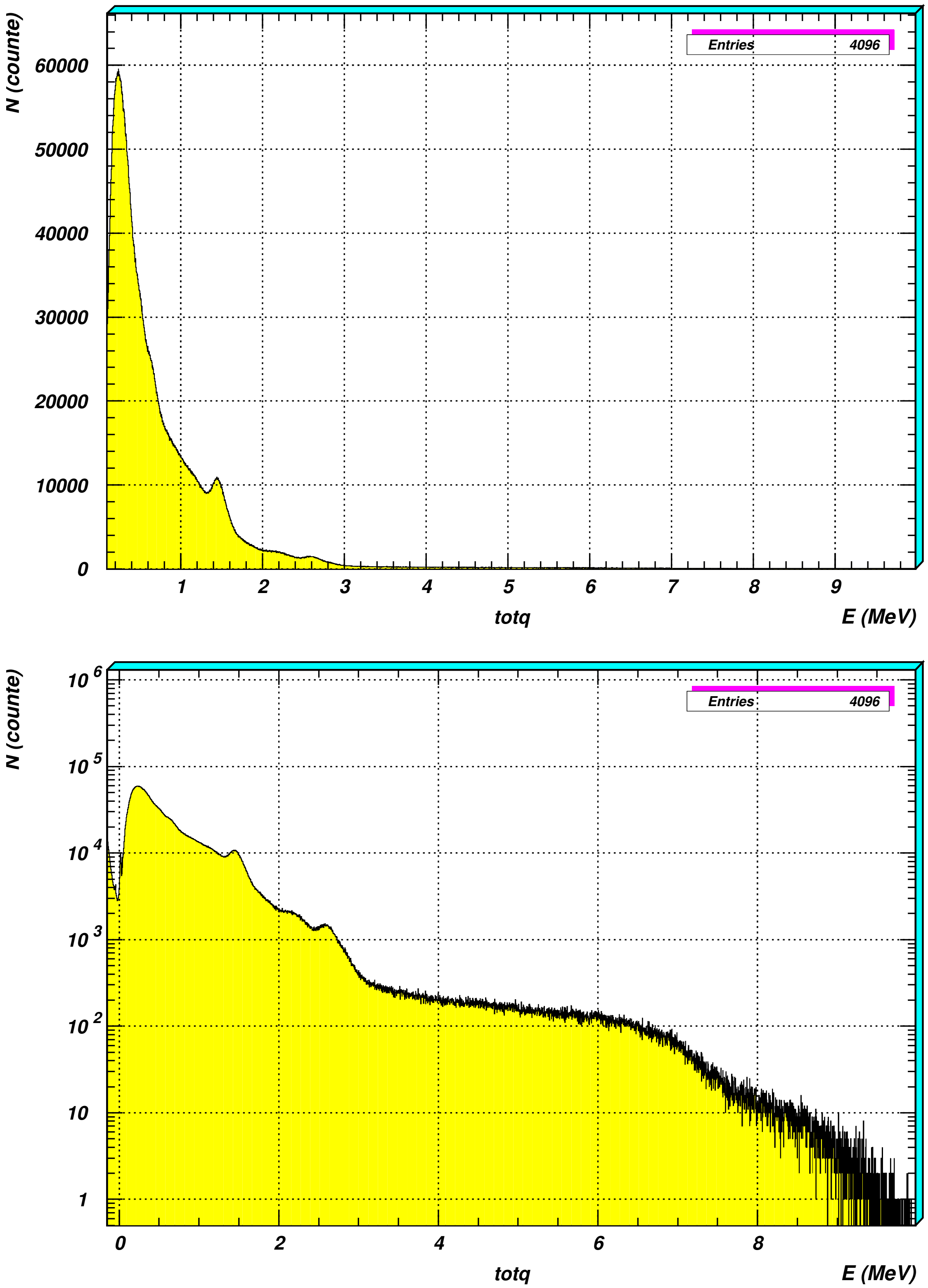

Figure 19: Measured background spectrum of a 5-kg CsI(Tl) crystal. The absence of peaks at the 3-5 MeV range gives a sensitivity of ^{238}U and ^{232}Th to a level of 10^{-12} g/g.

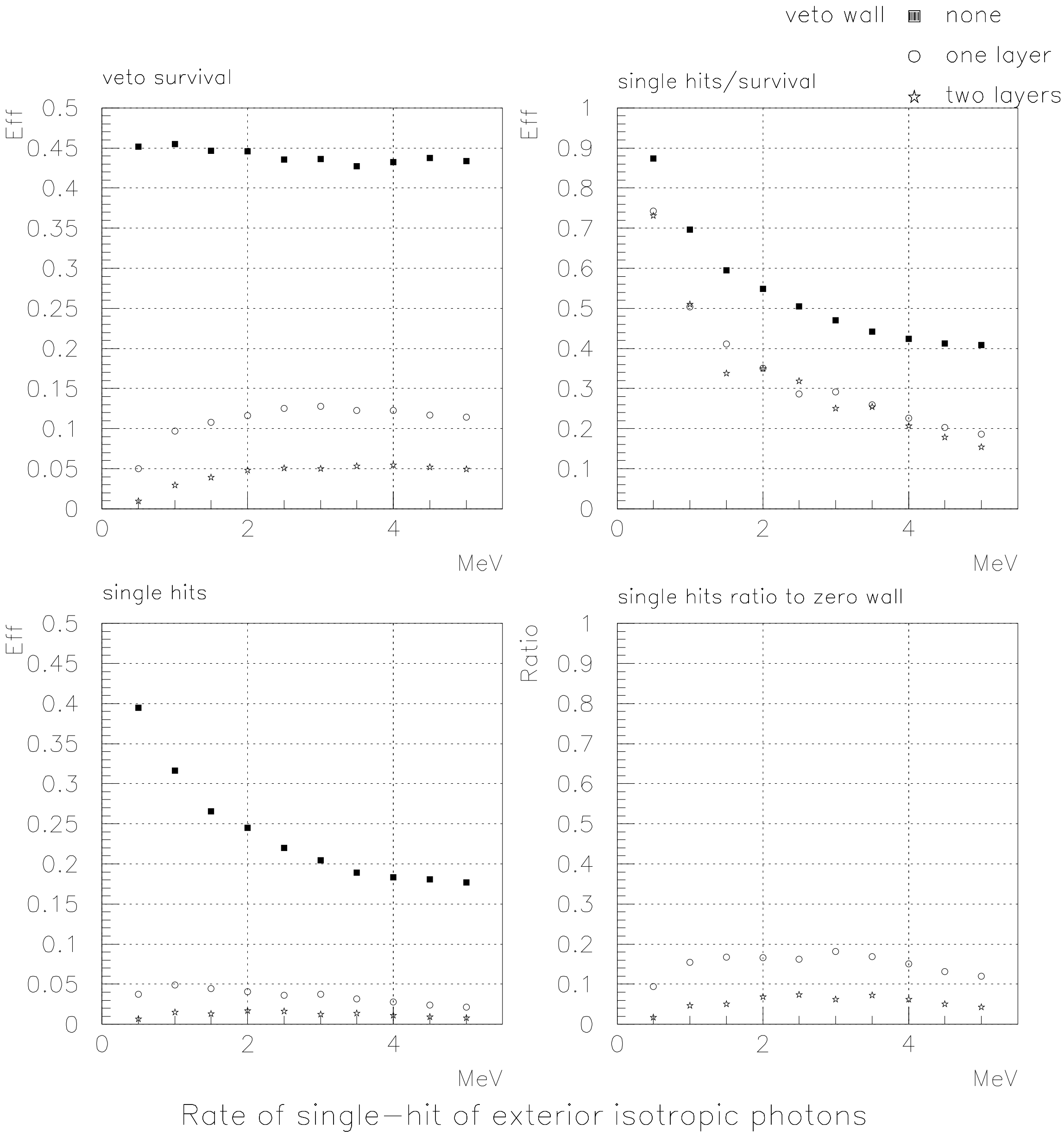

Figure 20: Veto efficiencies from external photon originated isotropically from a point source at the detector surface, with different definitions of fiducial volume (0, 1, or 2 veto layers). **Top : Left-** Survival probabilities of the photon reaching the fiducial volume without hitting the veto-layers; **Right-** Probabilities of those photons giving only single hits. **Bottom : Left-** Product of above: that is, the probabilities of an external photon creating a single hit in the fiducial volume; **Right-** Ratio of single hit probabilities with 1 or 2 layers to that without veto layer.

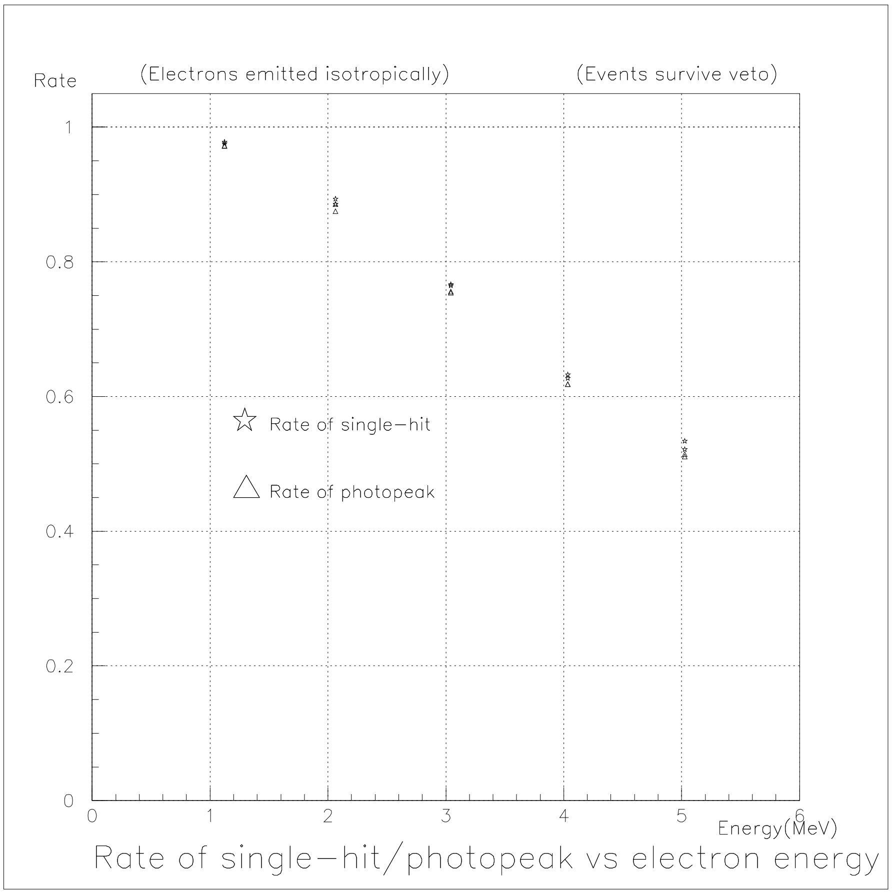

Figure 21: Single-hit efficiencies for electrons originating from the target region. The slight spread is due to different definitions of threshold cuts and target configurations.

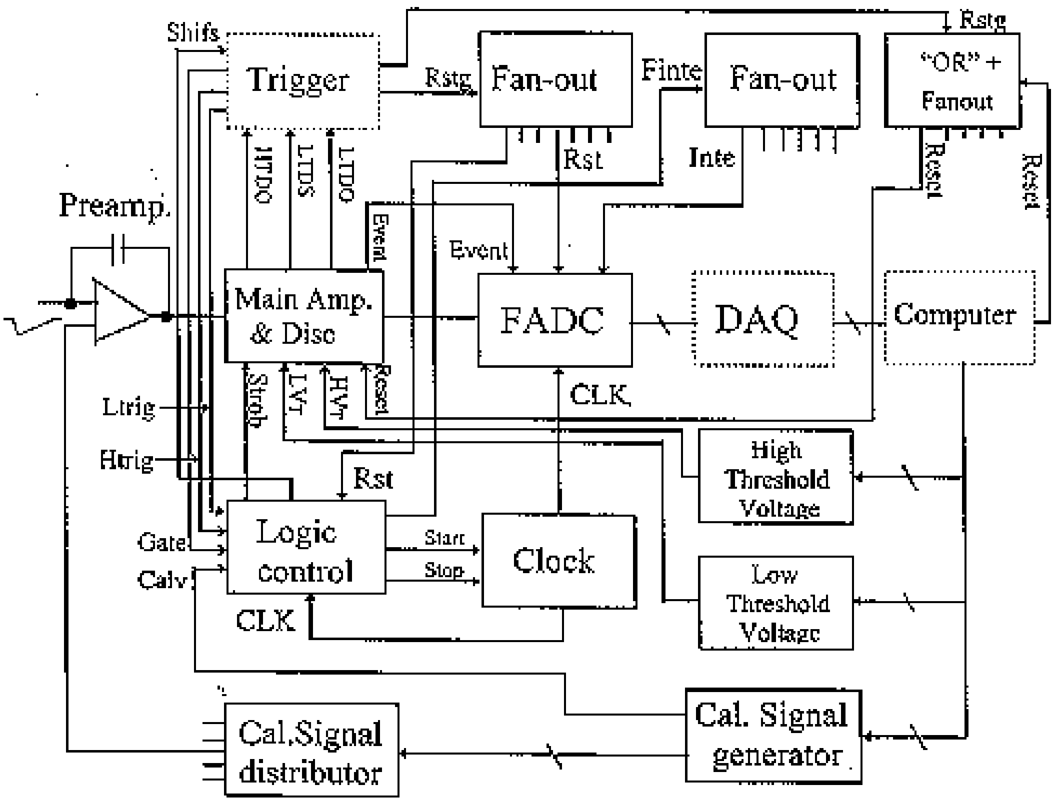

Notes:

- LTDO – Low Threshold Discrimination "Or" output
- HTDO – High Threshold Discrimination "Or" output
- LTDS – Low Threshold Discrimination Series output
- Strob – Strobe signal
- Event – Low Threshold Discrimination "Or" output enabled by strob falling edge.
- Finte – FADC INTerrupt Enable
- Stop – to stop clock
- CLK—CLocK signal
- LV_T – Low Threshold voltage
- HV_T – High Threshold voltage
- Rstg – Reset signal given by trigger when level-2 trig is negative.
- Inte – Interrupt Enable for FADC, which is the fanout of Finte.
- RST – ReSeT signal for logic control and FADC, which is the fanout of Rstg.
- Calv – Calibration Valid
- Shifs – Shift start

Figure 22: Schematic layout of the electronics system design.

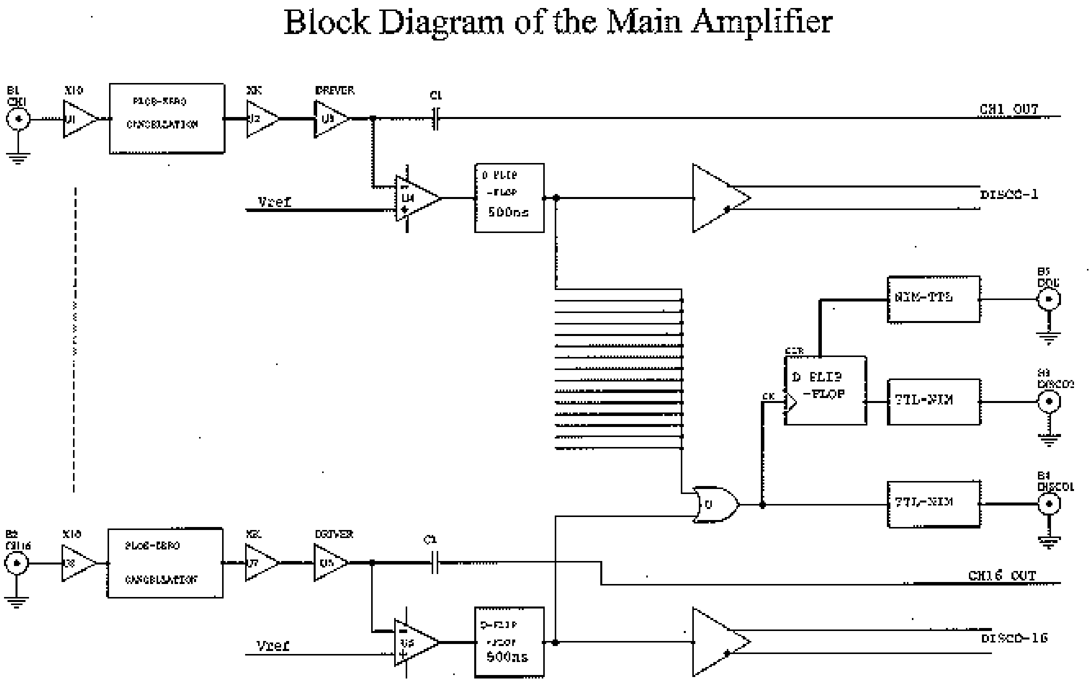

Figure 23: Block diagrams of the main amplifier plus shaper module.

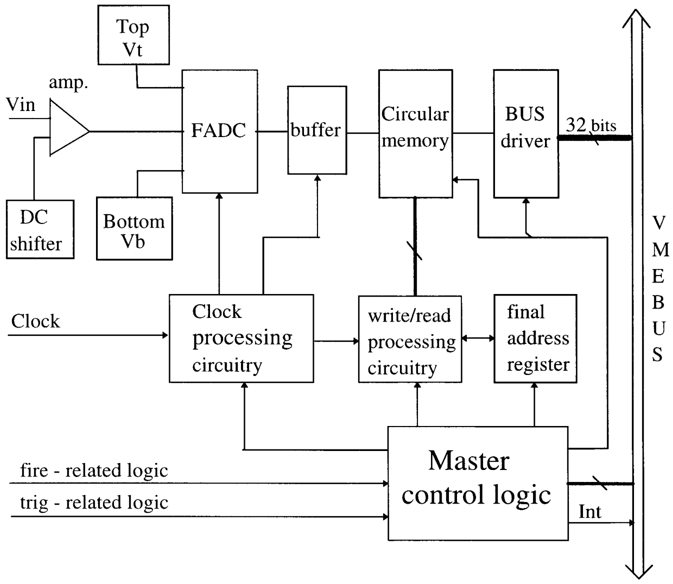

FADC module block diagram

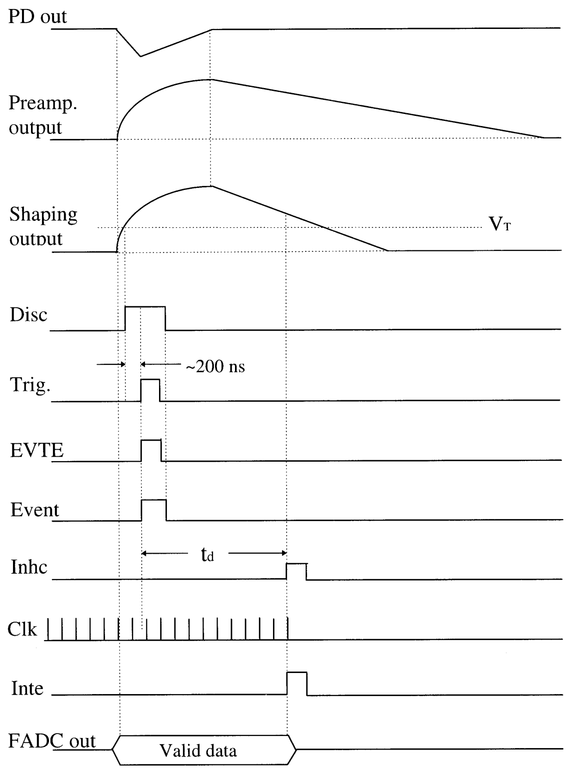

TEXONO electronics timing diagram

Figure 24: **Top:** Block diagram of the FADC module, and **Bottom:** its timing characteristics.

Block Diagram of the Threshold Voltage Generator

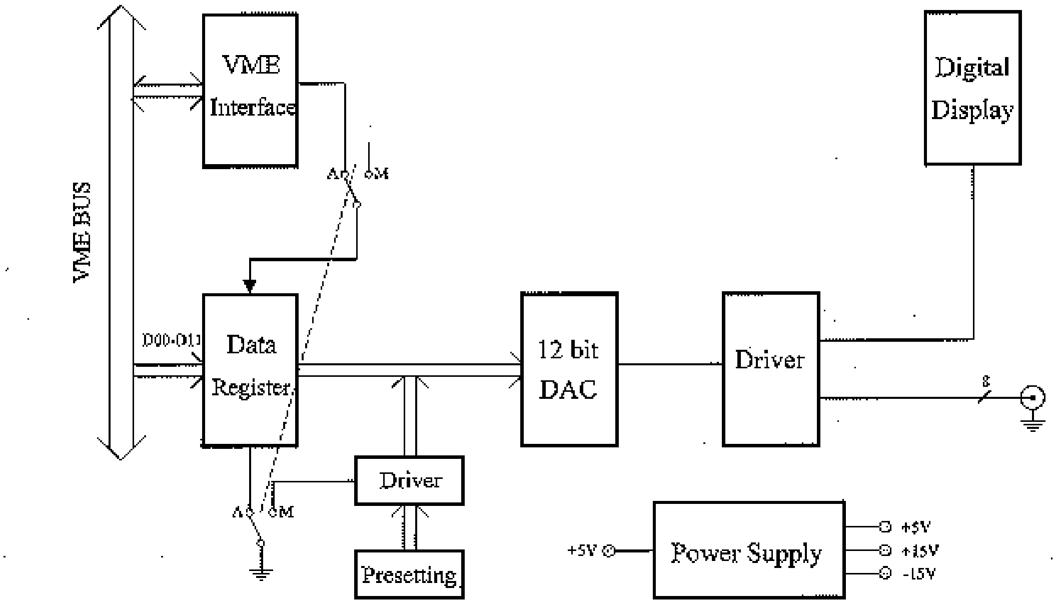

Block Diagram of the Calibration Circuit

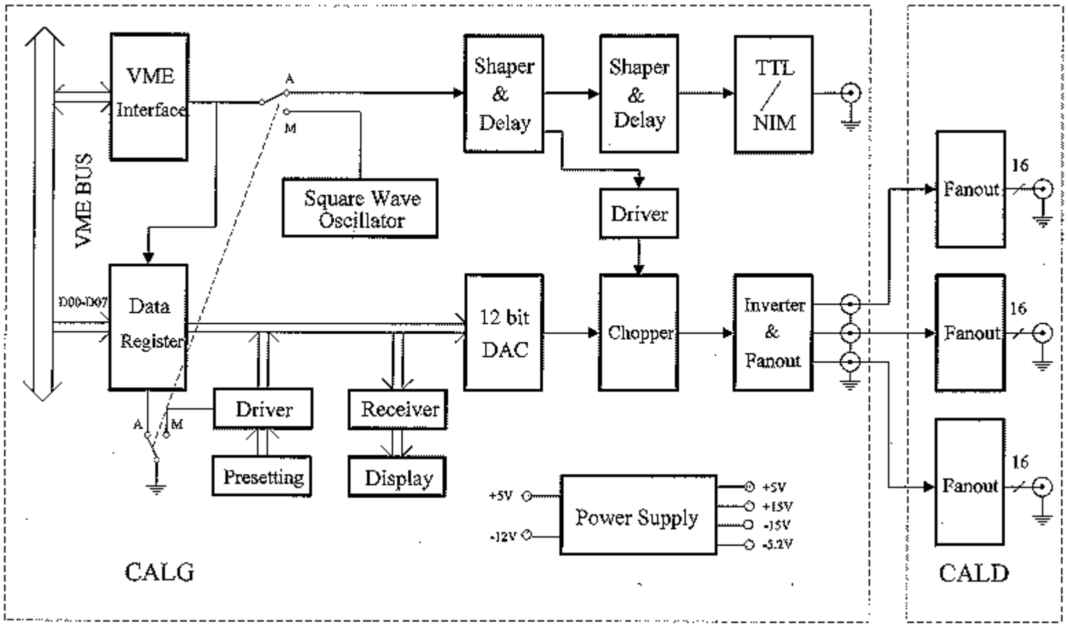

Figure 25: Block diagrams of the Threshold Adjustor module and of the Pulser Calibration module.

Block Diagram of the Logic Control Circuit

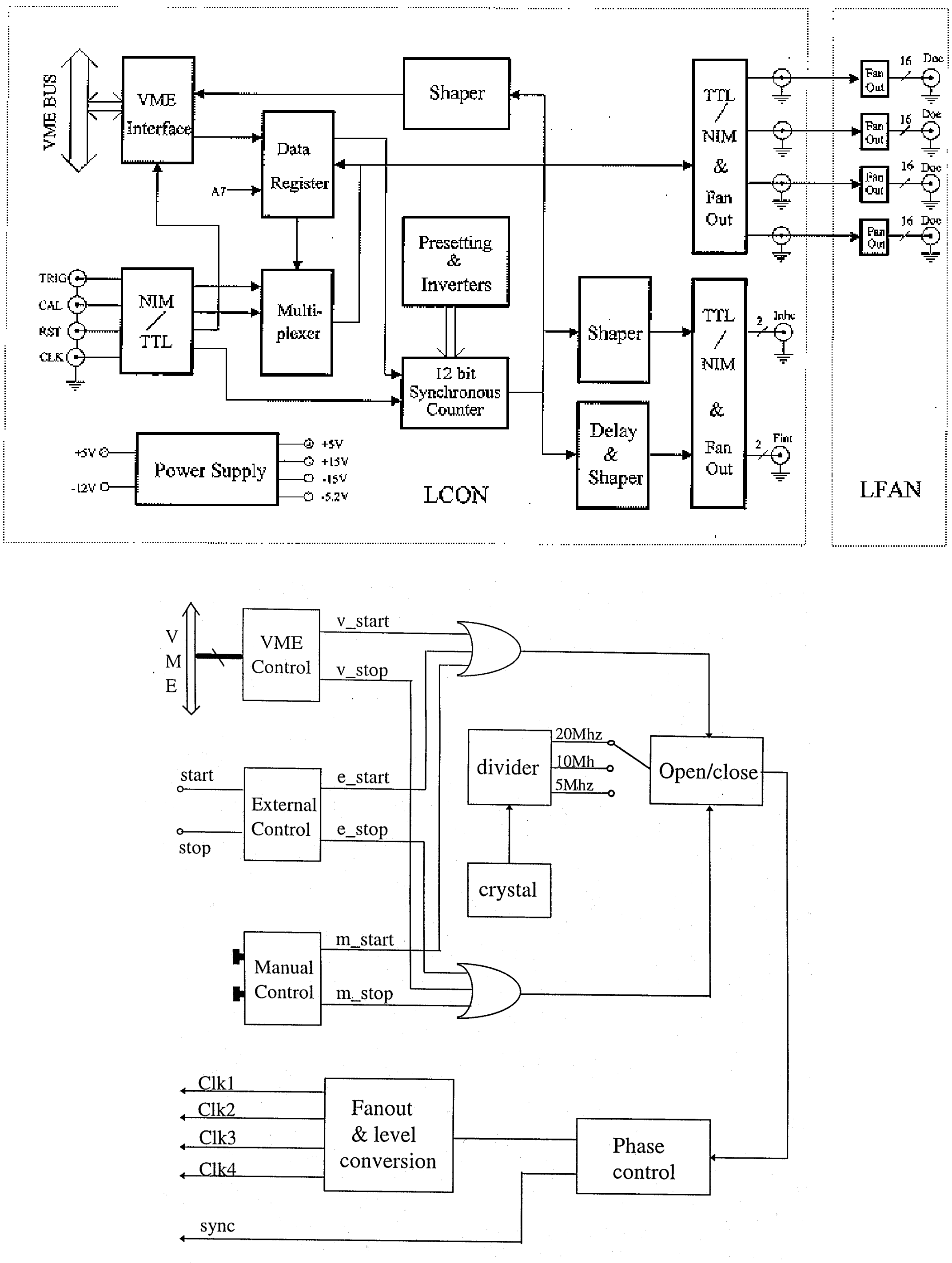

Clock module block diagram

Figure 26: Schematic layout of the logic control and the clocking circuits.

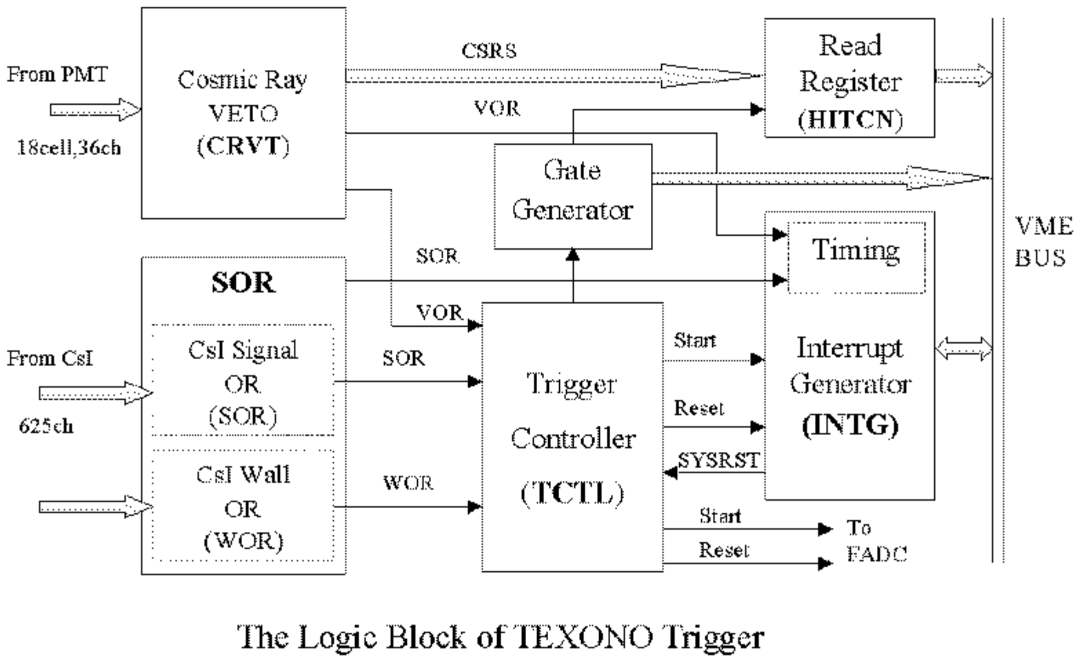

Figure 27: Schematic layout of the trigger system design.

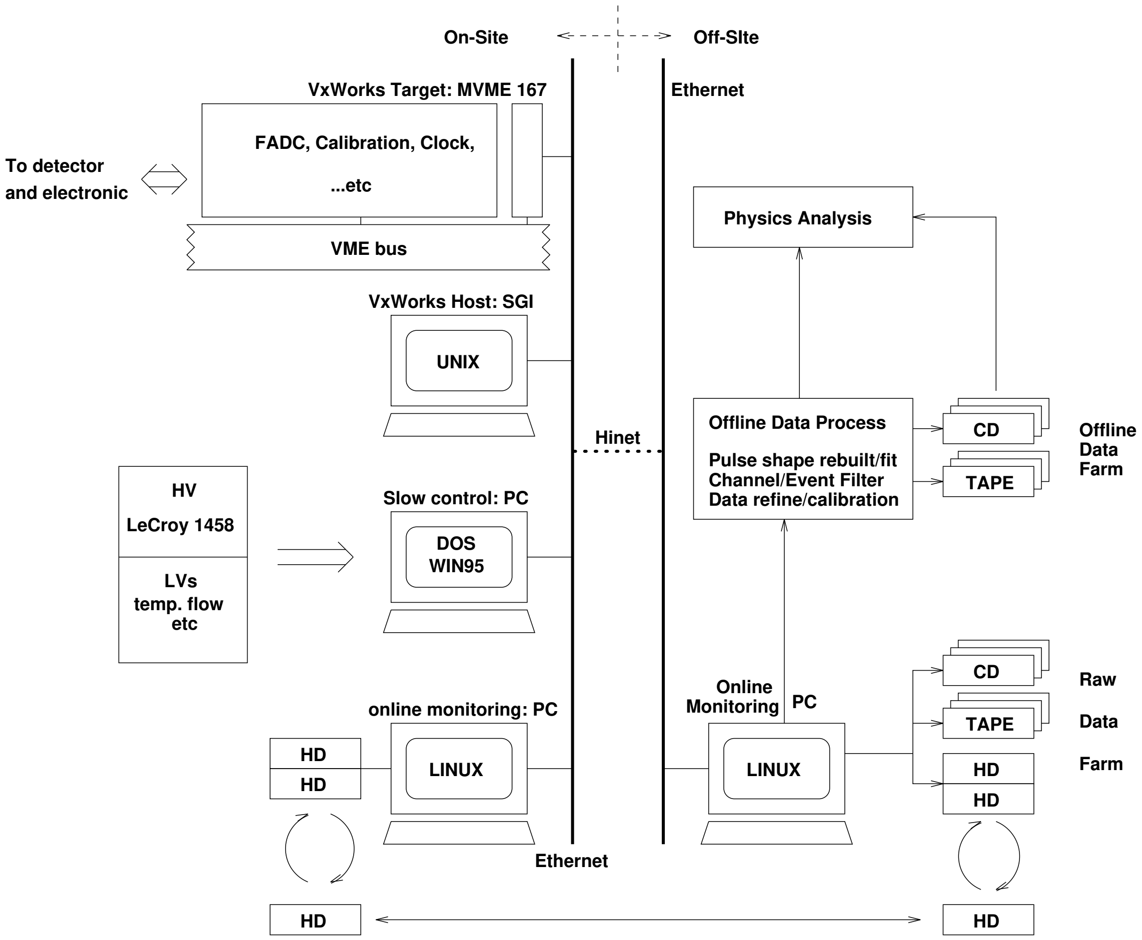

Figure 28: Schematic layout of the data acquisition and on-line monitoring systems, and its interfacing with the off-line software.

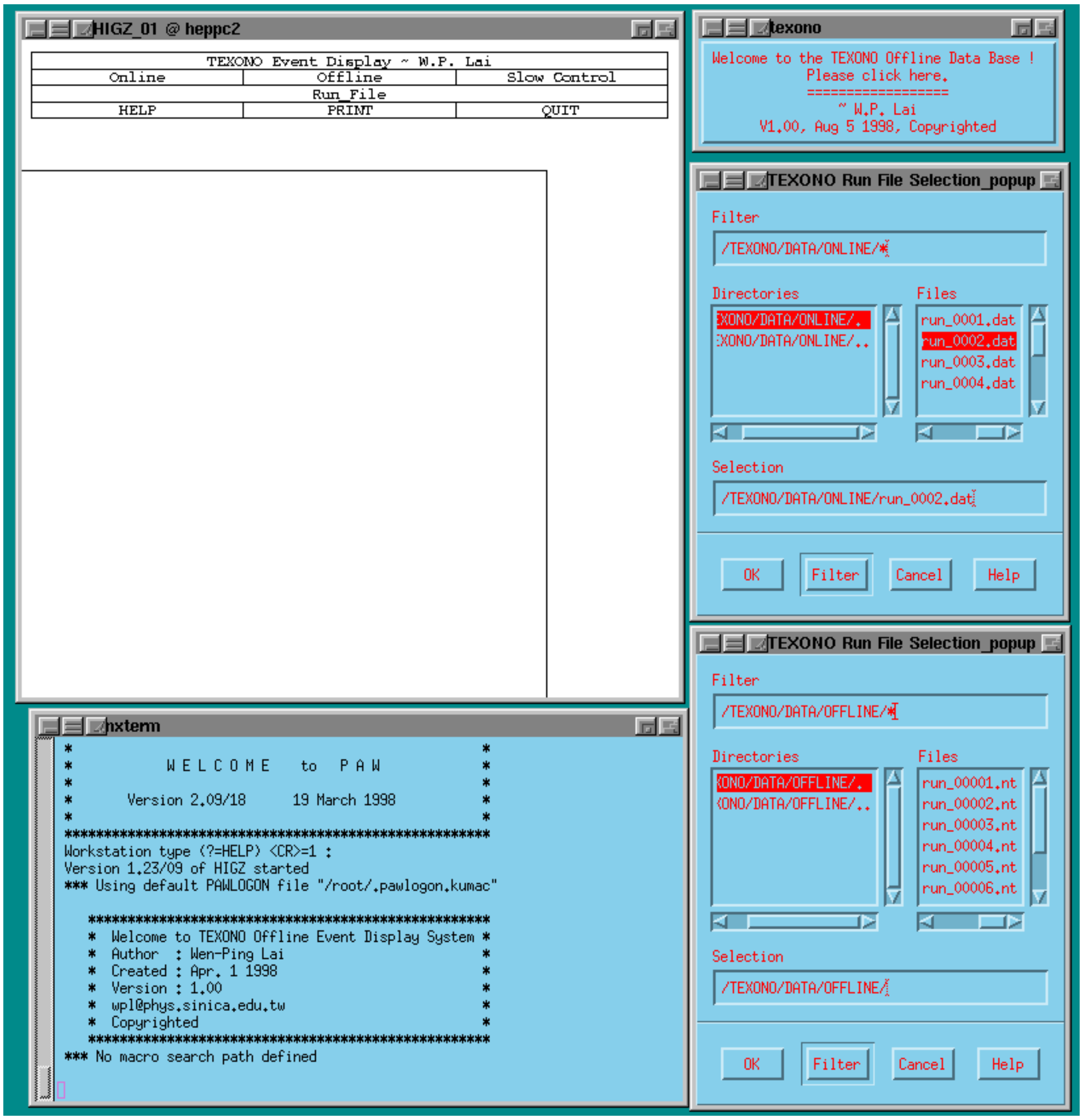

Figure 29: Front panel of the display system, from which various functions and different data set can be selected by mouse-buttons.

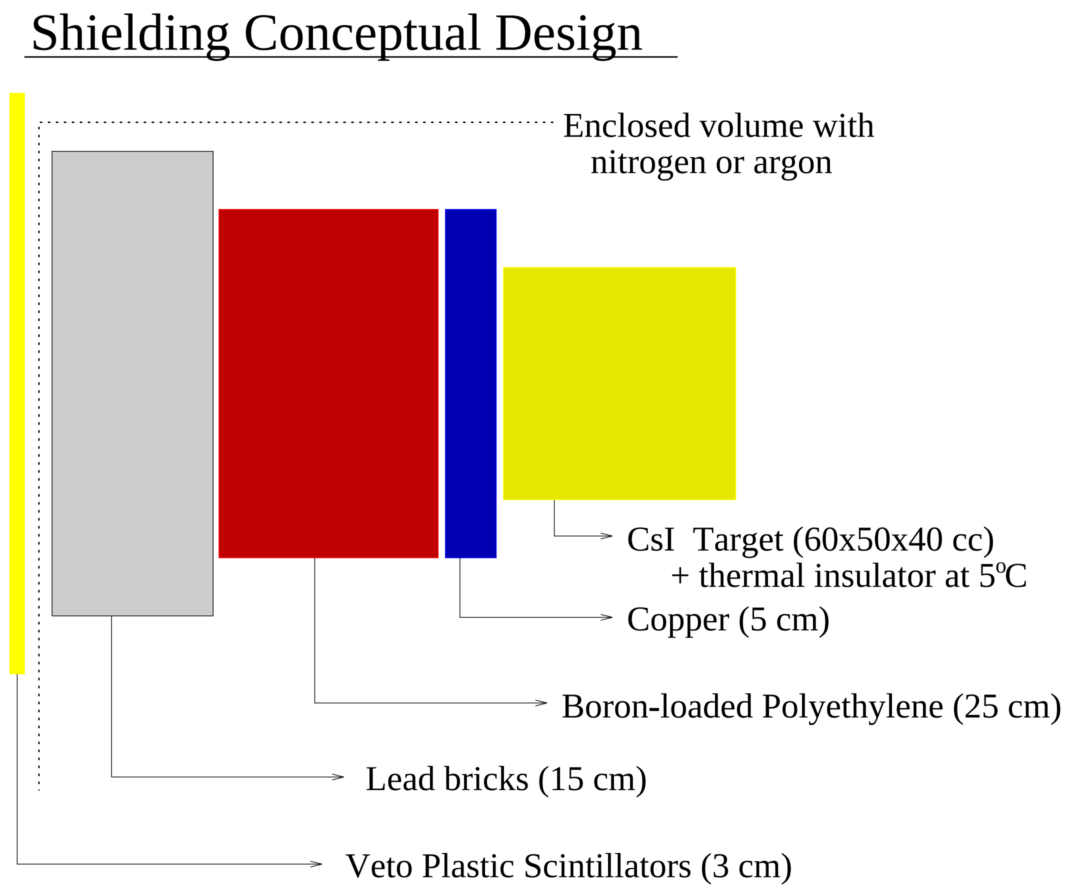

Figure 30: Schematic layout of the shielding. The coverage is 4π but only one face is shown.

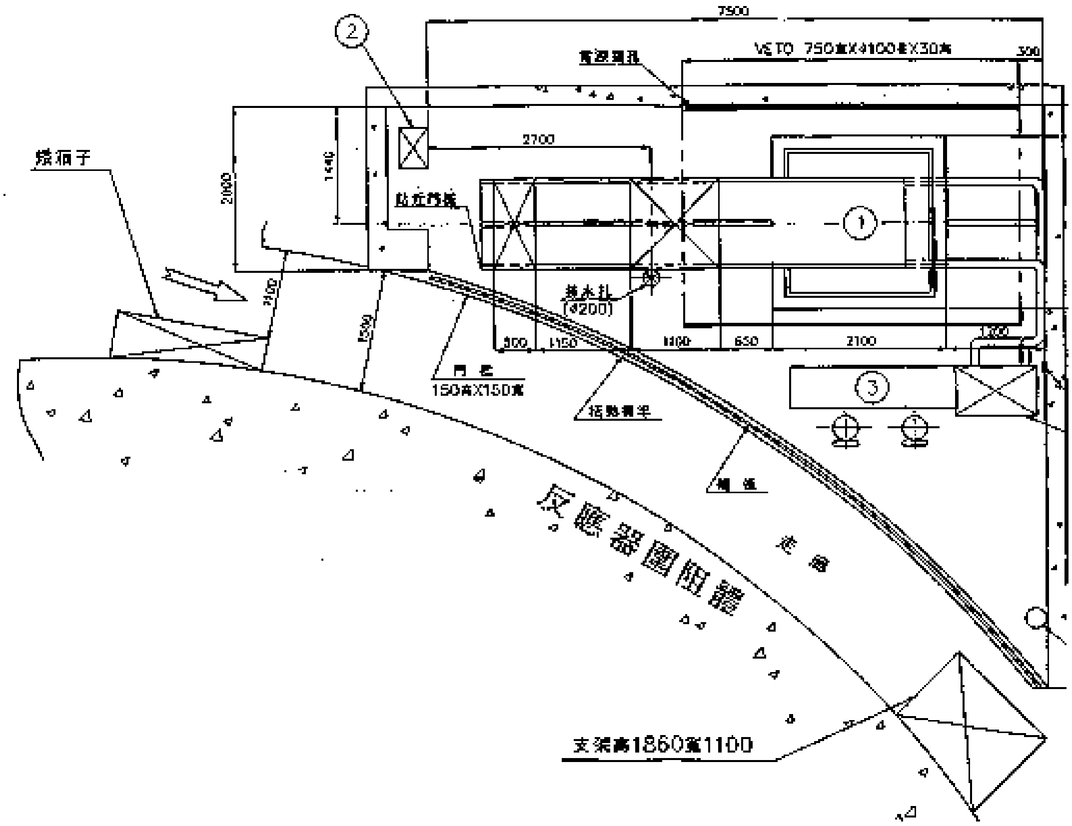

Figure 31: Technical drawing showing the layout of the shielding at the experimental cite: (1) is the target location while (3) is where the electronic racks and control panels will be placed.

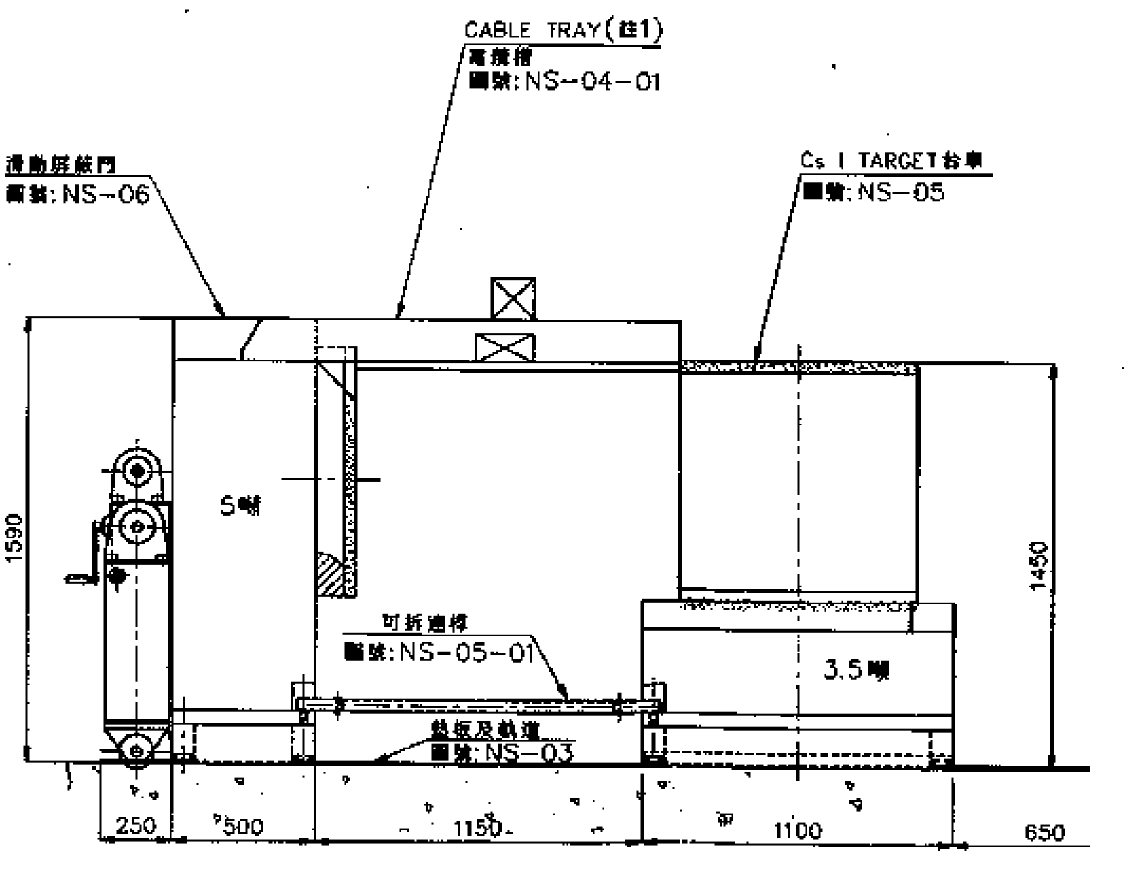

Figure 32: Techical drawing of the movable shielding wall and the target trolley.

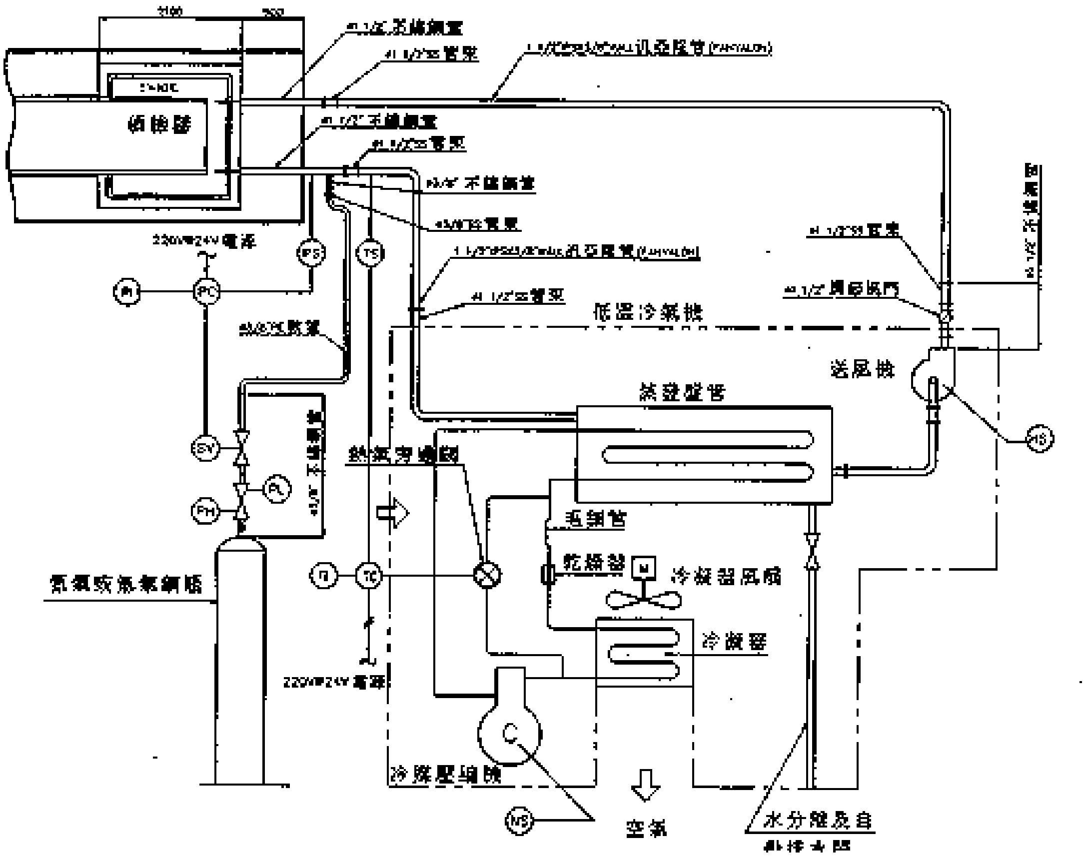

Figure 33: Schematic diagram of the cooling system.

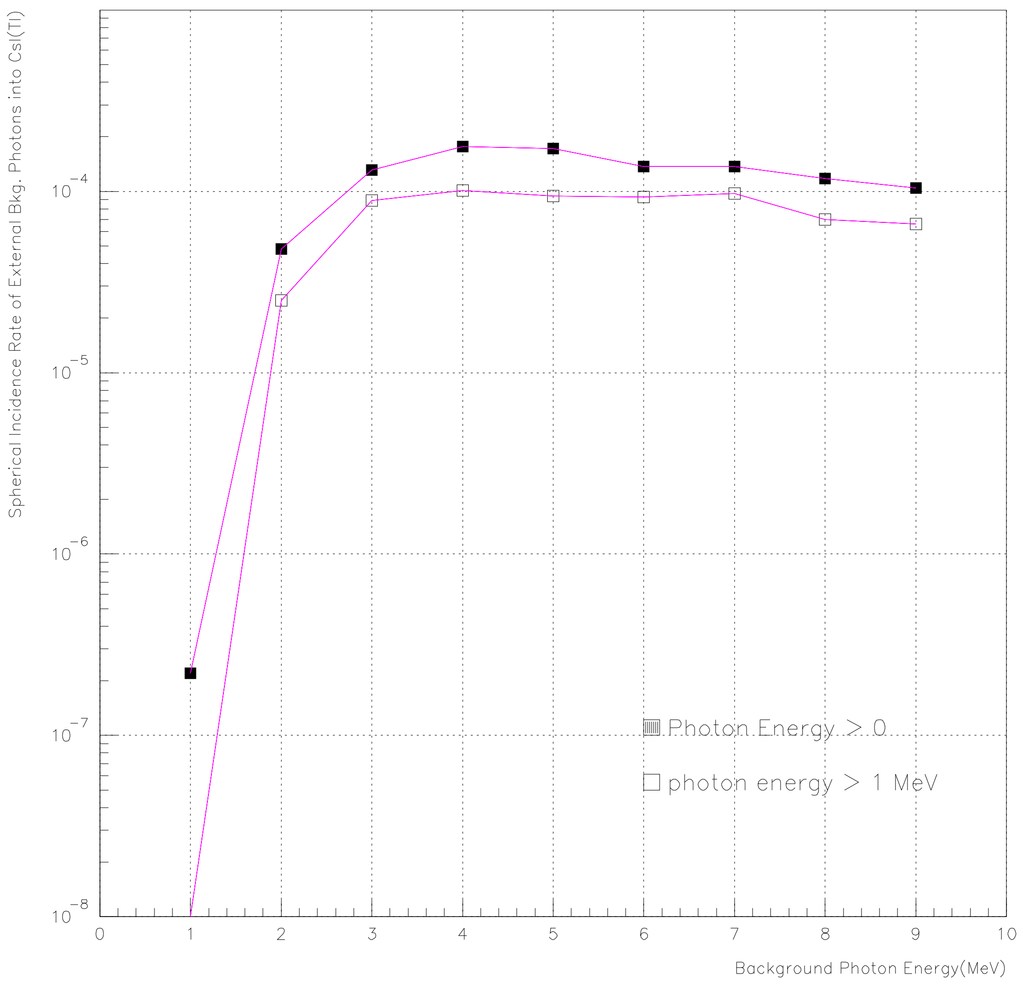

Figure 34: Attenuation factors for photons due to our shielding configuration. The photons are originated from a spherical shell external to the shieldings and traverse radially inwards to the target

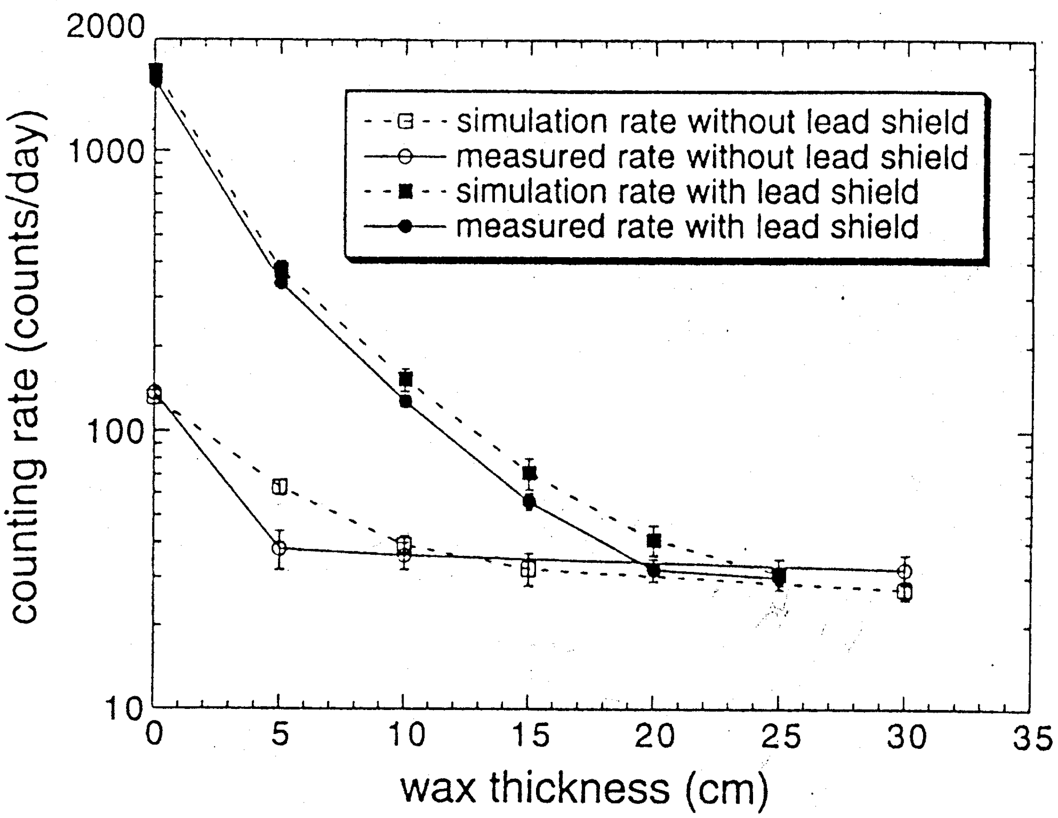

Figure 35: The variation of the neutron flux, as measured by a BF_3 detector, with the thickness of wax in the shielding. The thickness of the lead shield is 10 cm and the site overburden is 17 mwe.

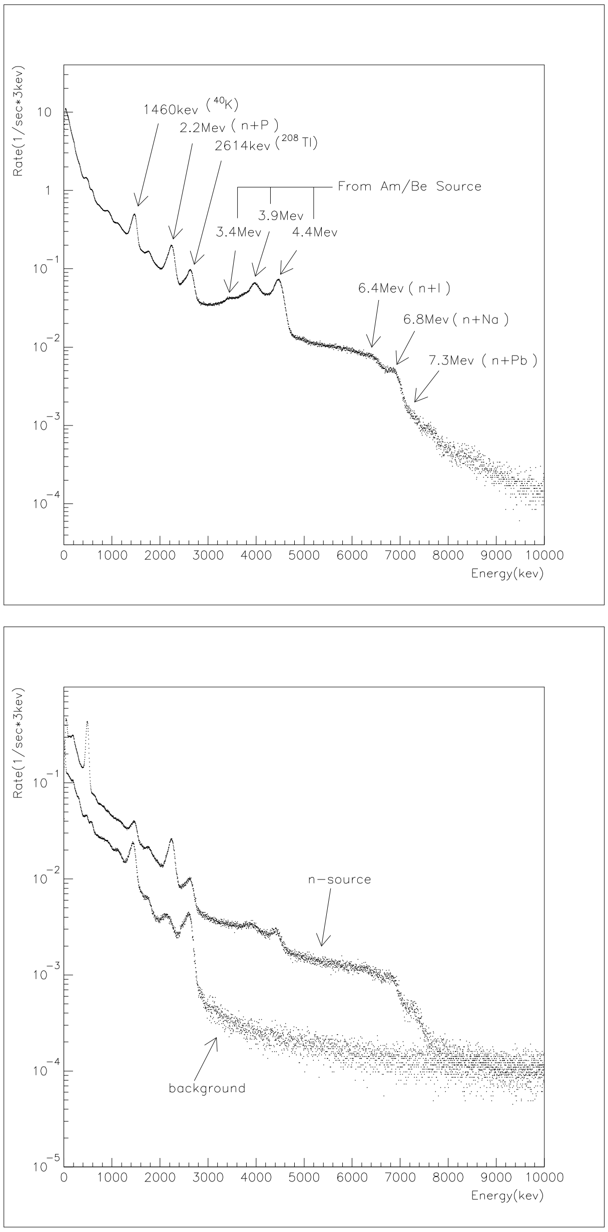

Figure 36: Measured spectra with the prototype shielding set up at AS basement: **Top:** With a Am/Be neutron source, with many structures observed, and **Bottom:** Comparison with a background spectrum which does not have any of the structures due to neutrons.

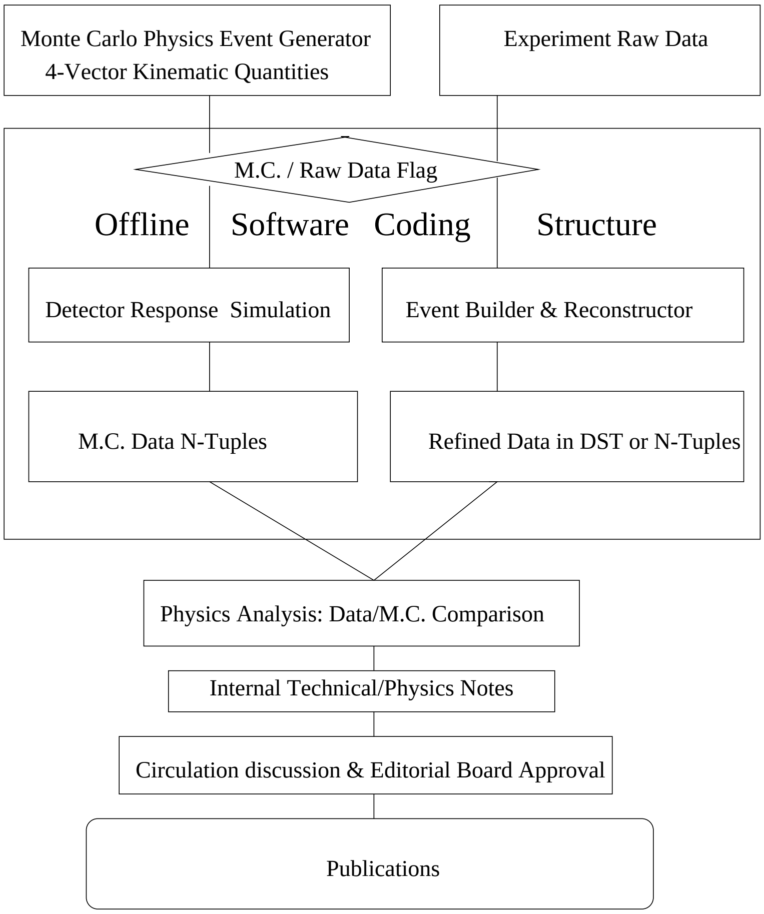

Figure 37: The schematic chart showing offline data flow and software organization.

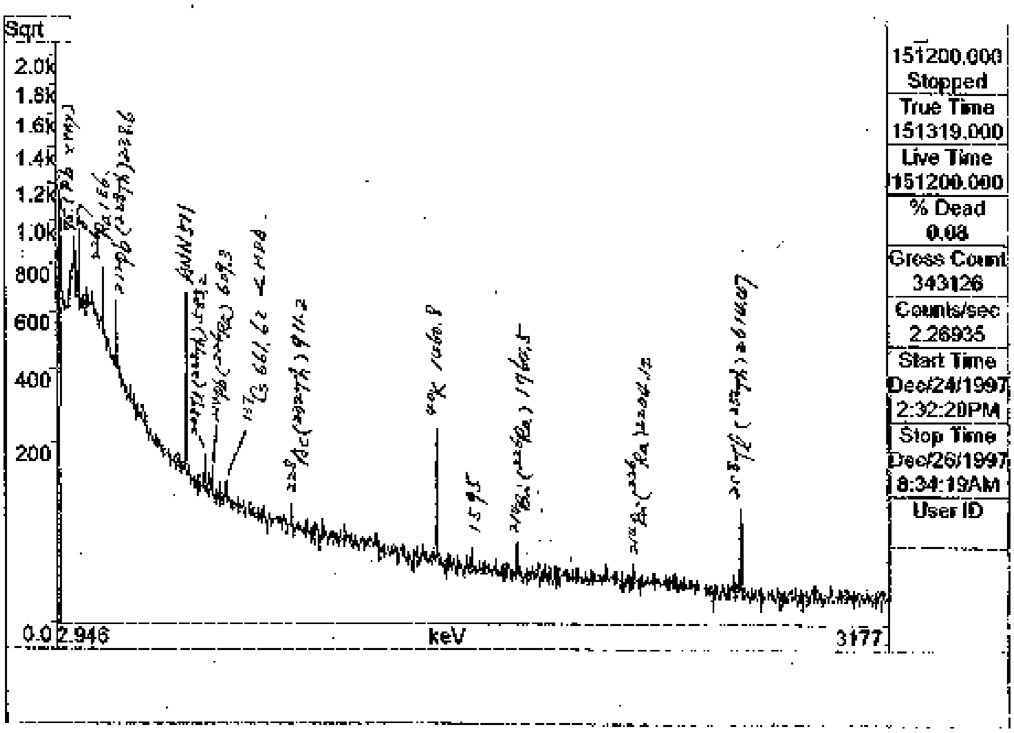

Figure 38: A typical spectra taken by the high-purity germanium detector for radiopurity measurements, showing the ambient background from ^{40}K, as well as the ^{238}U and ^{232}Th series. There is a slight excess for the 660 keV ^{137}Cs in this particular case.

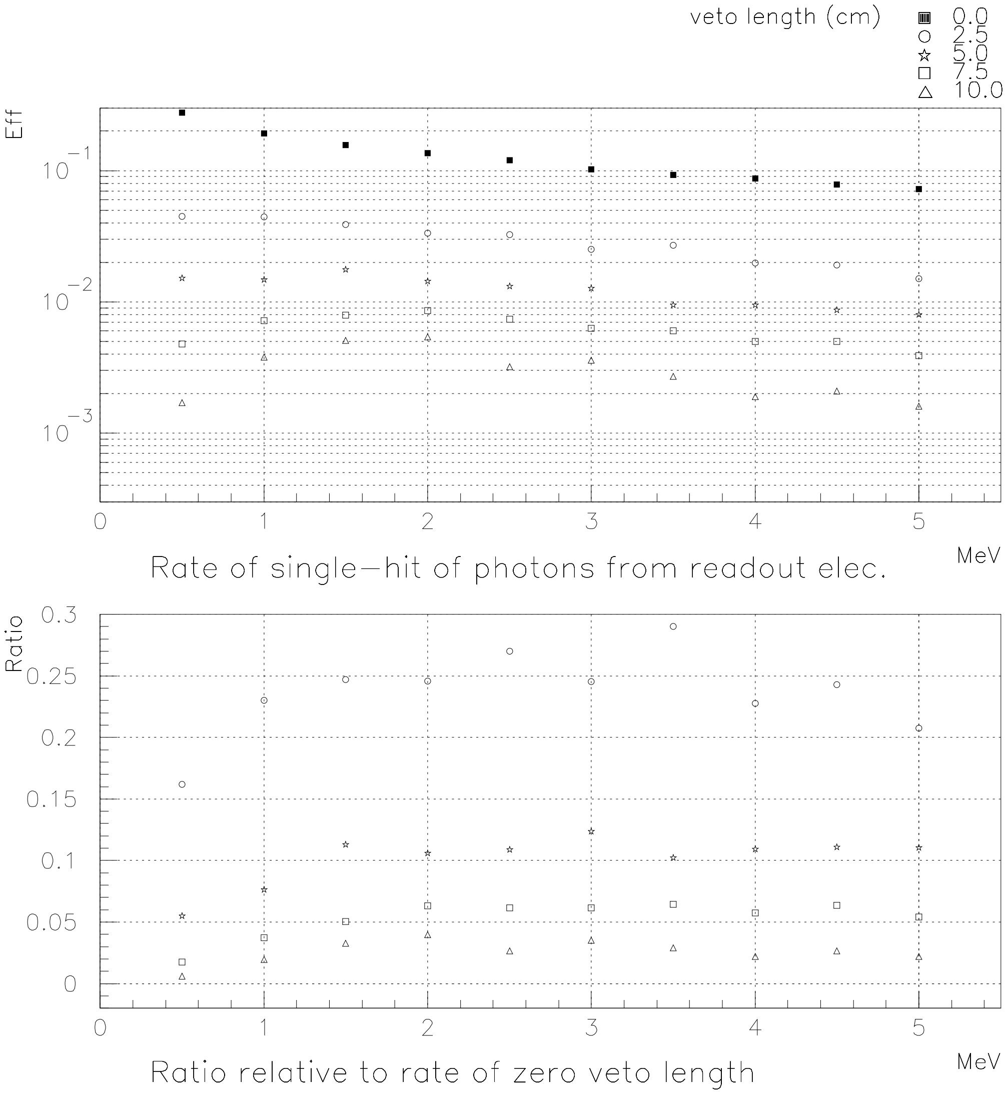

Figure 39: Attenuation factors for background photons originating isotropically from the photo-diodes and pre-amplifiers regions. **Top:** Probability of producing a single-hit with different lengths for the active veto, and **Bottom:** Ratio of the attenuation factor at length L>0 to that at L=0.

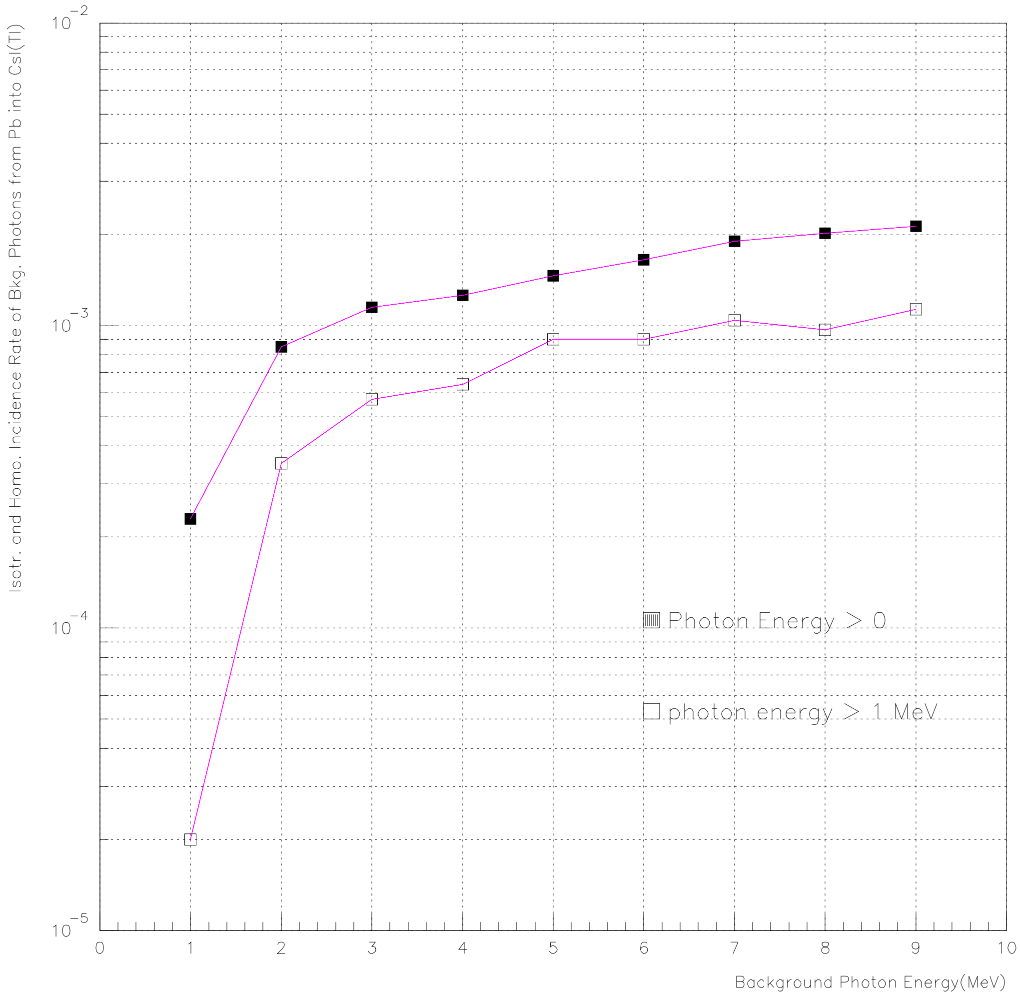

Figure 40: Attenuation factors for photons produced uniformly and isotropically in the lead shieldings to hit the inner target region.

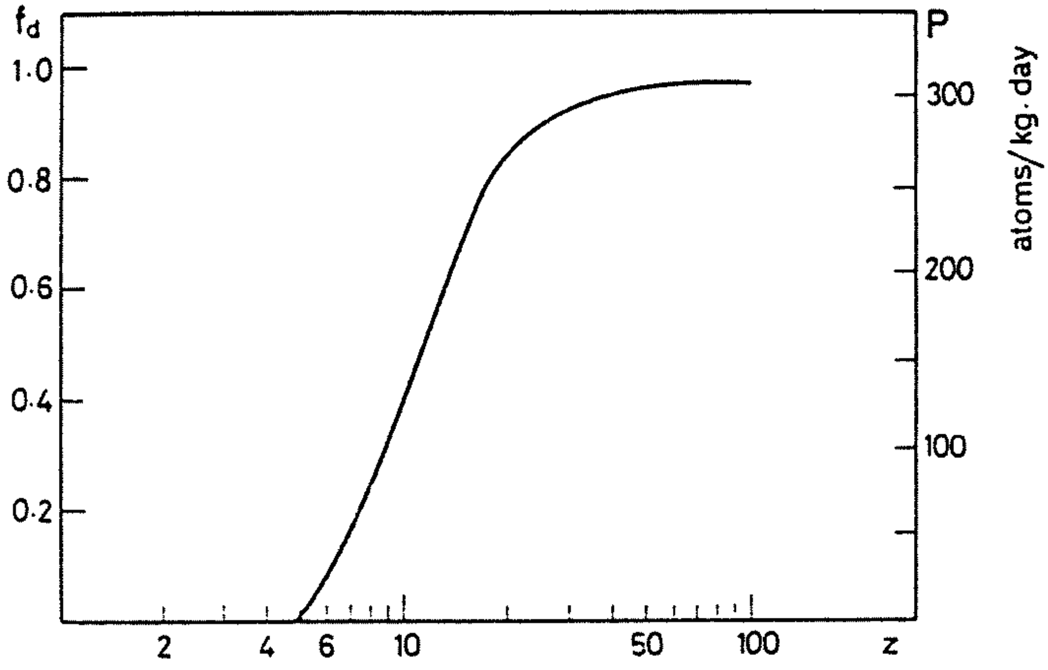

Figure 41: The muon capture probability and rate as a function of atomic number Z : f_d denotes the fraction of muons being captured after stopping at the nuclei (those not captured will decay) and P is the calculated rate at sea-level.

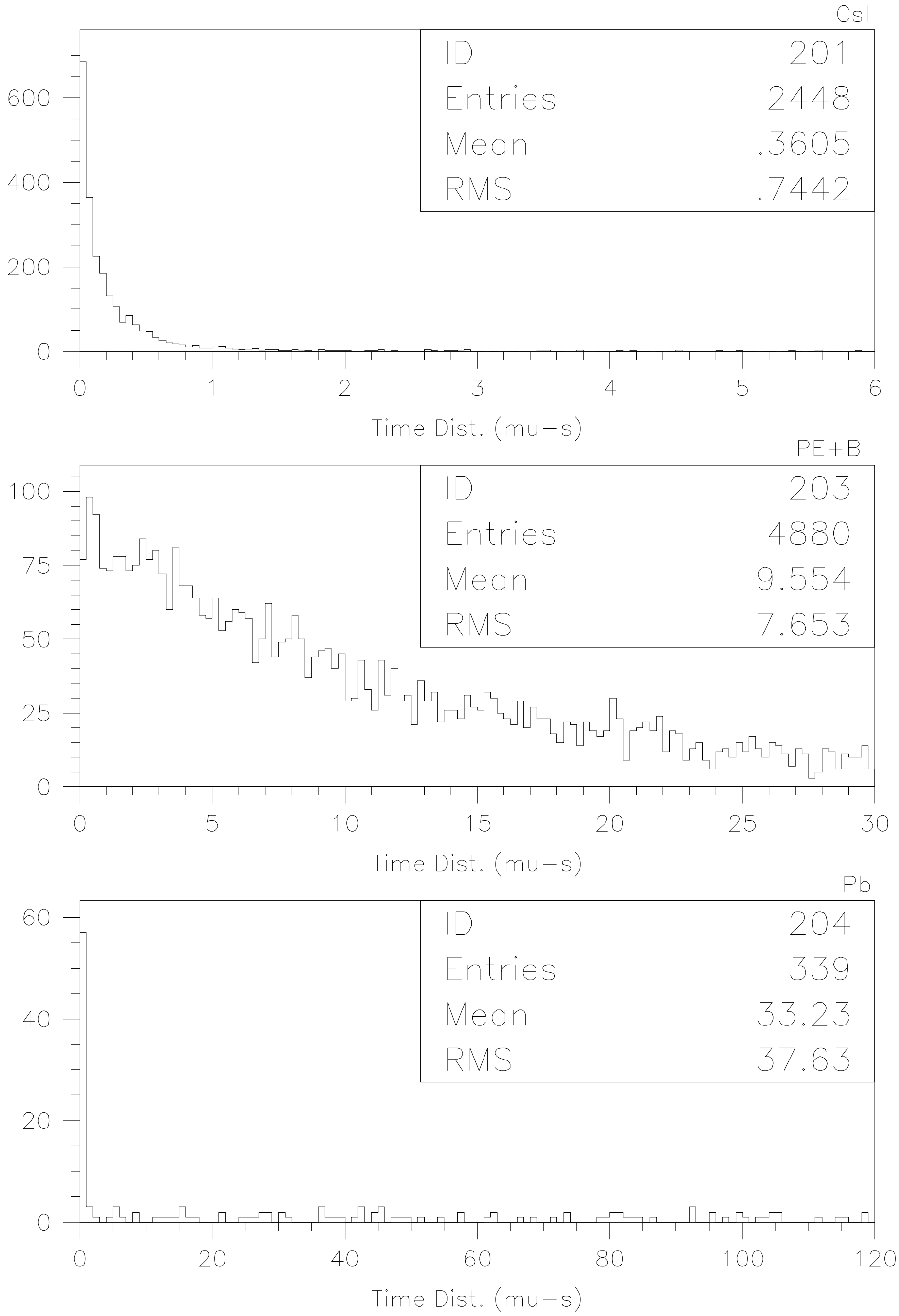

Figure 42: Capture time distribution 1 MeV neutrons. **Top:** Neutrons produced uniformly and isotropically in CsI target and the captured also by CsI target; **Middle:** Neutrons produced isotropically in the center of the lead plates and then captured by the boron-loaded polyethylene and **Bottom:** by the lead itself.

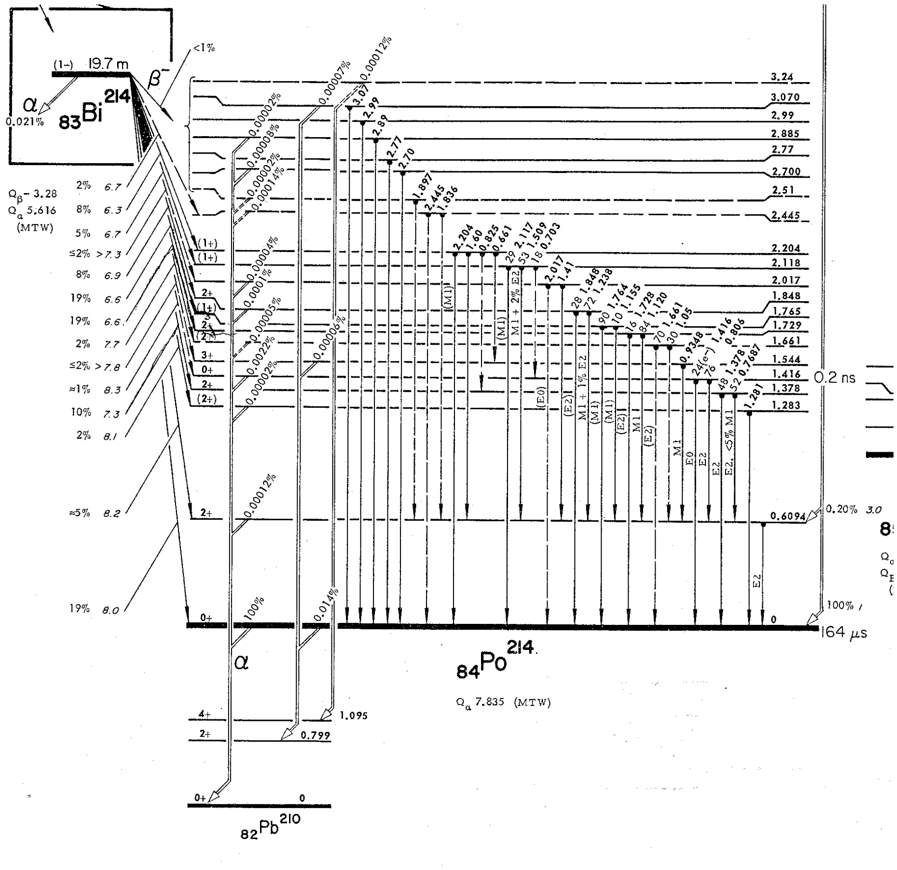

Figure 43: Decay schemes for the ^{214}Bi $-^{214}$ Po cascade in the ^{238}U series.

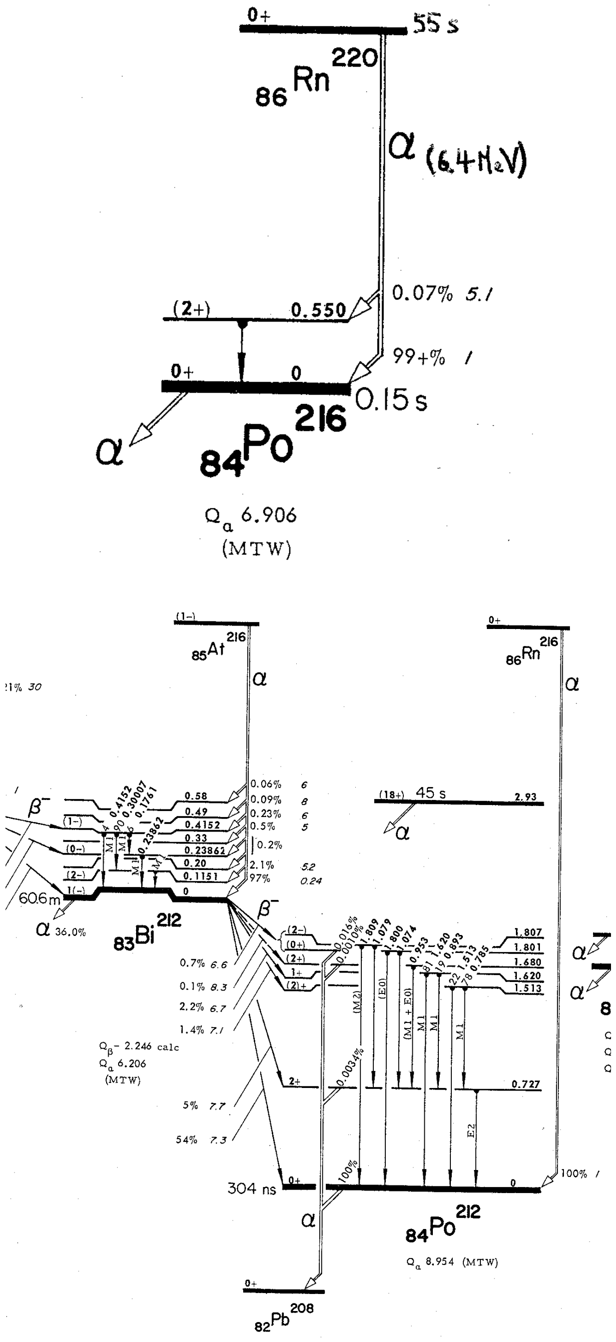

Figure 44: Decay schemes of the ^{220}Rn $-^{216}$ Po and ^{212}Bi $-^{212}$ Po cascades of the ^{232}Th series.

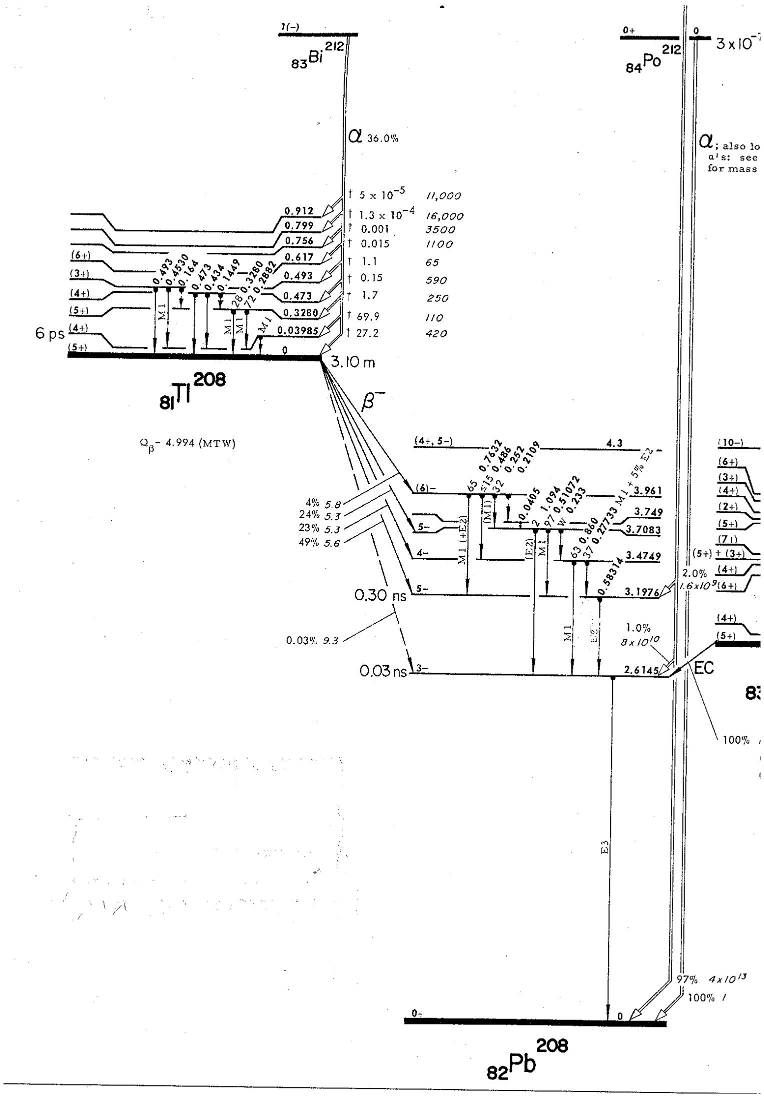

Figure 45: Decay scheme of ^{208}Tl to ^{208}Pb with the emission of the 2.614 MeV γ-ray.

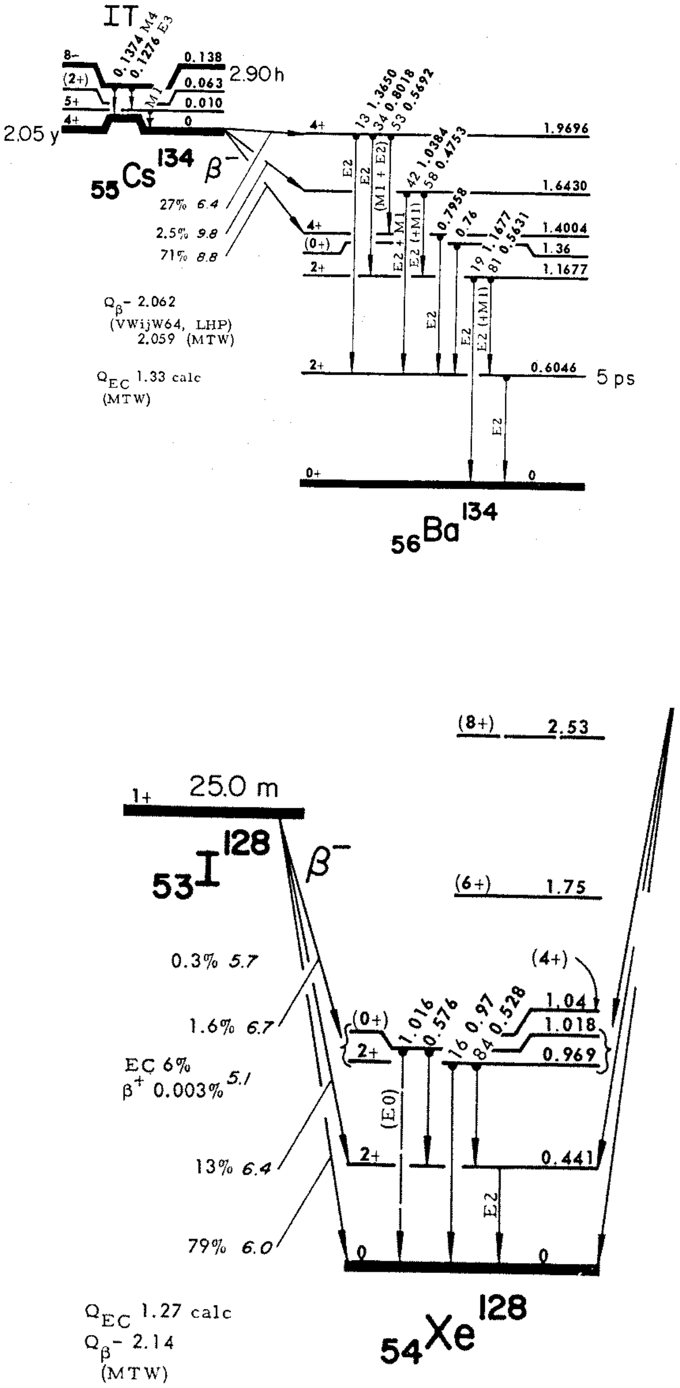

Figure 46: Decay schemes of the isotopes ^{134}Cs and ^{128}I.

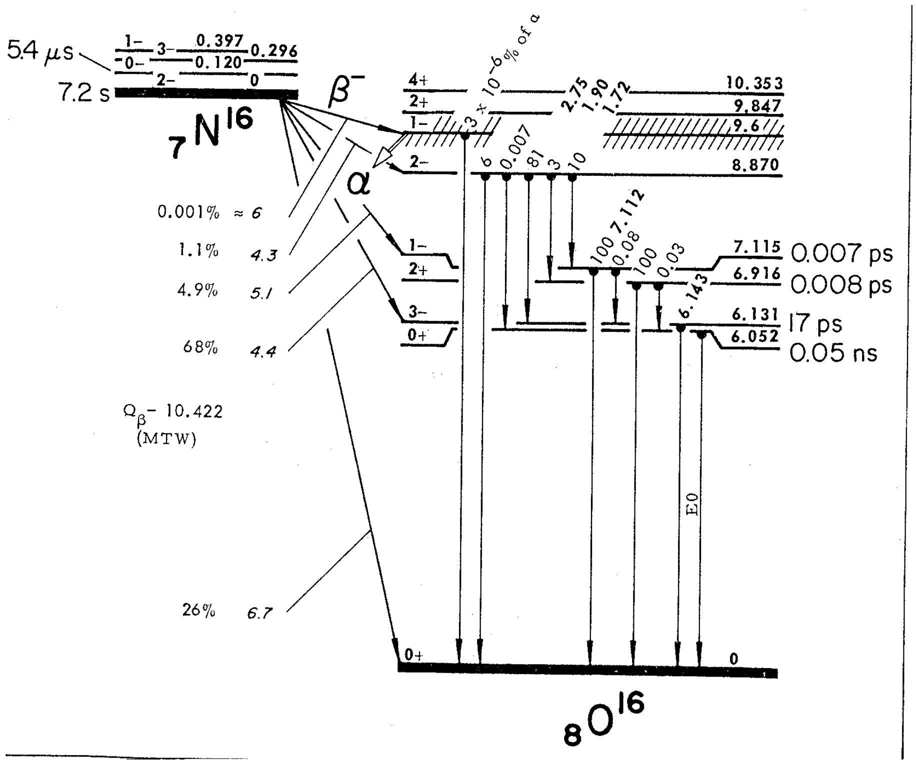

Figure 47: Nuclear level diagrams of the ^{16}O-^{16}N system, indicating potential high energy background due to muon capture by ^{16}O.

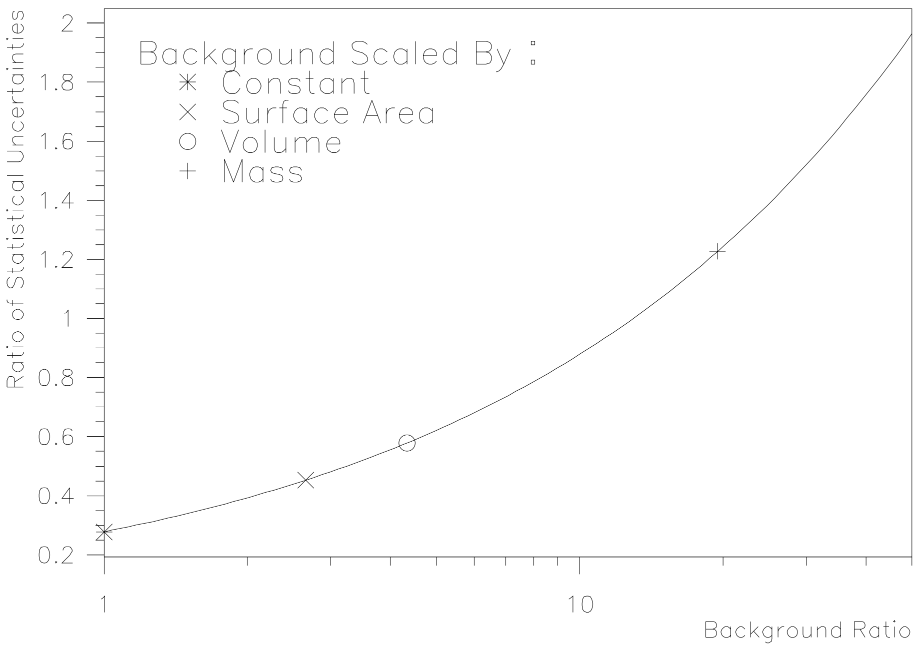

Figure 48: Projected statistical uncertainties in the measured number of $\bar{\nu}_e$e events in the CsI detector relative the Savannah River experiment, where the signal ratio R_S is 3.6, under different cases where the background would be constant or scaled by the surface area, volume or mass ratios between the two experiments. A fiducial mass of 312 kg is assumed.

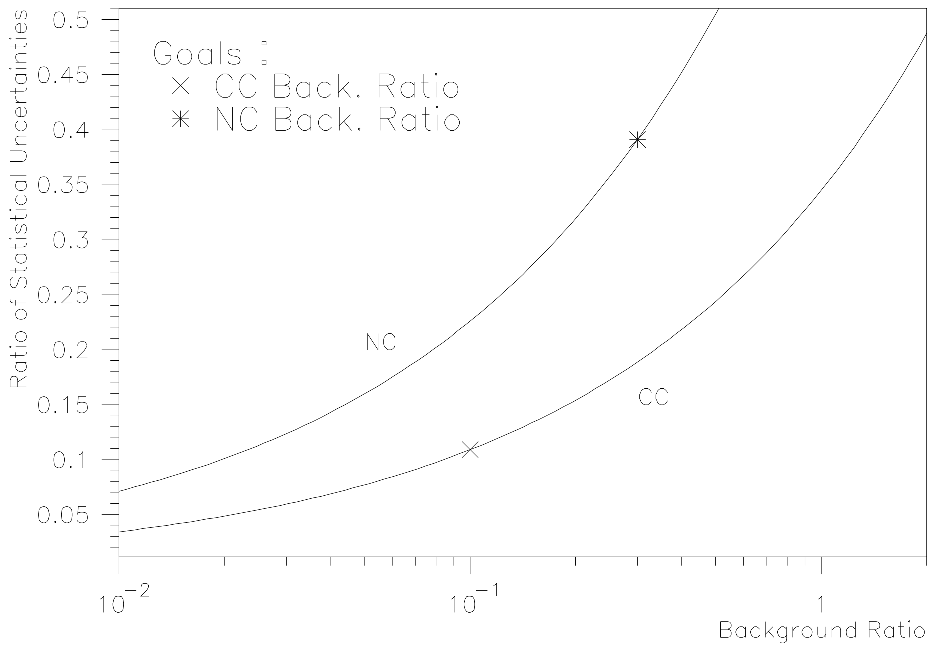

Figure 49: Projected statistical uncertainties in the measured number of $\bar{\nu}_e$d events in the CsI detector relative the Savannah River experiment, where the signal ratios R_S are 2.9 and 1.4 for the CC and NC interactions, respectively. The goals are to reduce the background of CC and NC to relative ratios of 0.1 and 0.3, respectively.